

Modeling of Geophysical Flows – Analysis of Models and Modeling Assumptions Using UQ

Abani K. Patra^{1,3}, Andrea Bevilacqua², Ali Akhavan-Safaei¹, E. Bruce Pitman⁴, Marcus I. Bursik², and David Hyman²

¹*Dept. of Mech. and Aero. Eng., University at Buffalo, Buffalo NY 14260*

²*Dept. of Geology, University at Buffalo, Buffalo NY 14260*

³*Comp. Data Science and Eng., University at Buffalo, Buffalo NY 14260*

⁴*Dept. of Materials Design and Innovation, University at Buffalo, NY, 14260*

{abani, abevilac, aliakhav, pitman, mib, davidhym}@buffalo.edu

Contents

1 Geophysical mass flows	3
2 Overview of the models	4
2.1 Modeling Assumptions	4
2.2 Governing Equations, Boundary Conditions and Numerical Solver	5
2.3 Rheology assumptions	6
2.3.1 Mohr-Coulomb model	6
2.3.2 Pouliquen-Forterre model	8
2.3.3 Voellmy-Salm model	9
2.4 Overview of the case studies	10
3 UQ Process	11
3.1 Statistical analysis of force contributions	13
3.2 Forces terms definition	15
3.3 Definition and consistency of the input variables	16
4 QoIs and Data Collected - Flow down and inclined plane, and a change in slope to a flat plane	19
4.1 Observable outputs	19
4.1.1 Flow Height, local measurements	20
4.1.2 Flow Speed, local measurements	21
4.1.3 Froude Number, local measurements	21
4.1.4 Flow Acceleration, local measurements	22
4.1.5 Flow extents and averaged measurements	24
4.2 Statistical analysis of dynamic quantities	24
4.2.1 Forces, spatial integral	24
4.2.2 Powers, spatial integral	25
4.2.3 Force contribution coefficients, RHS terms	26
4.2.4 Force dominance factors, RHS terms	27

5 QoIs and Data Collected - Volcán de Colima BAF	29
5.1 Observable outputs overview - MC model	29
5.1.1 Average flow Height, local measurements.	29
5.1.2 Average flow Speed, local measurements.	30
5.1.3 Average Froude Number, local measurements.	31
5.2 Observable outputs - six selected locations	32
5.2.1 Flow Height, selected measurements	32
5.2.2 Flow Speed, selected measurements	33
5.2.3 Froude Number, selected measurements	35
5.2.4 Flow Acceleration, selected measurements	36
5.2.5 Flow area and spatially averaged measurements	37
5.3 Statistical analysis of dynamic quantities	38
5.3.1 Forces, spatial integral	38
5.3.2 Powers, spatial integral	40
5.3.3 Force contribution coefficients, RHS terms	41
5.3.4 Force dominance factors, RHS terms	41
6 Discussion	44
7 Conclusions	44

Abstract

Dense large scale granular avalanches are a complex class of flows with physics that has often been poorly captured by models that are computationally tractable. Sparsity of actual flow data (usually only *a posteriori* deposit information is available), and large uncertainty in the mechanisms of initiation and flow propagation, make the modeling task challenging, and a subject of much continuing interest. Models that appear to represent the physics well in certain flows, may turn out to be poorly behaved in others, due to intrinsic mathematical or numerical issues. Nevertheless, given the large implications on life and property, many models with different modeling assumptions have been proposed.

While inverse problems can shed some light on parameter choices, it is difficult to make firm judgments on the validity or appropriateness of any single or set of modeling assumptions for a particular target flow, or potential flows, that needs to be modeled for predictive use in hazard analysis. We present here an uncertainty quantification based approach to carefully analyze the effect of several modeling assumptions on quantities of interest in simulations based on three established models, i.e Mohr-Coulomb, Pouliquen-Forterre and Voellmy-Salm. In doing this, we take advantage of the versatile implementation of all the models on the same infrastructure, given by TITAN2D.

Statistical analysis is performed on spatially averaged dynamical quantities, but also focusing on locally sampled points of interest. This enables us to exploit the significant differences that remain hidden in the averaged analysis. The fundamental focus of this paper is the exploration of the dynamics of the simulated flows, enabling a notion of the contribution of different mechanisms or models elements inside the simulation procedure, in a fully quantitative, predictive-use oriented and statistical framework.

1 Geophysical mass flows

Geophysical mass flows include debris and mud flows, landslides, snow and rock avalanches, glacier flows, pyroclastic surges, block and ash flows, and pumice flows, lahars, jökulhaups and many other examples. These flows are sometimes tens of kilometers in length and may travel at speeds as fast as hundreds of meters per second. Their deposits can be as much as tens of meters deep and kilometers long. In other words, there is no single universal description of a “typical” geophysical mass flow. Different types of flows are the results of different types of mechanisms/processes and hence different types of flows will have significantly different physical characteristics.

The rheology complexity of the fluidized material, and the mathematical problem of modeling and computing, make the description of the dynamics of those flows really challenging. In many cases the flows are *shallow*, i.e. the horizontal dimension is significantly larger than the flow depth. This assumption allows to perform depth-integration on the governing 3D Navier-Stokes equations, resulting in the 2D formulation of Shallow Water Equations (SWE), also known as Saint Venant Equations (Batchelor, 2000; Luca et al., 2016). Pioneering work of Savage and Hutter (1989) that was followed by Hutter et al. (1993); Dade and Huppert (1998) developed a depth-averaged model for flow of granular materials. Their model was used to model a flow of granular material down an inclined plane, originally using the Mohr-Coulomb rheology (MC) (see also Jaeger et al. (1989); Fracccarollo and Toro (1995)). Afterwards, large number of studies focused on the modeling of granular flows, including geophysical mass flows, using SWE approach and many of them were carefully reviewed in Pudasaini and Hutter (2007).

Modeling flow of granular material down an inclined plane was explored in detail by several further studies, both theoretically and experimentally (Pouliquen, 1999; Ruyer-Quil and Manneville, 2000; Silbert et al., 2001; Bursik et al., 2005; DaCruz et al., 2005). Granular material slumping (Balmforth and Kerswell, 2005; Lajeunesse et al., 2005), rapid flow down smooth inclines (Greve et al., 1994; Wieland et al., 1999) and shock waves (Gray et al., 2003; Hokanardottir and Hogg, 2005) were modeled and tested. Terrain erosion effects were investigated (Pitman et al., 2003a; Edwards and Gray, 2015), and also material deposition and self-channeling effects (Mangeney-Castelnau et al., 2005, 2007).

In particular, the experiments on rough inclined planes led to the development of the Pouliquen-Forterre rheology (PF), assuming a variable frictional behavior as a function of flow regime (i.e. Froude Number, Fr) and flow depth (Pouliquen, 1999; Forterre and Pouliquen, 2002; Pouliquen and Forterre, 2002; Forterre and Pouliquen, 2003). They allowed for an improved modeling of front propagation, mass spreading, surface wave-propagation and vortices-evolution in the flows on a rough terrain (Forterre, 2006; Jop et al., 2006; Forterre and Pouliquen, 2008).

In parallel to and sometimes anticipating the earth avalanches experiments and models, study of snow avalanches led to the development of the Voellmy-Salm rheology (VS) (Voellmy, 1955; Salm et al., 1990; Salm, 1993; Bartelt et al., 1999). Dense snow or debris avalanches consist of mobilized, rapidly flowing ice-snow mixed to debris-rock granules (Bartelt and McArdell, 2009). The VS rheology assumes a velocity dependent resisting term in addition to the traditional basal friction, ideally capable of including an approximation of the turbulence-generated dissipation. Many experimental and theoretical studies were developed in this framework (Gruber and Bartelt, 2007; Kern et al., 2009; Christen et al., 2010; Fischer et al., 2012).

In Iverson (1997); Iverson and Denlinger (2001); Denlinger and Iverson (2001, 2004); Iverson et al. (2004), the depth-averaged model was further studied and applied in the simulation of test geophysical flows in large scale flume experiments. Moreover, Gray et al. (1999, 2003) tested modeling of fast avalanches, exploring the high-velocity effects of channelizing/chuting topographies. A compensation for the effect of earth pressure changes was implemented and explored in detail (Pirulli et al., 2007; Pirulli and Mangeney, 2008), as well as the implementation of a significant curvature in the terrain (Pudasaini and Hutter, 2003; Fischer et al., 2012). Several specific studies on the pore pressure effects on the flow initiation and fluidization were developed (Savage and Iverson, 2003; Iordanoff and Khonsari, 2004; Iverson and George, 2014). A two-phase model was also implemented to more accurately simulate heterogenous flows with a significant portion of interstitial fluid (Pitman and Le, 2005). *All of these complex modeling choices correspond to alternative or additional physical assumptions, and they are sometimes very difficult to evaluate, compare or reasonably combine together.*

A particular interest is raised by the specific efforts devoted to the modeling of volcanic mass flows with SWE (Freundt and Bursik, 1998; Pitman et al., 2003b; Bursik et al., 2005; Saucedo et al., 2005; Kelfoun and Druitt, 2005; Charbonnier and Gertisser, 2009; Kelfoun et al., 2009; Procter et al., 2010;

Sulpizio et al., 2010; Kelfoun, 2011; Charbonnier et al., 2013). Volcanoes are great sources for a rich variety of geophysical flow types and provide field data from past flow events.

In this study, we use the open source TITAN2D software for simulation of granular flows over natural terrains (represented by Digital Elevation Models (DEM)). TITAN2D solves depth-averaged equations using state of the art numerical methodology like adaptive mesh refinement, parallel computing (Pitman et al., 2003b; Patra et al., 2005, 2006; Yu et al., 2009), special methods for wet-dry interface capture (Aghakhani et al., 2016) and finds much use in hazard analysis of such flows using uncertainty quantification methods. The 4th release of TITAN2D offers multiple rheology options (MC, PF and VS rheologies) in the same computational platform. We leverage this capability and focus on modeling characteristics of these rheology options without concern for effects of diverse numerical methods. So far, TITAN2D achieved many successful applications in the simulation of different geophysical mass flows with specific characterisitcs (Sheridan et al., 2005; Rupp et al., 2006; Norini et al., 2009; Charbonnier and Gertisser, 2009; Procter et al., 2010; Sheridan et al.; Sulpizio et al., 2010; Capra et al., 2011). Several studies involving TITAN2D were recently directed towards a statistical study of geophysical flows, focusing on uncertainty quantification and propagation (Dalbey et al., 2008; Dalbey, 2009; Stefanescu et al., 2012a,b), or on the more efficient production of hazard maps (Bayarri et al., 2009; Spiller et al., 2014; Bayarri et al., 2015; Ogburn et al.).

This study for the first time applies a statistical approach to the detailed investigation of the material model. Quantitative statistical analysis of *stress components* and their associated *powers*, as well as the *Froude Number Fr*, the *acceleration* and observable quantities as the flow *velocity*, *height*, *lateral extent*, and *area* over the full range of potential flows is obtained here. The stress components have a strong link with terms in the equations, while *Fr* can give information on the flow regime; moreover, the observable quantities have a direct link to field data and hazard assessments. *Our main purpose is to obtain a quantitative and statistical understanding of the consequences of the different physical assumptions, both on the forces inside the flow and on the observable outputs in time and space.*

In particular, what we present is a procedure for the improved exploration and quantitative comparison of physical models and their assumptions through the collection of full statistical data. Behind each physical model there are different physical assumptions, and therefore it is more appropriate to look at those instead than at the entire model results. Our statistical approach shall enable a first step towards a data driven selection of the best modeling assumptions to use.

2 Overview of the models

2.1 Modeling Assumptions

The models of geophysical mass flows described in this study rely on several physical and mathematical assumptions. We will classify them in two groups - the general assumptions and the rheology assumptions. The main focus of this study is on the latter group, but, in principle, the same procedure could be applied to the former.

General Assumptions

- The *shallowness* approximation is at the base of the depth-averaging procedure. In this approximation, the flow depth is assumed to be at least an order of magnitude less than the characteristic length of the flowing material. Variation of velocity within the flow depth is neglected.
- The material is assumed to be *continuous*. The real flows consist of granular material and, often, interstitial fluid. Usually the “typical particle” diameter is small compared to the depth and length of the flowing mass, and the rheological properties are imposed to approximate the bulk behavior that is expected of an actual mass flow.
- The moving mass is assumed to be *volume preserving* and *incompressible*. In contrast, phenomena of erosion and deposition of material may violate this assumption.
- The body of mass is supposed to be in *isothermal* state or, if not, thermal effects can be ignored.
- The mass flow is assumed to be *free surface*. Air entrainment is instead frequently observed in the dilute real flows.

The shallowness assumption is very important, and brings several implications which may be considered additional assumptions on their own.

Consequences of Shallowness

- The shallowness assumption implies a *hydrostatic* expression for the normal pressure in the direction perpendicular to the basal surface. Moreover, the downslope and cross-slope pressure components are assumed to be varying linearly with the normal pressure component through the flow depth.
- The *boundary layer* where the shearing deformation takes place is collapsed to zero thickness. The sliding and shearing velocity are combined to a single sliding law with a somewhat larger modelled sliding velocity.
- The *lateral shear stresses can be neglected*, compared to the basal shear stresses. Motion of the bulk of mass consists of “shearing within the deforming mass” and “sliding along the basal surface”.

The list rheology assumptions is detailed when the models are presented.

2.2 Governing Equations, Boundary Conditions and Numerical Solver

The motion of the mass flow is described by the basic conservation of mass and momentum for an incompressible medium:

$$\begin{aligned} \nabla \cdot \underline{\mathbf{u}} &= 0, \\ \frac{\partial}{\partial t}(\rho \underline{\mathbf{u}}) + \nabla \cdot (\rho \underline{\mathbf{u}} \otimes \underline{\mathbf{u}}) &= \nabla \cdot \underline{\underline{\mathbf{T}}} + \rho \underline{\mathbf{g}}, \end{aligned} \quad (1)$$

Where $\underline{\mathbf{u}} = [u, v, w]^T$ is the material velocity in cartesian coordinates, ρ is its constant density, $\underline{\underline{\mathbf{T}}}$ is the *Cauchy* stress tensor, and $\underline{\mathbf{g}}$ is the gravity acceleration vector.

The Cauchy stress tensor, $\underline{\underline{\mathbf{T}}}$, depends on the rheology assumptions. The kinetic boundary conditions are defined on the free surface $F^s = s(x, y, t) - z = 0$ and basal surface $F^b = b(x, y, t) - z = 0$ interfaces:

$$\frac{\partial F^s}{\partial t} + \underline{\mathbf{u}} \cdot \nabla F^s = 0, \quad \text{at } F^s(x, y, t) = 0 \quad (2)$$

$$\frac{\partial F^b}{\partial t} + \underline{\mathbf{u}} \cdot \nabla F^b = 0, \quad \text{at } F^b(x, y, t) = 0 \quad (3)$$

The depth-averaged Saint-Venant equations that TITAN2D solves are:

$$\begin{aligned} \frac{\partial h}{\partial t} + \frac{\partial}{\partial x}(h\bar{u}) + \frac{\partial}{\partial y}(h\bar{v}) &= 0, \\ \frac{\partial}{\partial t}(h\bar{u}) + \frac{\partial}{\partial x}\left(h\bar{u}^2 + \frac{1}{2}kg_z h^2\right) + \frac{\partial}{\partial y}(h\bar{u}\bar{v}) &= S_x, \\ \frac{\partial}{\partial t}(h\bar{v}) + \frac{\partial}{\partial x}(h\bar{u}\bar{v}) + \frac{\partial}{\partial y}\left(h\bar{v}^2 + \frac{1}{2}kg_z h^2\right) &= S_y \end{aligned} \quad (4)$$

Here the cartesian coordinate system is aligned such that z is normal to the surface; h is the flow height in the z direction; $h\bar{u}$ and $h\bar{v}$ are respectively the components of momentum in the x and y directions; and k is the coefficient which relates the lateral stress components, $\bar{\sigma}_{xx}$ and $\bar{\sigma}_{yy}$, to the normal stress component, $\bar{\sigma}_{zz}$. The definition of this coefficient depends on the constitutive model of the flowing material we choose. Note that $\frac{1}{2}kg_z h^2$ is the contribution of hydrostatic pressure to the momentum fluxes. S_x and S_y are the sum local stresses: they include the gravitational driving forces, the basal friction force resisting to the motion of the material, and additional forces specific of rheology assumptions.

Let $\mathbf{U} = [h, h\bar{u}, h\bar{v}]^T$ be the vector of conservative variables and $\mathbf{F} = [h\bar{u}, h\bar{u}^2 + 0.5k_{ap}g_z h^2, h\bar{v}\bar{u}]^T$ and $\mathbf{G} = [h\bar{v}, h\bar{u}\bar{v}, h\bar{v}^2 + 0.5k_{ap}g_z h^2]^T$ be the physical flux vectors. In order to solve the system of hyperbolic conservation laws (4), TITAN2D employs a finite volume Godunov solver, and the time-stepping procedure is achieved by an explicit Euler scheme (Pitman et al., 2003b; Patra et al., 2005,

2006). Assuming $\mathbf{S} = [S_h, S_x, S_y]^T$ as the source terms vector containing the effect of the flow rheology, the flow in the next time step updates as:

$$\mathbf{U}_{i,j}^{n+1} = \mathbf{U}_{i,j}^n - \frac{\Delta t}{\Delta x} \{ \mathbf{F}_{i+\frac{1}{2},j}^n - \mathbf{F}_{i-\frac{1}{2},j}^n \} - \frac{\Delta t}{\Delta y} \{ \mathbf{G}_{i,j+\frac{1}{2}}^n - \mathbf{G}_{i,j-\frac{1}{2}}^n \} + \Delta t \mathbf{S}_{i,j} \quad (5)$$

Where $\mathbf{F}_{i\pm\frac{1}{2},j}^n$ and $\mathbf{G}_{i,j\pm\frac{1}{2}}^n$ are the numerical flux terms at the inter-cell boundaries which are computed regarding the Harten-Lax-Van Leer Riemann solver (Toro, 2013). In fact, the evolution of the flow to the next time step depends on the advection flux at the cell interface, which results from the wave interaction at the boundaries between cells. On the other hand, adaptive mesh refinement allows for the concentration of computing power on regions of special interest. It captures the complex flow features along the flow boundaries, as well as the locations where there are large mass or momentum fluxes (which may include places where the topography changes abruptly). Mesh coarsening is also applied where the solution values are relatively constant or small to further improve the computational efficiency (Patra et al., 2005; Aghakhani et al., 2016).

2.3 Rheology assumptions

In the three following sections, we briefly describe *Mohr-Coulomb* (MC), *Pouliquen-Forsterre* (PF) and *Voellmy-Salm* (VS) models.

2.3.1 Mohr-Coulomb model

Based on the long history of studies in soil mechanics (Rankine, 1857), the Mohr-Coulomb rheology model was developed and used to represent the behavior of geophysical mass flows Savage and Hutter (1989).

Shear and normal stress are assumed to obey Coulomb friction equation, both within the flow and at its boundaries. In other words,

$$\tau = \sigma \tan \phi, \quad (6)$$

where τ and σ are respectively the shear and normal stresses on failure surfaces, and ϕ is a friction angle. This relationship does not depend on the flow speed.

Under the assumption of symmetry of the stress tensor w.r.t. the z axis, the earth pressure coefficient $k = k_{ap}$ can take on only one of three values indicated by the square dots shown in Figure 1. The material yield criterion is represented by the two straight lines at angles $\pm\phi$ (the internal friction angle) relative to horizontal direction. Similarly, the normal and shear stress at the bed are represented by the line $\tau = -\sigma \tan(\delta)$ where δ is the bed friction angle. The three possible stress states in the xz -plane are indicated by the square dots. The circular dots show the additional possible stress states for σ_{yy} for a non-axisymmetric stress tensor.

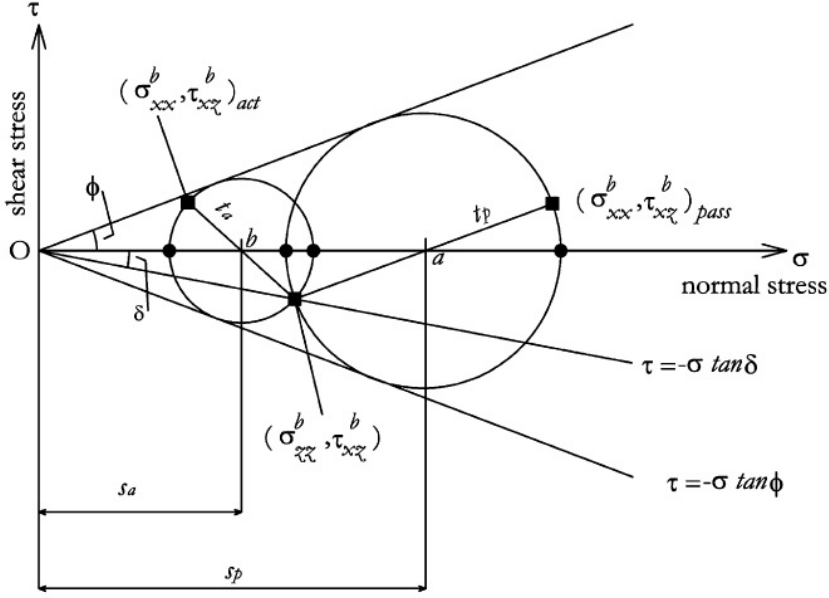


Figure 1: Mohr-circle-diagram representing the stress state within a granular medium (Pirulli et al., 2007).

Regarding the friction angle stated above, we have two material properties in this model:

- Internal friction angle, ϕ_{int} , which resists material shear.
- Bed friction angle, ϕ_{bed} , which resists motion of the material relative to the bed. This is a joint property of the material and the surface it flows over.

It is worth mentioning that the effective value of the friction angles can be strongly reduced by the presence of interstitial fluid, sometimes creating modeling issues. Specific models have been developed in case the effect of interstitial fluid is believed to be particularly relevant (Pitman and Le, 2005).

Earth pressure coefficient $k = k_{ap}$ is defined in MC as:

$$k_{ap} = \begin{cases} \frac{\sigma_{xx}^{b\ act}}{\sigma_{zz}^b} = 2 \frac{1 - \sqrt{1 - \cos^2(\phi_{int})(1 + \tan^2(\phi_{bed}))}}{\cos^2(\phi_{int})} - 1, & \nabla \cdot \tilde{\mathbf{u}} > 0, \text{ active} \\ \frac{\sigma_{xx}^b}{\sigma_{zz}^b} = 1, & \nabla \cdot \tilde{\mathbf{u}} = 0, \text{ neutral} \\ \frac{\sigma_{xx}^{b\ pass}}{\sigma_{zz}^b} = 2 \frac{1 + \sqrt{1 - \cos^2(\phi_{int})(1 + \tan^2(\phi_{bed}))}}{\cos^2(\phi_{int})} - 1, & \nabla \cdot \tilde{\mathbf{u}} < 0, \text{ passive} \end{cases} \quad (7)$$

MC equations As a result, we can write down the source terms of the Eqs. (4):

$$\begin{aligned} S_x &= g_x h - \frac{\bar{u}}{\|\tilde{\mathbf{u}}\|} \left[h \left(g_z + \frac{\bar{u}^2}{r_x} \right) \tan(\phi_{bed}) \right] - h k_{ap} \operatorname{sgn} \left(\frac{\partial \bar{u}}{\partial y} \right) \frac{\partial(g_z h)}{\partial y} \sin(\phi_{int}), \\ S_y &= g_y h - \frac{\bar{v}}{\|\tilde{\mathbf{u}}\|} \left[h \left(g_z + \frac{\bar{v}^2}{r_y} \right) \tan(\phi_{bed}) \right] - h k_{ap} \operatorname{sgn} \left(\frac{\partial \bar{v}}{\partial x} \right) \frac{\partial(g_z h)}{\partial x} \sin(\phi_{int}) \end{aligned} \quad (8)$$

Where, $\tilde{\mathbf{u}} = (\bar{u}, \bar{v})$, is the depth-averaged velocity vector, r_x and r_y denote the radii of curvature of the local basal surface. The inverse of the radii of curvature is usually approximated with the partial derivatives of the basal slope, e.g., $1/r_x = \partial \theta_x / \partial x$, where θ_x is the local bed slope.

MC rheology assumptions In summary:

- *Basal Friction* is based on a constant friction angle.
- *Internal Friction* gives a not negligible contribution and it is based on a constant friction angle.
- *Earth pressure coefficient* formula depends on the Mohr-Coulomb circle.
- Velocity based *curvature effects* are included into the equations.

2.3.2 Pouliquen-Forterre model

The scaling properties for granular flows down rough inclined planes led to a new formulation of the basal friction stress as a function of the flow depth and velocity (Pouliquen, 1999).

Two critical slope inclination angles are defined as functions of the flow thickness, namely $\phi_{start}(h)$ and $\phi_{stop}(h)$. The function $\phi_{stop}(h)$ gives the slope angle at which a steady uniform flow leaves a deposit of thickness h , while $\phi_{start}(h)$ is the angle at which a layer of thickness h is mobilized. They define two different basal friction coefficients:

$$\mu_{start}(h) = \tan(\phi_{start}(h)) \quad (9)$$

$$\mu_{stop}(h) = \tan(\phi_{stop}(h)) \quad (10)$$

An empirical friction law $\mu_b(\|\bar{\mathbf{u}}\|, h)$ is then defined in the whole range of velocity and thickness. The expression changes depending on two flow regimes, according to a parameter β and the Froude number $Fr = \|\bar{\mathbf{u}}\| / \sqrt{hg_z}$.

Dynamic friction regime - $Fr \geq \beta$

$$\mu(h, Fr) = \mu_{stop}(h\beta/Fr) \quad (11)$$

Intermediate friction regime - $0 \leq Fr < \beta$

$$\mu(h, Fr) = \left(\frac{Fr}{\beta} \right)^\gamma [\mu_{stop}(h) - \mu_{start}(h)] + \mu_{start}(h), \quad (12)$$

where γ is the power of extrapolation, assumed equal to 10^{-3} in the sequel (Pouliquen and Forterre, 2002). In particular, if $Fr = \beta$, then $\mu(h, Fr) = \mu_{stop}(h)$, and if $Fr = 0$, then $\mu(h, Fr) = \mu_{start}(h)$.

The functions μ_{stop} and μ_{start} are defined by:

$$\mu_{stop}(h) = \tan \phi_1 + \frac{\tan \phi_2 - \tan \phi_1}{1 + h/\mathcal{L}} \quad (13)$$

and

$$\mu_{start}(h) = \tan \phi_3 + \frac{\tan \phi_2 - \tan \phi_1}{1 + h/\mathcal{L}} \quad (14)$$

The critical angles ϕ_1 , ϕ_2 and ϕ_3 and the parameters \mathcal{L}, β are the parameters of the model.

In particular, \mathcal{L} is the characteristic depth of the flow over which a transition between the angles ϕ_1 to ϕ_2 occurs, in the μ_{stop} formula. In practice, if $h \ll \mathcal{L}$, then $\mu_{stop}(h) \approx \tan \phi_2$, and if $h \gg \mathcal{L}$, then $\mu_{stop}(h) \approx \tan \phi_1$. The effect of the topographic local curvatures is also taken into account.

PF equations The depth-averaged Eqs. (4) source terms thus take the following form:

$$\begin{aligned} S_x &= g_x h - \frac{\bar{u}}{\|\bar{\mathbf{u}}\|} \left[h \left(g_z + \frac{\bar{u}^2}{r_x} \right) \mu_b(\|\bar{\mathbf{u}}\|, h) \right] + g_z h \frac{\partial h}{\partial x} \\ S_y &= g_y h - \frac{\bar{v}}{\|\bar{\mathbf{u}}\|} \left[h \left(g_z + \frac{\bar{v}^2}{r_y} \right) \mu_b(\|\bar{\mathbf{u}}\|, h) \right] + g_z h \frac{\partial h}{\partial y} \end{aligned} \quad (15)$$

PF rheology assumptions In summary:

- *Basal Friction* is based on an interpolation of different friction angles, based on the flow regime and depth.
- *Internal Friction* is neglected.
- *Earth pressure coefficient* is equal to one.
- Normal stress is modified by a *hydrostatic pressure force* related to the flow height gradient.
- Velocity based *curvature effects* are included into the equations.

2.3.3 Voellmy-Salm model

The theoretical analysis of dense snow avalanches led to the VS rheology model (Voellmy, 1955; Salm, 1993). The following relation between shear and normal stresses holds:

$$\tau = \mu\sigma + \frac{\rho\|\underline{\mathbf{g}}\|}{\xi}\|\tilde{\underline{\mathbf{u}}}\|^2, \quad (16)$$

where, σ denotes the normal stress at the bottom of the fluid layer and $\underline{\mathbf{g}} = (g_x, g_y, g_z)$ represents the gravity vector. The VS rheology adds a velocity dependent *turbulent* friction to the traditional velocity independent basal friction term which is proportional to the normal stress at the flow bottom. The two parameters of the model are the bed friction coefficient μ and the turbulent friction coefficient ξ . By dimension analysis, ξ is equivalent to an acceleration, while μ is dimensionless. The decomposition of the total basal friction into velocity independent and dependent parts allows the modeling of either the dynamic regime when the avalanche is flowing with a high velocity in the acceleration zone, and when it is close to stopping in the runout zone.

The effect of the topographic local curvatures is again taken into account by adding the terms containing the local radii of curvature r_x and r_y . In this case the formula is considering the modulus of velocity instead than the scalar component (Fischer et al., 2012).

VS equations Therefore, the final source terms take the following form:

$$\begin{aligned} S_x &= g_x h - \frac{\bar{u}}{\|\tilde{\underline{\mathbf{u}}}\|} \left[h \left(g_z + \frac{\|\tilde{\underline{\mathbf{u}}}\|^2}{r_x} \right) \mu + \frac{\|\underline{\mathbf{g}}\|}{\xi} \|\tilde{\underline{\mathbf{u}}}\|^2 \right], \\ S_y &= g_y h - \frac{\bar{v}}{\|\tilde{\underline{\mathbf{u}}}\|} \left[h \left(g_z + \frac{\|\tilde{\underline{\mathbf{u}}}\|^2}{r_y} \right) \mu + \frac{\|\underline{\mathbf{g}}\|}{\xi} \|\tilde{\underline{\mathbf{u}}}\|^2 \right]. \end{aligned} \quad (17)$$

VS rheology assumptions In summary:

- *Basal Friction* is based on a constant coefficient, similarly to the MC rheology.
- *Internal Friction* is neglected.
- *Earth pressure coefficient* is equal to one.
- Additional *turbulent friction* is based on the local velocity by a quadratic expression.
- Velocity based *curvature effects* are included into the equations, following an alternative formulation.

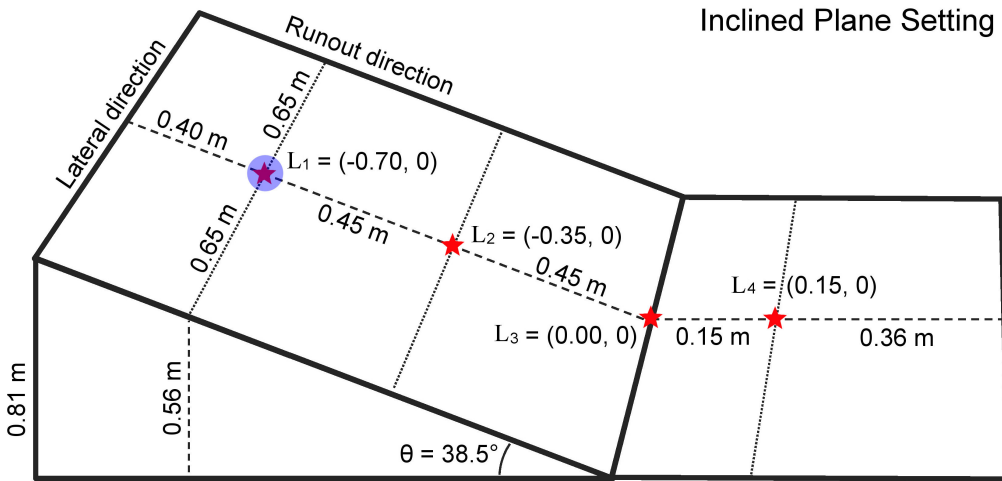


Figure 2: Inclined plane description, including local samples sites (red stars). Pile location is marked by a blue dot.

2.4 Overview of the case studies

The first case study assumes very simple boundary conditions, and corresponds to an experiment fully described in [Webb \(2004\)](#); [Bursik et al. \(2005\)](#); [Webb and Bursik \(2016\)](#). It is a classical flow down an inclined plane set-up, including a change in slope to an horizontal plane (Fig. 2). Four locations are selected among the center line of the flow to accomplish local testing. These are: the initial pile location $L_1 = (-0.7, 0)$ m, the middle of the inclined plane $L_2 = (-0.35, 0)$ m, the change in slope $L_3 = (0, 0)$ m, the middle of the flat plane $L_4 = (0.15, 0)$ m (see Section 4).

The second case study is a block and ash flow down the slope of Volcán de Colima (México) - an andesitic stratovolcano that rises to 3,860 m above sea level, situated in the western portion of the Trans-Mexican Volcanic Belt (Fig. 3). Historically, it has been the most active volcano in México ([la Cruz-Reyna, 1993](#); [Zobin et al., 2002](#); [González et al., 2002](#)). The modeling of pyroclastic flows generated by explosive eruptions and lava dome collapses of Volcán de Colima is a well studied problem ([Martin Del Pozzo et al., 1995](#); [Sheridan and Macas, 1995](#); [Saucedo et al., 2002, 2004, 2005](#); [Sarocchi et al., 2011](#); [Capra et al., 2015](#)). The volcano has been already used as a case study in several research involving the Titan2D code ([Rupp, 2004](#); [Rupp et al., 2006](#); [Dalbey et al., 2008](#); [Yu et al., 2009](#); [Sulpizio et al., 2010](#); [Capra et al., 2011](#); [Aghakhani et al., 2016](#)). During July 10th-11th, 2015, the volcano underwent its most intense eruptive phase since its Subplinian-Plinian 1913 AD eruption ([Saucedo et al., 2010](#); [Zobin et al., 2015](#); [Reyes-Dvila et al., 2016](#); [Capra et al., 2016](#); ?).

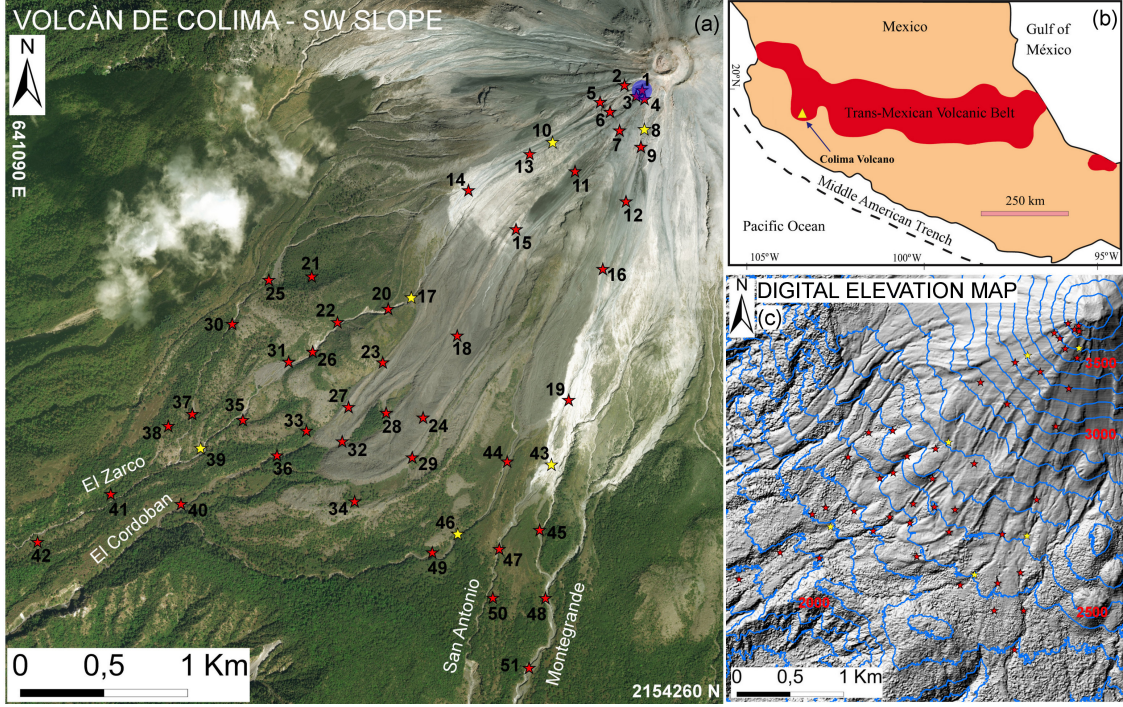


Figure 3: (a) Volcán de Colima (Méjico) overview, including 51 numbered local sample sites (stars) and four labeled major ravines channeling the flow. Pile location is marked by a blue dot. Reported coordinates are in UTM zone 13N. Background is a satellite photo. (b) Regional geology map. (c) Digital elevation map. Six points that are adopted as preferred locations are highlighted in yellow. Elevation isolines are included in blue, elevation values in red.

We assume the flow to be generated by the gravitational collapse of a material pile placed close to the summit area. The volcano already produced either pyroclastic flows generated by lava dome collapse, sometimes called Merapi style flows, or by an eruptive column partial collapse, Soufrière style (?). A dome collapse occurs when there is a significant amount of recently-extruded highly-viscous lava piled up in an unstable configuration around a vent. Further extrusion and/or external forces can cause the still hot dome of viscous lava to collapse, disintegrate, and avalanche downhill (Bursik et al., 2005; ?). Eruptive column collapse can occur during explosive eruptions, when the eruption column can no longer sustain the weight of material due to loss of pressure, and hence it partially collapses down. The hot, dense blocks in this “block and ash” flow (BAF) will typically range from centimeters to a few meters in size. The matrix is composed of fine ash from the comminuted blocks. Computations were performed on a DEM with 5m-pixel resolution, obtained from LiDAR data acquired in 2005 (Davila et al., 2007; Sulpizio et al., 2010). We select 51 locations along the flow inundated area to accomplish local testing. Six of them are then adopted as preferred locations, being representative of different flow regimes (see Section 5).

3 UQ Process

The key to a good forecasting capability in the context of mass flows requires the careful selection of the pair $(M(A), P_{M(A)})$, where A is a set of assumptions, $M(A)$ is the model which combines those assumptions, and P_M is a probability distribution in the parameter space of M . For the sake of simplicity we are always taking P_M uniformly distributed on selected parameter ranges.

Models and assumptions An assumption is a quite general concept - for example it can be a specific equation for the internal stress, the implementation of bed curvature effects, of active-passive

material stretching, or the use of a specific correction on the pressure effects. Assumptions are what makes the models being different, and each model may be seen as the combined result of a set of assumptions. Sometimes a good model contains a useless assumption that may be removed, sometimes a good assumption should be implemented inside a different model - those are usually considered as subjective choices, not data driven. Moreover, the correct assumptions may change through time, making the analysis more difficult. We provided a list of assumptions behind SWE general implementation, and behind each rheology in section 2.

Parameters ranges It is worth mentioning that whereas the support of P_M can be restricted to a single point in case an inverse problem is solved for the optimal reconstruction of a particular flow, this is not possible if we are interested in the general predictive capabilities of the model, i.e. the target of probabilistic hazard assessment. In this study we always assume $P_M \sim \bigotimes_{i=1}^{N_M} Unif(a_{i,M}, b_{i,M})$, where N_M is the number of parameters of M . These parameter ranges will not be selected under the influence of a particular observation, but we will try to use the information gathered in literature about the physical meaning of those values, together with a preliminary testing, coupling the range of possible runouts. This coupling step is detailed in section 3.3, and required to focus the statistical comparison on a consistence range of flow regimes.

Simulated quantities The simulation algorithms can be schematized as:

$$(1) \text{INPUT VARIABLES} \rightarrow (2) \text{HIDDEN DYNAMIC QUANTITIES} \rightarrow (3) \text{OBSERVABLE OUTPUTS}$$

The *input variables* are the parameters of M , i.e. volume, rheology coefficients, but can include also the initiation site and geometry, and the digital elevation map. The *hidden quantities* include the stress terms in the Newton Equations that rule the simulation, and their powers. Those are hidden to the observation in a real flow, but they directly depend on the parameters, and represent a fundamental link between the parameters and the observable outputs. Moreover, the models share some of those terms while change others, and this enables a detailed comparison of the real physics below the curtain (see Sections 4.2, 5.3). Finally, the *observable outputs* include what can be measured in space and time: e.g. flow height, lateral extent, area, velocity, acceleration, and combined quantities as Fr (see Sections 4.1, 5.2). In the sequel (2) and (3) are also called quantities of interest (QoI).

Local samples and spatial averaging The QoI in the previous scheme which are evolving fields $f(\underline{x}, t)$ in space-time, can be either *locally sampled* or *spatially averaged* (see sections 4, 5). The spatial averaging is defined by $F(t) = \int_{\mathbb{R}^k} f(\underline{x}, t) d\underline{x}$. In the most of the cases $k = 2$, and $d\underline{x}$ is given by the area of the mesh elements. Sometimes $k = 3$, e.g. concerning speed, and $d\underline{x}$ is the element of volume corresponding to the mesh elements.

A fundamental part of this research was made possible by the new implementation of a local sampling option in the TITAN2D cyber-infrastructure. In particular, once a set of sample points $(x_i)_{i=1,\dots,N}$ is chosen, each field $f(\underline{x}, t)$ is calculated as a function of time on the elements of the numerical mesh which are found to contain the $(x_i)_{i=1,\dots,N}$. Exploring differences in time and location enable to constrain the changes in flow regime. Those are really important because if the flow behavior is radically different, then the significance and effects of the assumptions may also change.

Monte Carlo simulation In general, for each QoI, during a Monte Carlo simulation we sample the input variables and obtain a family of temporal graphs on time domains depending on the flow duration. These results are statistically summarized - plotting their expectation, and their 5th and 95th percentiles. In the following, we will detail the considered input variables and quantities of interest for each of our cases study.

Our sampling technique of the input variables is based on the Latin Hypercube Sampling (LHS) idea, and in particular, on the improved space-filling properties of the orthogonal array-based Latin Hypercubes (see Appendix 7). The LHS is performed over $[0, 1]^3$ for the MC and VS input parameters, and $[0, 1]^4$ for PF input parameters (see Section 3.3). Those adimensional samples are homothetically transformed to fill the required intervals.

3.1 Statistical analysis of force contributions

A statistical analysis capable of measuring the contributions of different force components in the rheology models is presented. That is helpful to explore and compare the effects of the assumptions behind some modeling choices, onto the time evolution of the flowing material. Let $(F_i(x, t))_{i=1, \dots, 6}$ be the array of force components, where $x \in \mathbb{R}^2$ is a spatial location, and $t \in T$ is a time instant.

In our case study, $(F_1, F_2) := (\mathbf{LHS}_1, \mathbf{LHS}_2)$, i.e. the left-hand side terms in the momentum equation, while $(F_3, \dots, F_6) := (\mathbf{RHS}_1, \dots, \mathbf{RHS}_4)$ are the right-hand side terms. These forces can take different formulations in the different models, which are detailed in section 3.2. This type of procedure can be applied to any additive decomposition of the physical forces. The analysis of RHS can inform on local effects, while LHS concerns the of un-local dynamics in space and time.

In general we show the projection of the forces on the slope direction, or the product with the velocity field, i.e. the power related to them. Hence, in the following the forces are scalar and not vectorial terms. It is important to remark that all the forces are hidden dynamic quantities (see above), depending on the input variables, and they are thus considered as random variables. The degree of contribution of those force terms is significantly variable in space and time, and we define the *contribution coefficients* to model this. The definitions are not depending on the location, but all the results will significantly depend of that choice. Next notation will assume to be in a selected location $x = L_k$, where $k \geq 1$. In the following we will focus on **RHS** forces, although some testing including **LHS** forces has also been accomplished.

Definition 1 (Contribution coefficients) *Let $(F_i)_{i \in I}$ be random variables on (Ω, \mathcal{F}, P) , representing the considered force components in location x at time t . Then, for each component i , the contribution coefficient is defined as:*

$$C_i := \mathbb{E} \left[\frac{F_i}{\Phi} \right],$$

where Φ is a dominating function, i.e. $\Phi \geq |F_i|, \forall i \in I$.

The *total force*, i.e. $\sum_i F_i$ excluding the inertial terms, is not a good candidate for a dominating function. Indeed, the terms often have opposite signs, and their sum can be really small. Another issue is given by the existence of a subset of times Θ characterized by the absence of flow in the selected location x . In Θ the dominant force is null, and cannot be the denominator of a fraction.

We have tested two alternative Φ choices: Φ_1 is based on the l^1 norm, and defined as:

$$\Phi_1 := \begin{cases} \sum_i \frac{|F_i|}{2}, & \text{if not null;} \\ 1, & \text{otherwise.} \end{cases}$$

In contrast Φ_2 is a dominant force based on the l^∞ norm:

$$\Phi_2 := \begin{cases} \max_i |F_i|, & \text{if not null;} \\ 1, & \text{otherwise.} \end{cases}$$

In particular, for a particular location x , time t , and parameter sample ω , we have $C_i = 0$ if there is no flow or all the forces are null. The expectation of C_i is reduced by the chance of F_i being small compared to the other terms, or by the chance of having no flow in (x, t) . Moreover, $\mathbb{E}[C_i] \in [-1, 1], \forall i$.

Proposition 2 *Let $\Phi_k, k = 1, 2$ be the functions described above. Then they are well defined dominating function, i.e. $\Phi_k \geq |F_j|, \forall j, k$.*

Proof. If $k = 1$, the Newton equation states $\sum_{j \in J} F_j = \sum_{i \in I} F_i$, where $(F_j)_{j \in J}$ are inertial forces, and $(F_i)_{i \in I}$ the local forces. Then, $\forall h \in I$

$$F_h = \sum_{i \neq h, i \in I} F_i - \sum_{j \in J} F_j.$$

And hence

$$|F_h| \leq |F_h| + \sum_{i \neq h, i \in I} |F_i| - \sum_{j \in J} |F_j| = 2\Phi_1.$$

A similar equation is valid $\forall k \in J$. If $k = 2$, or if the inertial forces are not included, the proof is trivial. \square

Furthermore, assuming $\Phi = \Phi_2$, there is a useful result explaining the meaning of those coefficients through the conditional expectation.

Proposition 3 Let $(F_i)_{i \in I}$ be random variables on (Ω, \mathcal{F}, P) , representing the considered force components in location x at time t . For each i , let C_i be the contribution coefficient of force F_i , assuming $\Phi = \Phi_2$. Then we have the following expression:

$$C_i = \sum_j p_j \mathbb{E} \left[\frac{F_i}{|F_j|} \mid \Phi = |F_j| \right],$$

where $p_j := P \{ \Phi = |F_j| \}$.

Proof. Let Z be a discrete random variable such that, for each $j \in \mathbb{N}$, $(Z = j) \iff (\Phi = |F_j|)$. Then, by the rule of chain expectation:

$$\begin{aligned} C_i &= \mathbb{E} \left[\frac{F_i}{\Phi} \right] = \mathbb{E} \left[\mathbb{E} \left[\frac{F_i}{\Phi} \mid Z = j \right] \right] = \\ &= \mathbb{E} \left[\mathbb{E} \left[\frac{F_i}{|F_j|} \mid Z = j \right] \right] = \sum_j P \{ Z = j \} \mathbb{E} \left[\frac{F_i}{|F_j|} \mid Z = j \right]. \end{aligned}$$

Moreover, by definition, $p_j = P \{ Z = j \}$. This completes the proof. \square

The last proposition brings to the definition of the *dominance factors* $(p_j)_{j=1,\dots,k}$, i.e. the probability of each F_j to be the dominant force in (x, t) .

Definition 4 (Dominance factors and conditional contributions) Let $(F_i)_{i=1,\dots,k}$ be random variables on (Ω, \mathcal{F}, P) , representing arbitrary force components in location x at time t . Then, for each pair of components (i, j) , the conditional contribution $C_{i,j}$ is defined as:

$$C_{i,j} := \mathbb{E} \left[\frac{F_i}{|F_j|} \mid \Phi = |F_j| \right],$$

where $\Phi = \Phi_2$ is the dominant force. In particular, for each component i , the dominance factor is defined as:

$$p_j := P \{ \Phi = |F_j| \}.$$

In sections 4.2.4 and 5.3.4 we display the contribution coefficients as a function of time, assuming $\Phi = \Phi_2$. Moreover, we report the dominance factors plots, another very useful tool to read the dynamic significance of the forces as a function of time and location.

3.2 Forces terms definition

Forces analyzed have been classified according to the terms of the momentum equation in (4). Moreover, the forces terms in S_x have been additionally classified, accordingly to equations (8), (15), (17), describing the three rheology models considered in this study. What follows is a summary of the force terms, and this notation will be used in the following (see Sections 4.2, 5.3).

Left-hand side, LHS forces

$$\mathbf{LHS}_1 = \left[\frac{\partial}{\partial t}(h\bar{u}), \frac{\partial}{\partial t}(h\bar{v}) \right], \quad (18)$$

it is the temporal derivative of momentum.

$$\mathbf{LHS}_2 = \left[\frac{\partial}{\partial x} \left(h\bar{u}^2 + \frac{1}{2}kg_z h^2 \right) + \frac{\partial}{\partial y}(h\bar{u}\bar{v}), \frac{\partial}{\partial x}(h\bar{u}\bar{v}) + \frac{\partial}{\partial y} \left(h\bar{v}^2 + \frac{1}{2}kg_z h^2 \right) \right], \quad (19)$$

it is the material derivative of momentum, due to the advection.

Right-hand side, RHS forces

$$\mathbf{RHS}_1 = [g_x h, g_y h], \quad (20)$$

it is the gravitational force term, it has the same formulation in all models.

The formula of basal friction force \mathbf{RHS}_2 depends on the model:

$$\begin{aligned} \mathbf{RHS}_2 &= -hg_z \tan(\phi_{bed}) \left[\frac{\bar{u}}{\|\tilde{\mathbf{u}}\|}, \frac{\bar{v}}{\|\tilde{\mathbf{u}}\|} \right], \text{ in MC model.} \\ \mathbf{RHS}_2 &= -hg_z \mu_b(\|\tilde{\mathbf{u}}\|, h) \left[\frac{\bar{u}}{\|\tilde{\mathbf{u}}\|}, \frac{\bar{v}}{\|\tilde{\mathbf{u}}\|} \right], \text{ in PF model.} \\ \mathbf{RHS}_2 &= -hg_z \mu \left[\frac{\bar{u}}{\|\tilde{\mathbf{u}}\|}, \frac{\bar{v}}{\|\tilde{\mathbf{u}}\|} \right], \text{ in VS model.} \end{aligned} \quad (21)$$

The formula of the force related to the topography curvature, \mathbf{RHS}_3 , also depends on the model:

$$\begin{aligned} \mathbf{RHS}_3 &= h \tan(\phi_{bed}) \left[-\frac{\bar{u}^3}{r_x \|\tilde{\mathbf{u}}\|}, -\frac{\bar{v}^3}{r_y \|\tilde{\mathbf{u}}\|} \right], \text{ in MC model.} \\ \mathbf{RHS}_3 &= h \mu_b(\|\tilde{\mathbf{u}}\|, h) \left[-\frac{\bar{u}^3}{r_x \|\tilde{\mathbf{u}}\|}, -\frac{\bar{v}^3}{r_y \|\tilde{\mathbf{u}}\|} \right], \text{ in PF model.} \\ \mathbf{RHS}_3 &= h \mu \left[-\frac{\bar{u} \|\tilde{\mathbf{u}}\|}{r_x} \mu, 0 \right], \text{ in VS model.} \end{aligned} \quad (22)$$

All the three models have an additional force term, having a different formula and meaning in the three models:

$$\begin{aligned} \mathbf{RHS}_4 &= -hk_{ap} \sin(\phi_{int}) \left[\operatorname{sgn} \left(\frac{\partial \bar{u}}{\partial y} \right) \frac{\partial(g_z h)}{\partial y}, \operatorname{sgn} \left(\frac{\partial \bar{v}}{\partial x} \right) \frac{\partial(g_z h)}{\partial x} \right], \text{ in MC model.} \\ \mathbf{RHS}_4 &= g_z h \left[\frac{\partial h}{\partial x}, \frac{\partial h}{\partial y} \right], \text{ in PF model.} \\ \mathbf{RHS}_4 &= -\frac{\|\mathbf{g}\|}{\xi} \|\tilde{\mathbf{u}}\|^2 \left[\frac{\bar{u}}{\|\tilde{\mathbf{u}}\|}, \frac{\bar{v}}{\|\tilde{\mathbf{u}}\|} \right], \text{ in VS model.} \end{aligned} \quad (23)$$

3.3 Definition and consistency of the input variables

In general, the three rheologies considered in this study, MC, PF, and VS, have totally different parameters. The statistical testing we perform requires to choose the parameter range P_M , and in principle it may be arbitrary. Nevertheless, if the total frictions of the models are not covering a similar span, the statistical comparison is dominated by trivial macroscopic differences, and cannot focus on the rheology details. Some degree of parameter consistency is required between the models.

We can find several instances of parameter choices in literature, and in general the choice depends on the case study. In all the models it is defined a basal friction stress (see RHS_2 in in 4). However, PF interpolates different effective friction angles, while VS includes a velocity based additional term. We tested that a direct correlation of effective friction angles is problematic to do. Hence, we did not follow such approach. In contrast, we make a preliminary testing on the extreme values of the parameter space, i.e. giving ***max volume – min resistance***, and ***min volume – max resistance***.

General definitions We assume what follows to simplify testing. Except when differently specified, parameters are sampled uniformly in linear scale.

- Material Volume V is an additional input parameter in all the models, on the same range.
- In MC, sampled input parameters are ϕ_{bed} , and $\Delta\phi := \phi_{int} - \phi_{bed}$. In particular, $\Delta\phi \in [2^\circ, 10^\circ]$ (Dalbey et al., 2008).
- In PF, sampled input parameters are ϕ_1 , $\Delta\phi_{12} := \phi_2 - \phi_1$, and β . In particular, $\Delta\phi_{12} \in [10^\circ, 15^\circ]$, and $\beta \in [0.1, 0.85]$. Moreover, $\phi_3 = \phi_1 + 1^\circ$, and \mathcal{L} is equal to 1 dm and 1 mm in the two case studies, respectively (Pouliquen and Forterre, 2002; Forterre and Pouliquen, 2003; Gray and Edwards, 2014; Barker et al., 2015).
- In VS, sampled input parameters are μ , and ξ . In detail, ξ uniform sampling is accomplished in log-scale. In fact, values of ξ between 250 and 4,000 m/s^2 have been described for snow avalanches (Salm, 1993; Bartelt et al., 1999; Gruber and Bartelt, 2007).

In summary, MC and VS have three-dimensional parameter spaces, while PF a four-dimensional parameter space.

Flow down an inclined plane In this case study, Dalbey et al. (2008) assumed $\phi_{bed} = [15^\circ, 30^\circ]$, while Webb and Bursik (2016) performed a series of laboratory experiments and found $\phi_{bed} = [18.2^\circ, 34.4^\circ]$. We relied on those published parameter choices to decide a comprehensive parameter range. Figure 4 displays the maps of max flow height and max velocities observed in the extreme cases tested. Simulation options are - `max_time = 2 s`, `height/radius = 1.34`, `length_scale = 1 m`, `number_of_cells_across_axis = 10`, `order = first`, `geoflow_tiny = 1e4` (Patra et al., 2005; Aghakhani et al., 2016). Initial pile geometry is cylindrical.

- **Material Volume:** $[449.0, 607.0] \text{ cm}^3$, i.e. average of 528.0 cm^3 and uncertainty of $\pm 15\%$.
- **Rheology models' parameter space:**

The parameter ranges adopted in this case study are:

MC - $\phi_{bed} \in [18^\circ, 30^\circ]$.

PF - $\phi_1 \in [10^\circ, 22^\circ]$.

VS - $\mu \in [0.22, 0.45]$, $\log(\xi) \in [3, 4]$.

Even if maximum and minimum runout are both matching, the shape and lateral extent of the flow is remarkably different in the max. runout case, according to the three models. In particular, MC model can produce the largest lateral extent, and VS model displays an accentuated wedge-like shape, due to the increased friction in the lateral margins. These features will be detailed in Section 4.1.

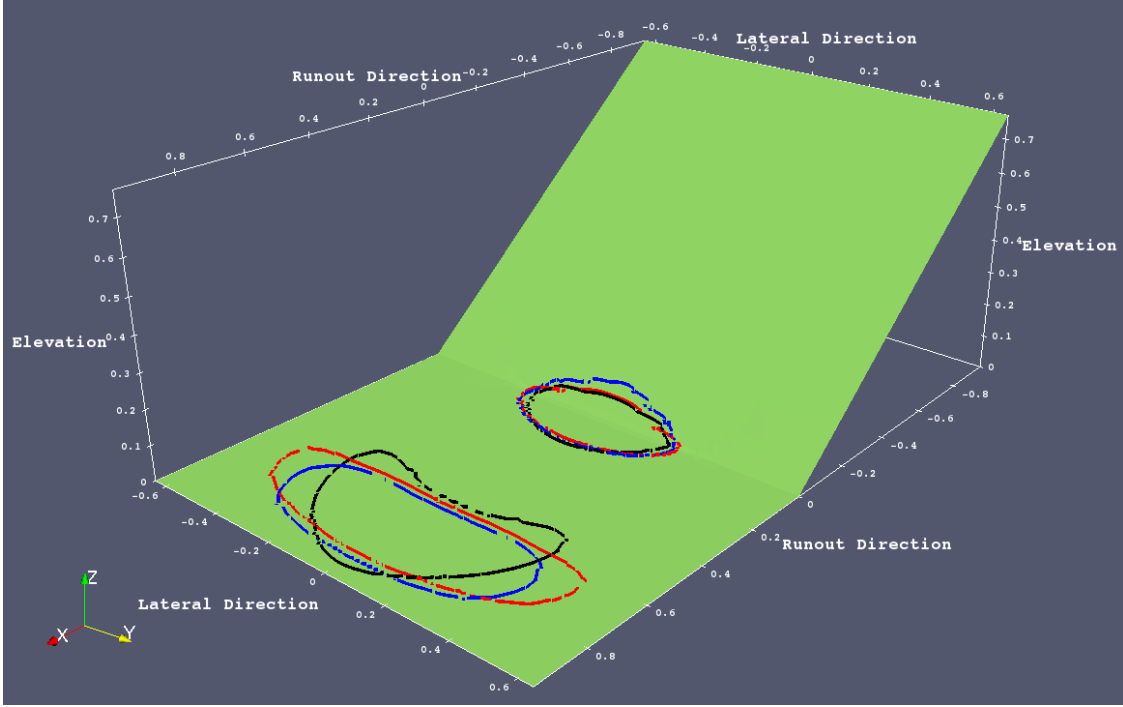


Figure 4: Inclined plane setup. Contours of $h = 1.0$ mm at last simulated snapshot ($t = 1.5$ sec) for simulated flows with *minimum runout obtained from min volume – max resistance*, and *maximum runout obtained from max volume – min resistance*. — : MC, — : PF, — : VS.

Volcán de Colima block and ash flow In this case study, [Dalbey et al. \(2008\)](#) assumed $\phi_{bed} = [15^\circ, 35^\circ]$, while [Capra et al., 2011](#) adopted $\phi_{bed} = 30^\circ$ in the simulation of a BAF in that same setting. Moreover, [Spiller et al. \(2014\); Bayarri et al. \(2015\); Ogburn et al.](#) found a statistical correlation between flow size and effective basal friction inferred from field observation of geophysical flows. The size of the BAF of this study would have $\phi_{bed} = [13^\circ, 18^\circ]$ according to their estimates. Figure 5 displays the maps of max flow height and max velocities observed in the extreme cases tested. Simulation options are - `max_time = 7200 s (2 hours)`, `height/radius = 0.55`, `length_scale = 4e3 m`, `number_of_cells_across_axis = 50`, `order = first`, `geoflow_tiny = 1e4` ([Patra et al., 2005; Aghakhani et al., 2016](#)). Initial pile geometry is cylindrical.

- **Material Volume:** $[2.08, 3.12] \times 10^5 \text{ m}^3$, i.e. average of $2.6 \times 10^5 \text{ m}^3$ and uncertainty of $\pm 20\%$.
- **Rheology models' parameter space:**

The parameter ranges adopted in this case study are:

MC - $\phi_{bed} \in [10^\circ, 25^\circ]$.

PF - $\phi_1 \in [8^\circ, 18^\circ]$.

VS - $\mu \in [0.15, 0.45]$, $\log(\xi) \in [1.7, 4]$.

The models possess different features, even if the maximum runuout after channelization in the ravines is matching. In particular, VS lateral spreading is significant lower and material reaches higher thickness, whereas PF model seems to stop more gradually than MC with a more complex inundated area boundary lines. These features will be detailed in Section 5.2.

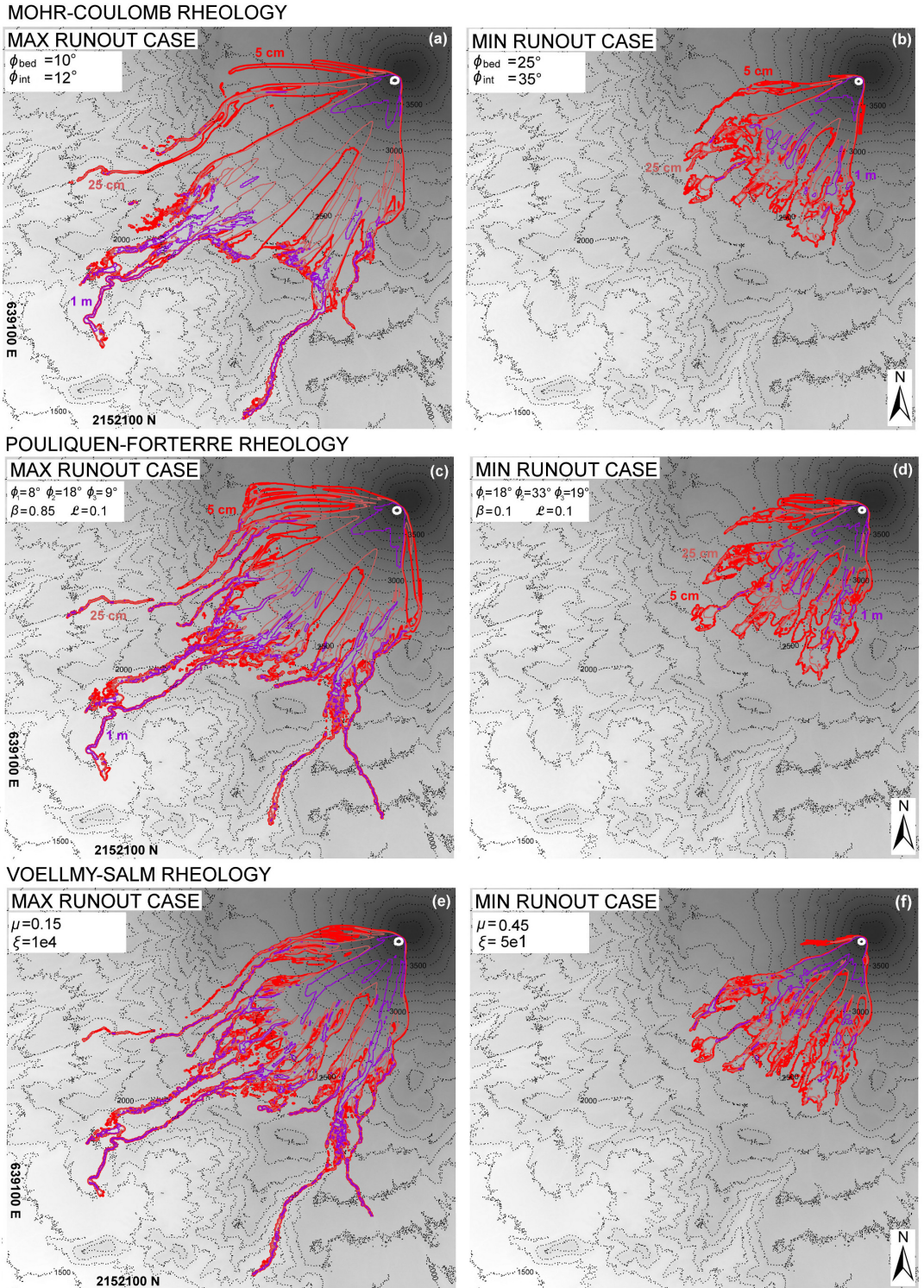


Figure 5: Volcán de Colima BAF. Comparison between *max flow height* maps of simulated flow, assuming Mohr-Coulomb (a),(b), Pouliquen-Forterre (c),(d), and Voellmy-Salm (e),(f) rheology. Extreme cases producing maximum and minimum runout, i.e. (a),(c),(e) ***max volume – min resistance*** and (b),(d),(f) ***min volume – max resistance***.

4 QoIs and Data Collected - Flow down and inclined plane, and a change in slope to a flat plane

First case study is the small scale experimental setting described above. First we describe the observable outputs (Section 4.1), and then the hidden dynamic quantities (Section 4.2). In many plots we note the effect of cutting the flow when height is < 1 mm, which is at the scale of the smallest granular size.

4.1 Observable outputs

Observable outputs include the flow height, speed, Fr , and acceleration as a function of time, measure on the four location L_1, \dots, L_4 displayed in Fig. 2. In addition, max lateral extension, flow area, and spatially averaged speed and Fr are displayed. UQ is also performed, accordingly to the parameter ranges described in Section 3.3.

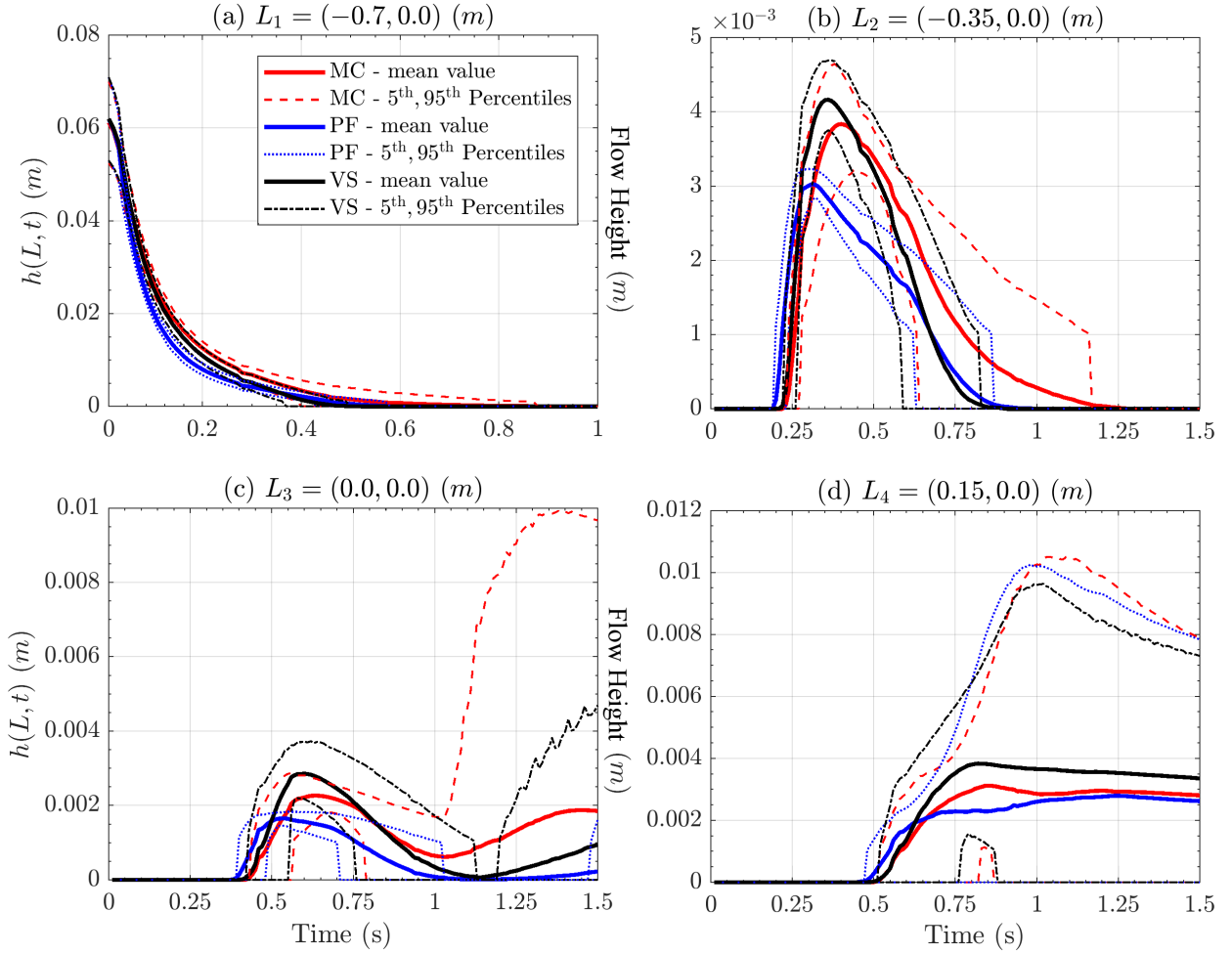


Figure 6: Records of flow height at four spatial locations of interest. Bold line is mean value, dashed/dotted lines are 5th and 95th percentile bounds. Different rheology models are displayed with different colors. Plots are at different scale, for simplifying lecture.

4.1.1 Flow Height, local measurements

Figure 6 shows the flow height, $h(L, t)$, at the points $(L_i)_{i=1,\dots,4}$, for the three rheology models. In plot 6a, related to point L_1 placed on the initial pile, the initial values of ~ 6 cm are the equal and only represent the pile height uncertainty, but then the flow height decreases slightly faster for the PF model, and slower for the MC, compared to the VS. Difference are more significant in plot 6b, related to point L_2 , placed in the middle of the slope. Flow max height is greater for the VS, and smaller for the PF model, which decreases slower after the height peak. However, the value is ~ 15 times smaller than initial pile height, of ~ 4 mm. None of the models leaves a material deposit in L_1 or L_2 , i.e. the 95th percentile of the height is null at the ending-time. In contrast, a deposit is left at points L_3 , i.e. plot 6c placed at the change in slope, and L_4 , i.e. plot 6d in the middle of the flat runout. MC's deposit is higher than the other models' at L_3 , while it is not significantly different at L_4 between the three models. It is of ~ 3 mm in average, but can range from 0 to 8 mm. In plots 6b and 6c the elimination of material when height is < 1 mm, cuts the 95th percentile to zero when its value is below that threshold.

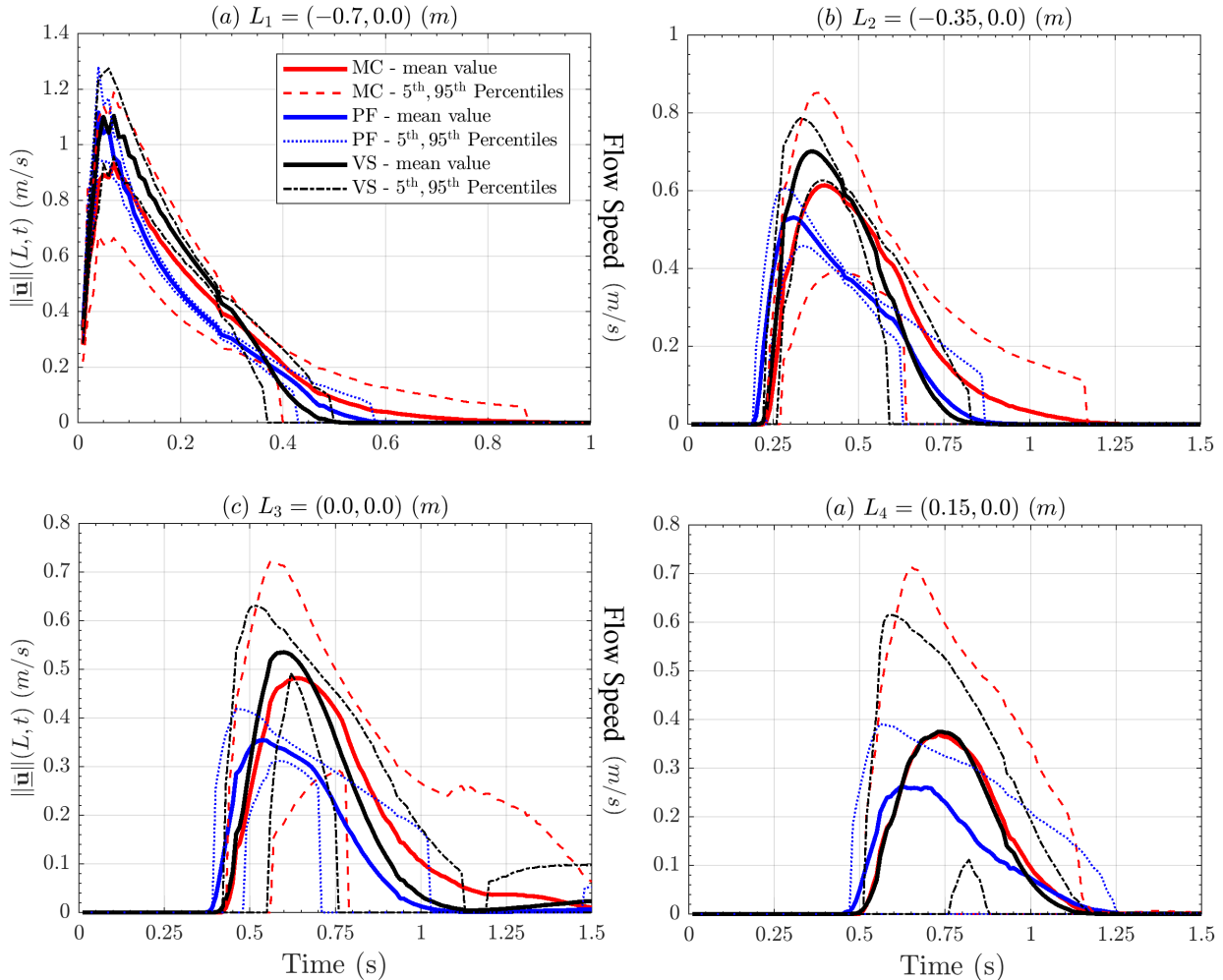


Figure 7: Records of flow speed at four spatial locations of interest. Bold line is mean value, dashed/dotted lines are 5th and 95th percentile bounds. Different rheology models are displayed with different colors. Plots are at different scale.

4.1.2 Flow Speed, local measurements

Figure 7 shows the flow speed, $\|\bar{\mathbf{u}}\|(L, t)$, at the points $(L_i)_{i=1,\dots,4}$, for the three rheology models. In plots 7a and 7b, related to points L_1 and L_2 , speed peaks are similar between the models, at ~ 1 m/s and ~ 0.6 cm/s, respectively. In plot 7a VS peak is higher, but then its speed decreases more linearly, while MC and PF have a more concave profile, making MC the faster model after 0.3 sec. In plot 7b it is the PF model to decrease more linearly. UQ shows that MC model uncertainty is remarkably larger than in the other models, and produces higher values in the 95th percentile plots. Lowest speed values are affected by the elimination of material below 1 mm flow height threshold. In plots 7c and 7d, related to points L_3 and L_4 , the PF velocity profile is significantly lower than the other models, but it also decreases slower, and matches with the stopping times of them. Speed in the deposits is below 0.1 m/s in L_3 , negligible in L_4 .

4.1.3 Froude Number, local measurements

Figure 8 shows the Froude Number, $\|\bar{\mathbf{u}}\|/\sqrt{gh}$, at the points $(L_i)_{i=1,\dots,4}$, for the three rheology models.

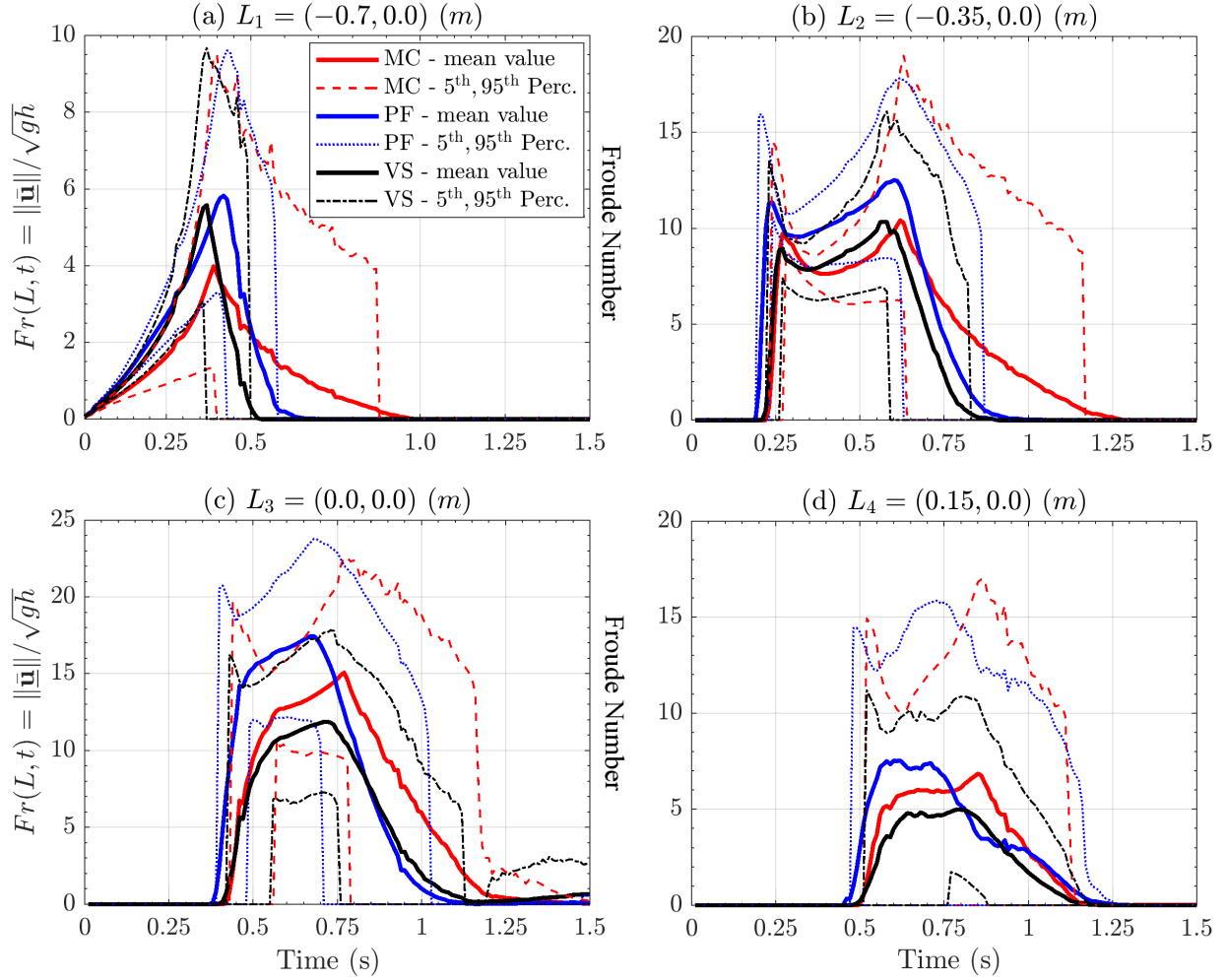


Figure 8: Records of Froude number at four spatial locations of interest. Bold line is mean value, dashed/dotted lines are 5th and 95th percentile bounds. Different rheology models are displayed with different colors. Plots are at different scale.

Froude Number combines the estimates of flow height and speed, described above. In plot 8a, related to point L_1 , Fr maximum average value is smaller for the MC model, ~ 4 , than for the others, ~ 6 . However, UQ tells us that 95th percentile almost reaches ~ 10 in all the three models. After the peak, the values decrease slower and more concavely in MC model than in the others. In plot 8b, related to point L_2 , Fr shows a bimodal profile in time, with two separate peaks at ~ 10 on average, but reaching ~ 18 in the 95th percentile plot. In fact, first maximum, at ~ 0.25 s is due to the speed peak, and second, at ~ 0.6 s is related to \sqrt{h} decreasing while the speed is not significantly changing. In plot 8c and 8d, related to points L_3 and L_4 , bimodality is less accentuated and becomes a plateau profile in $\sim [0.5, 0.75]$ sec. PF model gives significantly larger Fr values, even > 20 at L_3 , due to a larger speed and a thinner flow. It is worth noting, for the sake of PF model, that $Fr > \beta$ and the flow is in the dynamic regime during the most of the time.

4.1.4 Flow Acceleration, local measurements

Figure 9 shows the flow speed, $\|\mathbf{a}\|(L_i, t)$, at the points $(L_i)_{i=1,\dots,4}$, for the three rheology models.

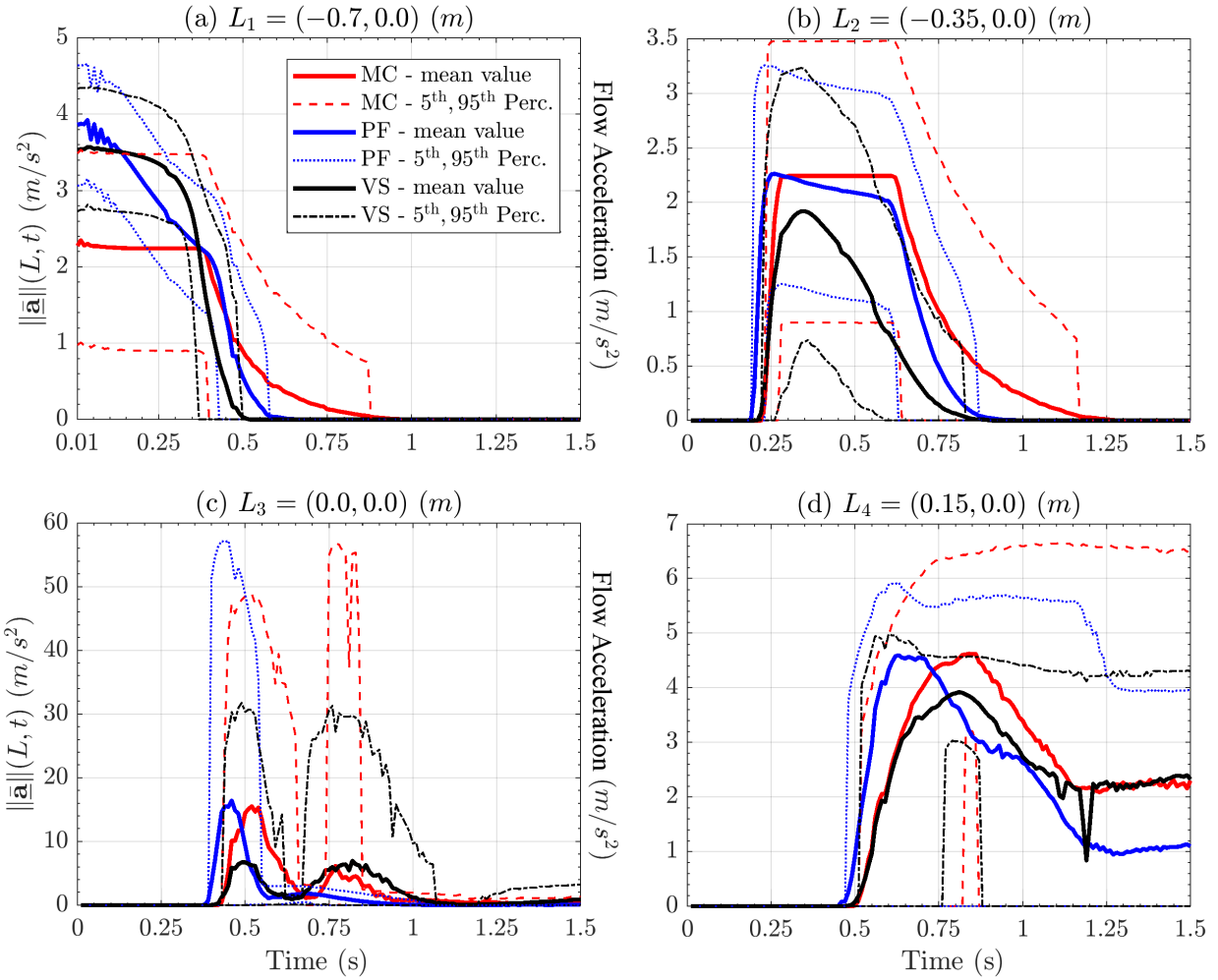


Figure 9: Records of flow acceleration magnitude (computed from LHS). Bold line is mean value, dashed lines are 5th and 95th percentile bounds. Different rheology models are displayed with different colors. Plots are at different scale.

Acceleration is the link between force terms and observable motion. We calculated it from the LHS of the dynamical equation, but using the RHS terms produces very similar results, although not identical due to the numerical approximations in our solution. In plot 9a, related to point L_1 , MC and VS show a plateau before ~ 0.4 sec, at $\sim 2.5 \text{ m/s}^2$ and $\sim 3.5 \text{ m/s}^2$, respectively, while PF linearly decreases between those same values. In plot 9b, related to point L_2 , are MC and PF to show a plateau, at $\sim 2.2 \text{ m/s}^2$, while VS has a more bell-shaped profile. UQ tells us that PF has a smaller uncertainty than the other models. In plot 9c, related to point L_3 , all the models show a bimodal profile, with peaks at ~ 0.5 sec and 0.8 sec. This is more accentuated for MC and VS, whereas the second peak is almost absent from PF profile. The second peak is motivated by an increase of velocity in the down-slope direction after its reduction due to lateral spreading of material. At the first peak, acceleration values are significant, with average peaks of MC and PF both at $\sim 15 \text{ m/s}^2$, and 95th percentile plot reaching $\sim 50 \text{ m/s}^2$ and $\sim 55 \text{ m/s}^2$, respectively. VS shows about halved acceleration peak values. At the second peak, average acceleration values are similar for MC and VS, at $\sim 5 \text{ m/s}^2$. In contrast, 95th percentile plot is $> 50 \text{ m/s}^2$ for MC, while $\sim 30 \text{ m/s}^2$ for VS. In plot 9d, related to point L_4 , the acceleration has a first peak at $\sim 4 \text{ m/s}^2$, and a final asymptote at $\sim 2 \text{ m/s}^2$ for MC and VS, $\sim 1 \text{ m/s}^2$ for PF. These values generally mean flow deceleration, and uncertainty is more relevant for MC and PF than for VS.

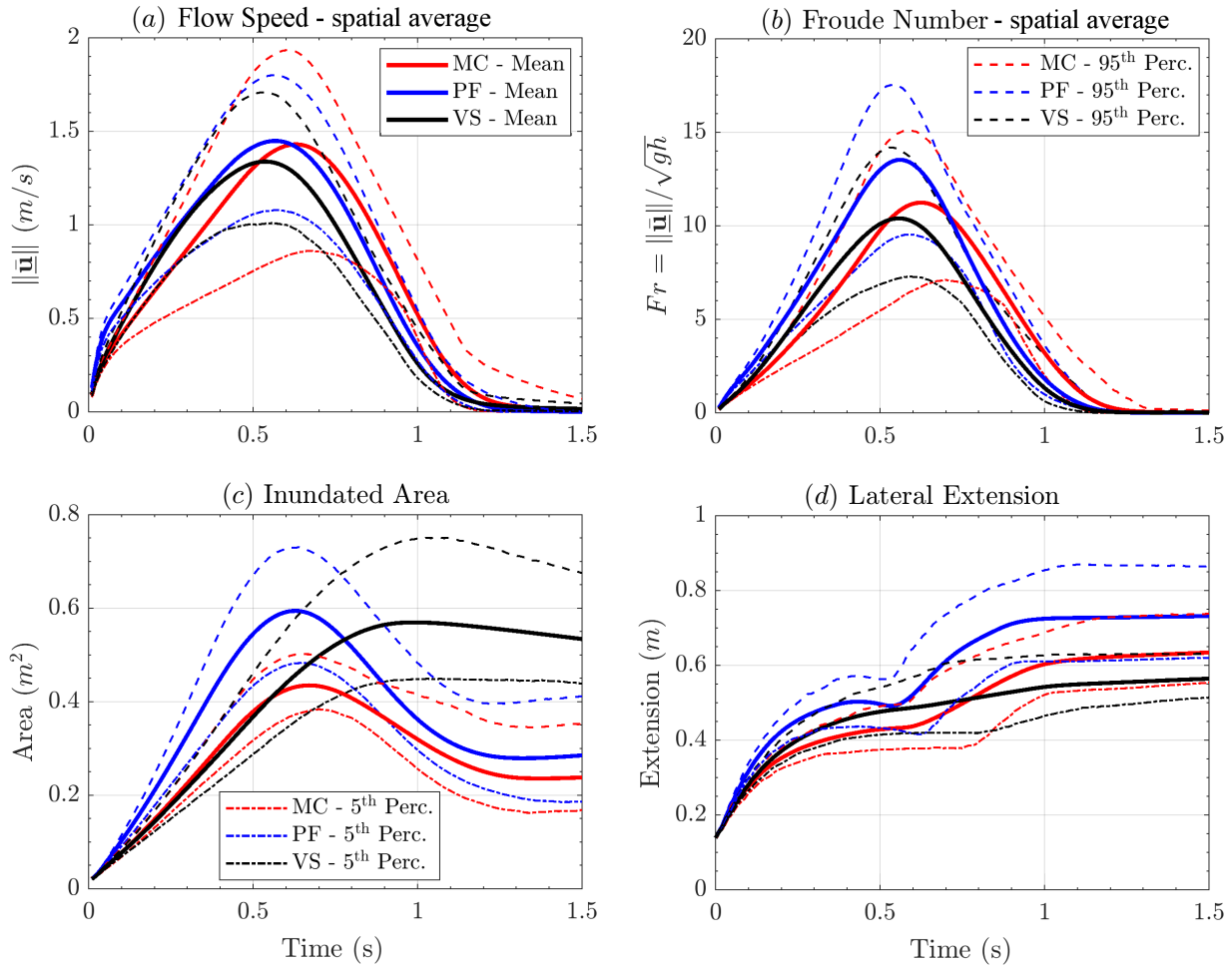


Figure 10: Comparison between spatial averages of (a) flow speed, and (b) Froude Number in addition to the flow (c) lateral extent, and (d) inundated area, as a function of time.

4.1.5 Flow extents and averaged measurements

Figure 10 shows the spatial average of speed and Froude Number, for the three rheology models. Moreover, it shows the (maximum) lateral extent and inundated area of flow, as a function of time. Spatial averages and global quantities as maximum lateral extent and inundated area have smoother plots than local measurements. Most of the details observed in local measurements are not easy to discern. In plot 10a the speed shows a bell-shaped profile in all the models, with an average peak at $\sim 1.4m/s$ and uncertainty range, given by 5th and 95th percentiles, of $\pm 0.4m/s$ for PF and VS. VS is slightly slower, reaching $\sim 1.3m/s$ in the average. MC shows a larger uncertainty range, of $\pm 0.6m/s$. The maximum speed is reached first by VS and PF at $\sim 0.55s$, and last by MC at $\sim 0.65s$. In plot 10b, also Froude Numbers have a bell-shaped profile. Fr peaks are temporally aligned with speed peaks, and are ~ 10 in VS, ~ 11 in MC, ~ 13.5 in PF, on average. Uncertainty range is about ± 4 in all models. In plot 10c inundated area shows similar max values in PF and VS, at $\sim 0.6m^2$ on average, and uncertainty of $\pm 0.15m^2$. MC is lower, at $\sim 0.45m^2$ on average, and less uncertain, $\pm 0.10m^2$. VS does not decrease significantly after reaching the peak, whereas the other models contract their area, to approximately half of the maximum extent. In plot 10d the lateral extent starts equal to the pile diameter $15cm$, and then rises in two stages in MC and PF, the second and greater rise starting at $\sim 0.6s$, corresponding to the time of arrival at the change in slope L_3 (see Fig. 6c). VS rises without showing two phases. After the first phase, average lateral extent is at $\sim 50cm$ in PF and VS, while it is $\sim 43cm$ in MC. Uncertainty range is $\pm 7cm$ for all models at that time. Final extent is $\sim 75cm$ in PF, $\sim 65cm$ in MC, $\sim 55cm$ in VS. Uncertainty range is $\pm 5cm$ in VS, but rises to $\pm 10cm$ in MC and PF.

4.2 Statistical analysis of dynamic quantities

We focus on the force terms and related powers, as well as their statistical analysis. The classification follows the definitions in section 3.2. In particular, all the estimates assume a material density of the flow $\rho = 805kg/m^3$. This a fixed scaling factor, and the plots aspect is not affected by its value.

4.2.1 Forces, spatial integral

Figure 11 shows the spatial sum of the force terms in the slope direction, for the three rheology models. Force sum is performed on half spatial domain, due to the symmetry with respect to the flow central axis. In plot 11a \mathbf{RHS}_1 represents the effect of the gravity in all the models. It starts with a plateau at $\sim 1.3N$ before $\sim 0.55s$, then decreases to zero after the material crosses the change in slope. The force values are consistent with the expression $\rho(V/2)g_x$, representing half the weight of material, projected along the slope direction. Uncertainty range of $\pm 0.2N$ on the peak values. MC decreases slower, and has a more significant uncertainty, after the change in slope. PF decreases faster. In plot 11b \mathbf{RHS}_2 represent the friction at the base of the flow. It is negative and opposed to the gravity. A similar profile is shared by the three models, with a first short-lasting weakening before $\sim 0.1s$, a plateau with a small strengthening after $\sim 0.5s$, and a final waning after $\sim 1s$, at the conclusion of the dynamics. MC does not reach zero, while the other models do. VS values are generally $\sim 0.5N$ weaker than MC, and PF is intermediate, except in the initial peak, where it is the weakest. Strongest forces are reached during the plateau, and are $\sim -0.55N$, $\sim -0.75N$, $\sim -0.9N$, with uncertainty range of $\pm 0.25N$ in the plateau. Uncertainty is reduced in the final stages of VS and PF, but increases in MC. In plot 11c \mathbf{RHS}_3 is related to the curvature effects, and is not null only at the change in slope. It is always negative, i.e. reducing flow velocity, indeed it is equivalent to the friction due to the additional weigh generated by centrifugal forces. Its scale is ten times smaller than the previous plots, with values above $0.1N$ only in MC. VS displays a bimodal profile, with a second and weaker peak at $\sim 0.75s$. In plot 11d \mathbf{RHS}_4 is related to the additional forces of the models, differently characterized. In MC and PF, they are significantly small forces before $0.1s$, completely negligible later. In VS, this is the velocity dependent term. It is negative and plays a significant role. It reaches $\sim 1N$ at the change in slope, with uncertainty $\pm 0.3N$. It is bell shaped and null before $\sim 0.1s$ and after $\sim 1s$. In plot 11e $\sum_{i=1}^4 \mathbf{RHS}_i$ represents the total force in the slope direction, and summarizes the previous plots. The profile is characterized by a positively valued stage at $\sim 0.5N$ before the change in slope, and by a negatively valued stage after that, with bell-shaped profile, and a peak at $\sim -0.5N$. In the first stage MC is more flat, while PF and VS decrease. In the second stage MC is occurring later in time, of $\sim 0.1s$; PF and VS are remarkably similar, but VS wanes faster.

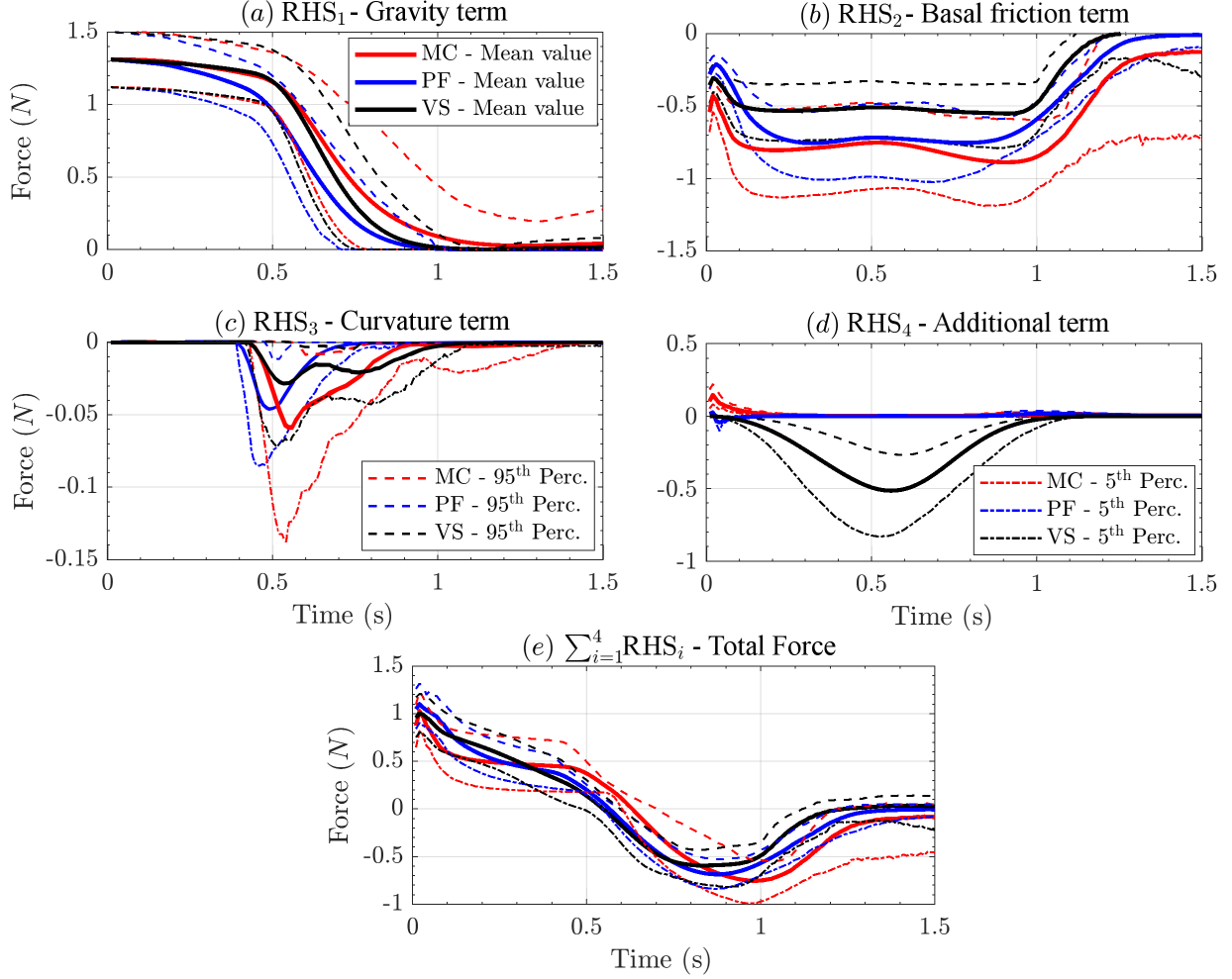


Figure 11: Spatial sum of the RHS forces in the slope direction. Bold line is mean value, dashed lines are 5th and 95th percentile bounds. Scale of plot (c) is ten times larger than in (a),(b),(d); scale of plot (e) is slightly smaller.

4.2.2 Powers, spatial integral

Figure 12 shows the spatial sum of the powers, for the three rheology models. Power sum is performed on half spatial domain, due to the symmetry with respect to the flow central axis. The plots follow the same order used in Fig. 11, but the scalar product with velocity imposes the bell-shaped profile observed in Fig. 10a. In plot 12a the power of RHS_1 starts from zero and rises up to $\sim 1.5W$, with uncertainty of $\pm 0.5W$. In plot 12b the power of RHS_2 is negative and peaks to $\sim 1W$ in MC and PF, $\sim 0.7W$ in VS. The initial ripple observed in Fig. 11b is not observed, nor the plateau. In plot 12c the power of RHS_3 has a similar profile to the force it is weaker than $-0.1W$ on average, although MC uncertainty reaches $\sim -0.25W$. In plot 12d the power of RHS_4 is relevant only in VS, although also in PF has a very short lasting positive peak up to $0.3W$ before to become null at $\sim 0.1s$. Power in VS is $\sim -0.7W$, $\pm 0.3W$. In plot 12e the power of the total force $\sum_{i=1}^4 \text{RHS}_i$ summarizes the energy accumulation and dissipation, following a sinusoid profile. As observed in Fig. 11e, MC profile is delayed of $\sim 0.1s$ compared to the others, and is affected by a larger uncertainty.

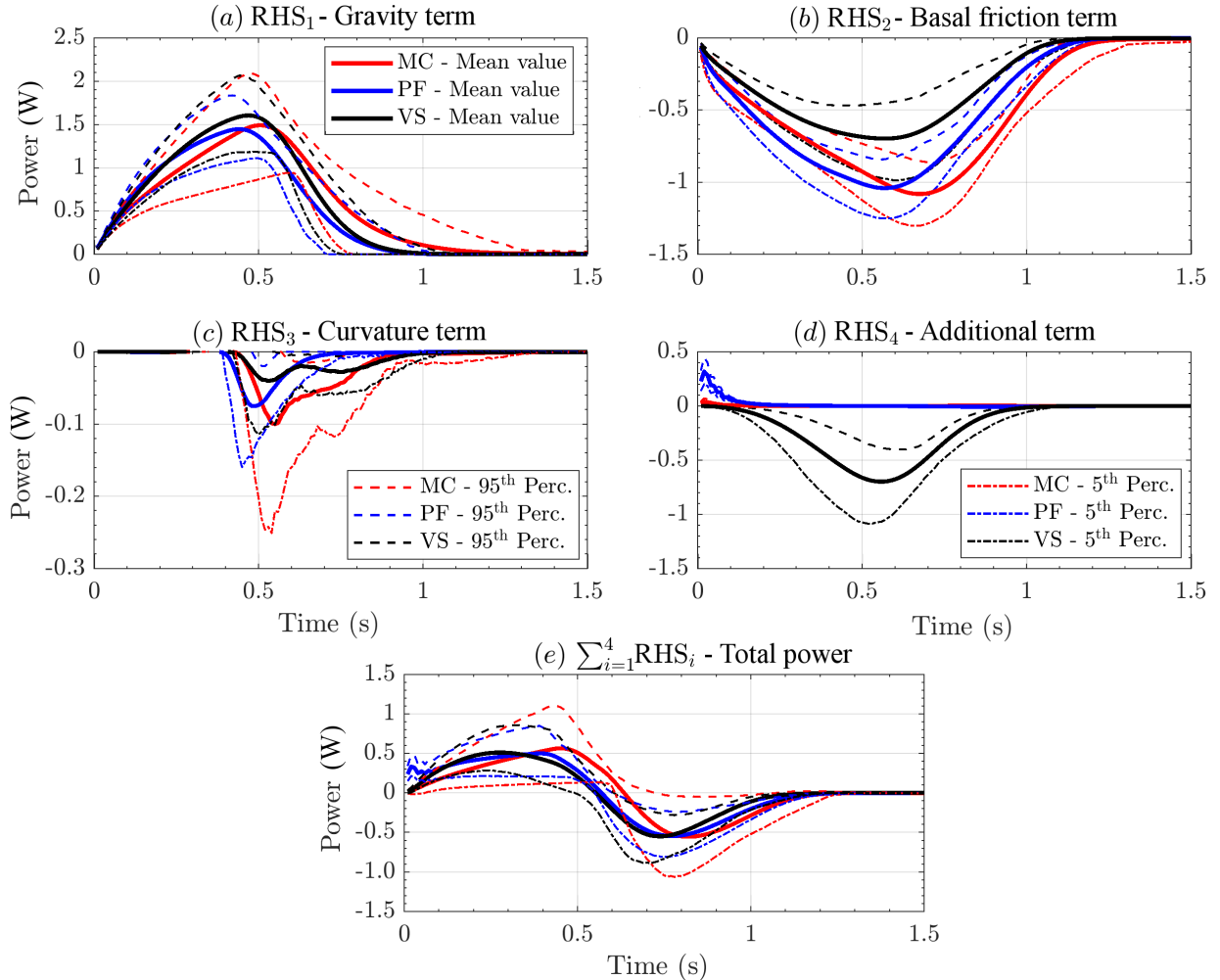


Figure 12: Spatial sum of the RHS powers. Bold line is mean value, dashed lines are 5th and 95th percentile bounds. Model comparison on the mean value is also displayed.

4.2.3 Force contribution coefficients, RHS terms

Figure 13 shows the Contributions Coefficients (C_i) $_{i=1,\dots,4}$, for the three rheology models and focusing on the RHS terms in the slope direction. Force contributions are defined in section 3.1 and are obtained dividing the force terms described in section 3.2 by a dominant function Φ . This is a tool to compare the different force terms, scaling the plots by the dominant function Φ - in this case in $[-1, 1]$. It also represent the degree of relevance of the assumptions behind the force terms, changing as a function of time. The different models are plotted separately: 13a,d,g,j assume MC; 13b,e,h,k assume PF; 13c,f,i,l assume VS. The plots 13a,b,c are related to point L_1 , placed on the initial pile. C_1 and C_2 play the major roles, with a minor contribution C_4 in VS. Contributions profiles are flat plateaus that start to wane after 0.4s, with the rise of the probability of no-flow at the point L_1 (see also Fig. 14). Uncertainty is related to the no-flow times, and to the value of C_2 . The negative contribution C_4 can be significant, as it is shown by the 5th percentile values, but appears after 0.25s. The plots 13d,e,f are related to point L_2 , placed in the middle of the slope. Again the major contributions are C_1 and C_2 , with trapezoidal profile preceded and followed by no-flow. In VS, C_4 becomes as a significant as C_2 , but it is bimodal instead than trapezoidal. The plots 13g,h,i are related to point L_3 , placed at the change in slope. The contributions C_1 and C_2 are still the largest, but their profiles are bell-shaped. In VS, C_4 is almost identical to C_2 . In all the models, C_3 is also significant, with a peak similar to C_2 , but has a different

profiles - triangular for MC and PF, bimodal for VS. In MC the decrease occurs in two stages. The uncertainty tells us that C_3 can also be the dominant force, for a shorter time. Due to the presence of deposit, all the contributions are small (particularly small in PF), but not zero at the ending time. The plots 13j,k,l are related to point L_4 , placed in the middle of the flat runout. Only C_2 has a major role, with a bell shaped profile faster to wax than to wane. Contribution C_4 has a minor role in VS and PF. Uncertainty affects this force, which can be shortly the dominant term, in PF.

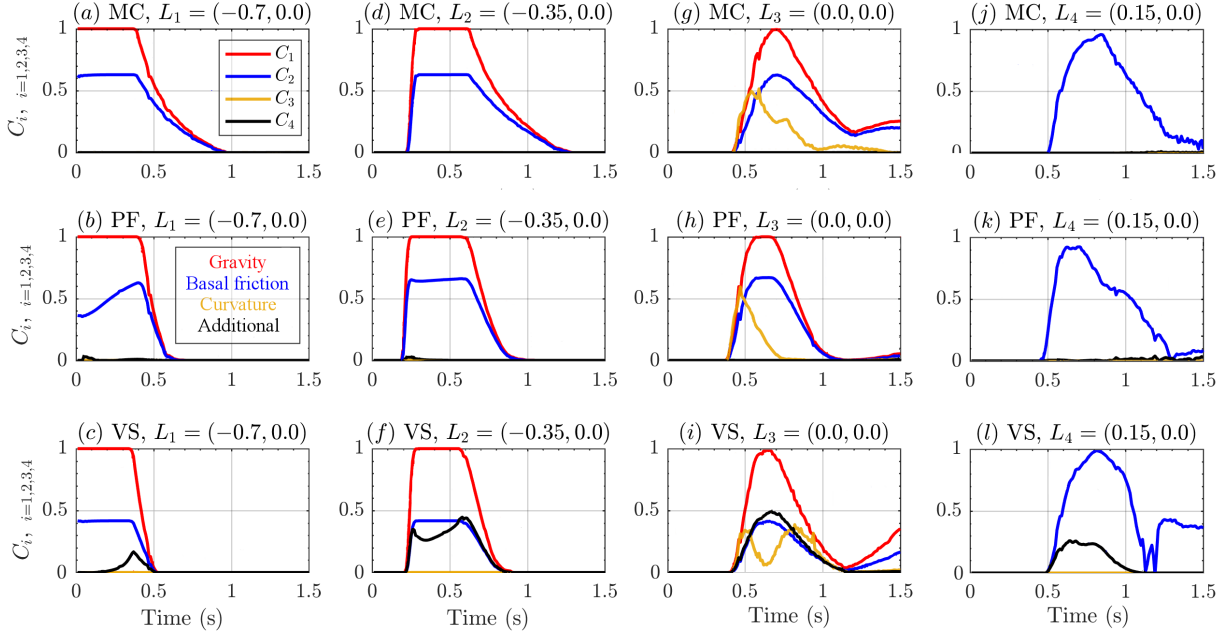


Figure 13: Records of contribution coefficients of **RHS** forces, in the slope direction, in four spatial locations of interest. Different rheology models are displayed with different colors. Dominant function Φ is calculated based on the l^∞ norm (see Section 3.1)

4.2.4 Force dominance factors, RHS terms

Figure 14 shows the Dominance Factors $(P_i)_{i=1,\dots,4}$, for the three rheology models and focusing on the RHS terms in the slope direction. They are defined in section 3.1 and are the probability of each force term (described in section 3.2) to be the maximal one. It is another tool to compare the different force terms, following a more restrictive approach than the Contribution Coefficients. The values are probability values, hence in $[0, 1]$. The plots include also the probability of no-flow in the considered point. Similarly to Fig. 13, the different models are plotted separately: 14a,d,g,j assume MC; 14b,e,h,k assume PF; 14c,f,i,l assume VS. The plots 14a,b,c are related to point L_1 , placed on the initial pile. Only \mathbf{RHS}_1 can be the dominant force, and no-flow probability is $(1 - P_1)$. Same thing in the plots 14d,e,f are related to point L_2 , placed in the middle of the slope. The plots 14g,h,i are related to point L_3 , placed at the change in slope. As observed in Fig. 13, also \mathbf{RHS}_3 can be the dominant term for a short time, with a peak probability of $\sim 30\%$. The plots 14j,k,l are related to point L_4 , placed in the middle of the flat runout. Only \mathbf{RHS}_2 can be the dominant term, except in PF where there is $\sim 10\%$ that \mathbf{RHS}_4 is the dominant term at then ending-time.

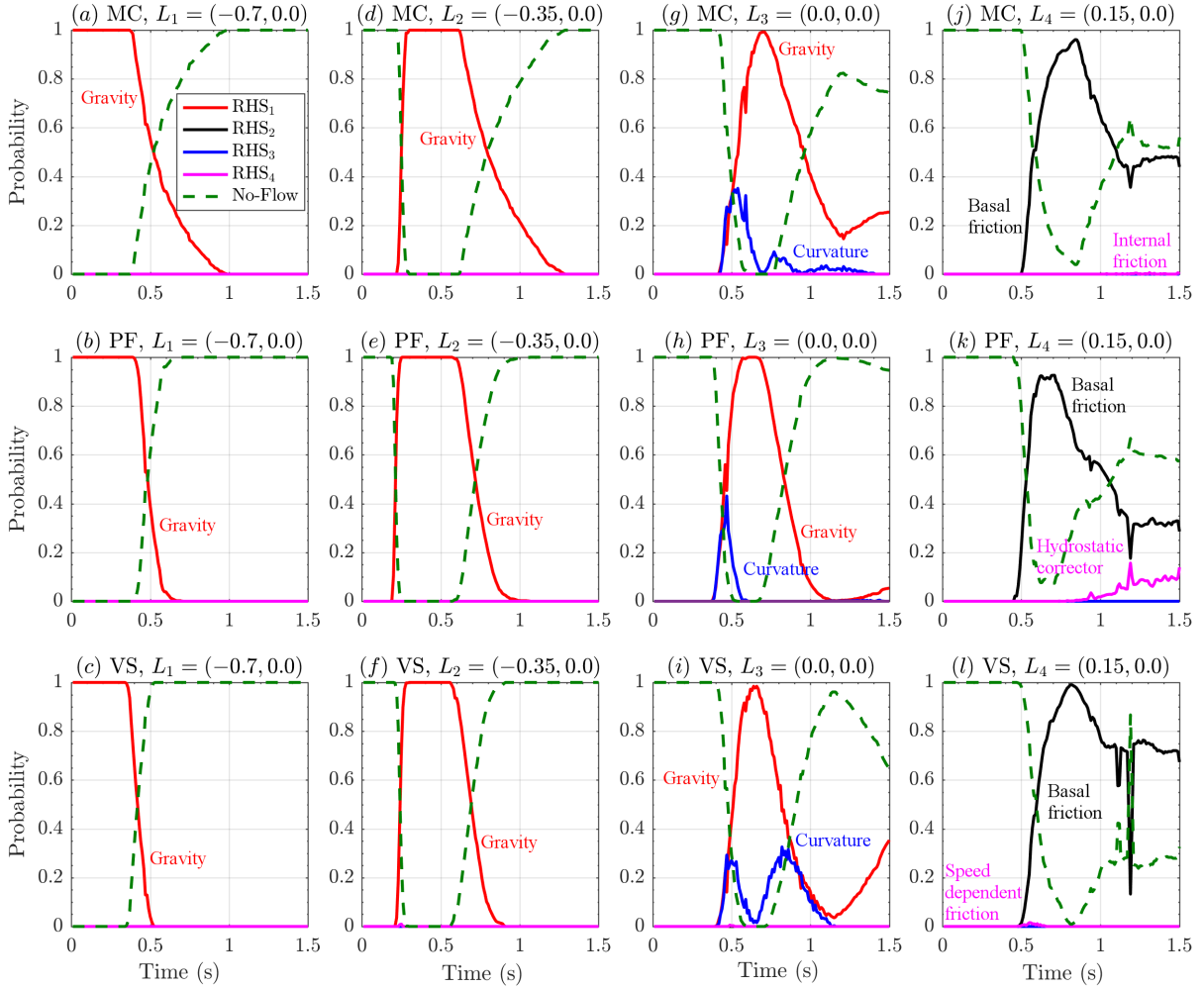


Figure 14: Records of dominance factors of **RHS** forces, in the slope direction, in four spatial locations of interest. Different rheology models are displayed with different colors. No-flow probability is also displayed with a green dashed line.

5 QoIs and Data Collected - Volcán de Colima BAF

5.1 Observable outputs overview - MC model

In our second case study, the number of spatial locations is significantly higher than previously. In fact, we placed 51 points to span the entire inundated area, in search of different flow regimes, displayed in Fig. 3. First we show the average flow height, speed, and Fr in all the locations, then, based on that, we select six points which we find representative of interesting flow regimes. Figures 15, 16, 17 assume MC model, while the results related to PF and VS models are detailed on six selected points.

5.1.1 Average flow Height, local measurements.

Figure 15 shows the flow height, $h(L, t)$, at the 51 spatial locations of interest, according to MC.

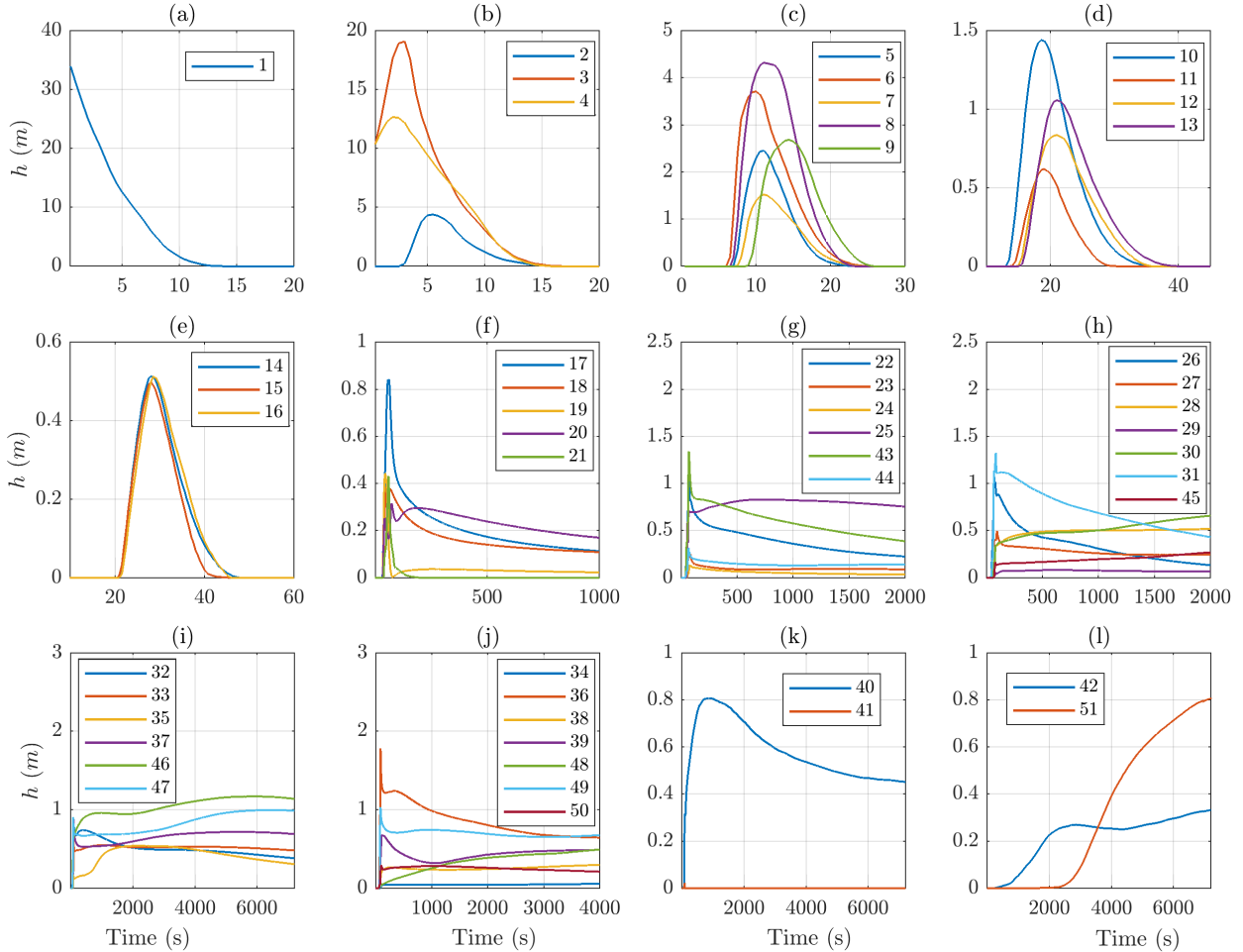


Figure 15: MC model, records of average flow height, $h(L, t)$, in 51 spatial locations of interest (Fig. 3).

Different plots have different scales on either time and space axes. In plot 15a, the only location is set on the center of the initial pile, and the profile is similar to what observed in point L_1 of the inclined plane case study, in Fig. 6a. In particular, the height decreases from the initial value to zero, in about 15 s. In plots 15b,c,d,e, the locations are set at less than ~ 1 km radius from the initial pile (projected distance, without considering slope). Their profiles are similar to point L_2 in Fig. 6b. The height profile is bell-shaped, starting from zero and then waning back to zero in ~ 20 s. All the dynamics occurs

during the first minute. Plot (b) shows transitional features, and focuses on points at the boundary of the initial pile. In plots 15f,g,h,i,j, points are set where the slope reduces, and the flow can channelize and leave a deposit. Projected distance from the initial pile is $\sim 2 - 3$ km. The profiles are sometimes similar to L_3 of Fig.6c, other times to L_4 of Fig.6d, in a few cases showing intermediate aspects. In general is either observed an initial short-lasting bulge followed by a slow decrease lasting minutes and asymptotically tending to a positive height, or a steady increase of material height tending to a positive height. In both cases it is sometimes observed a bimodal profile in the first 5 minutes. Finally, plots 15k,l focus on three points set at about the runout distance of the flow, in the most important ravines, at $\sim 4 - 5$ km projected distance from the initial pile. Profiles are similar to what observed in point L_4 of Fig.6d.

5.1.2 Average flow Speed, local measurements.

Figure 16 shows the flow speed, $h(L, t)$, at the 51 spatial locations of interest, according to MC.

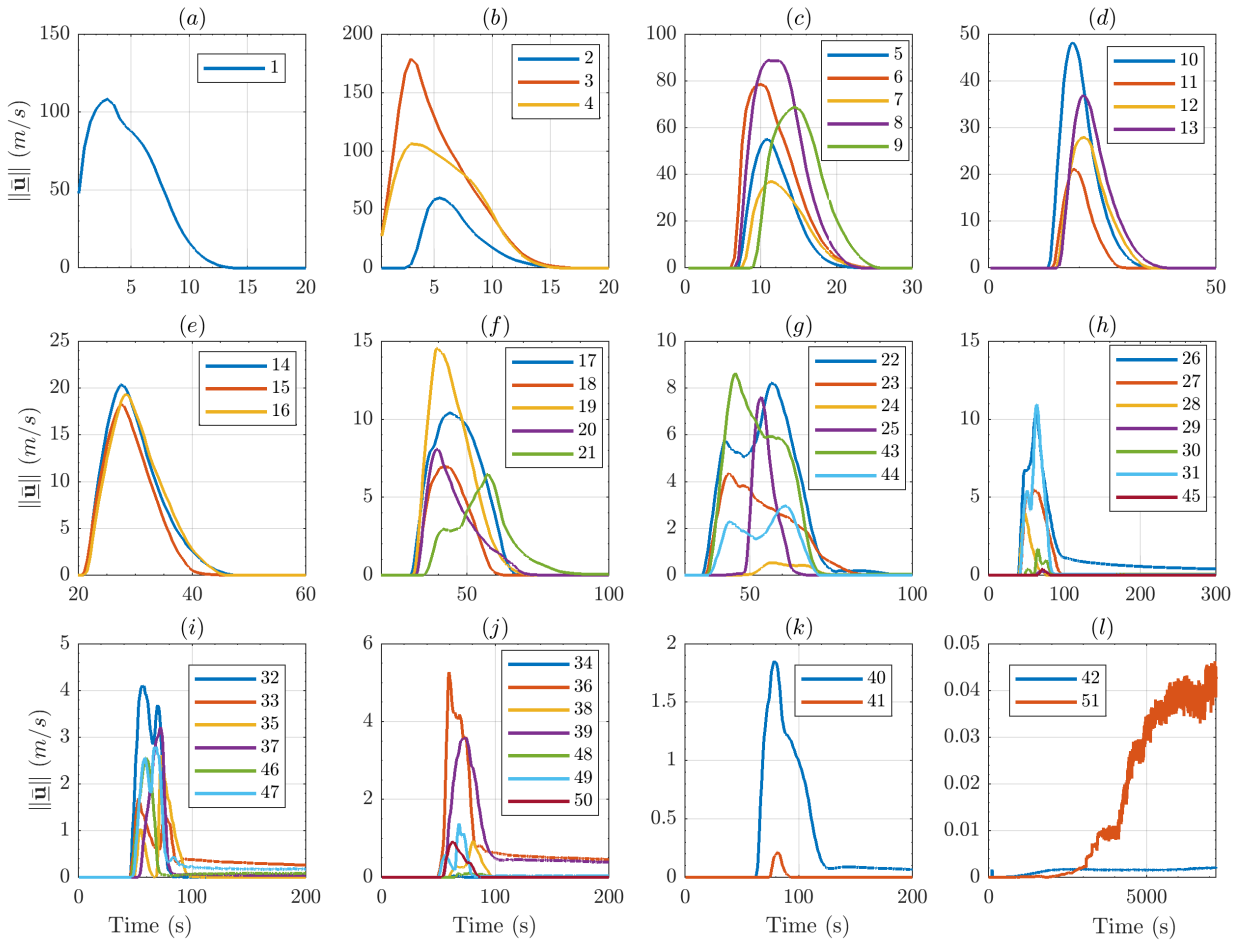


Figure 16: MC model, records of average flow speed, $|\underline{u}|(L, t)$, in 51 spatial locations of interest (Fig. 3).

Again the different plots have different scales on either time and space axes. The plot profiles are similar to what observed in figure 7, following the plot profile classification described above. Maximum speed of $\sim 200\text{m/s}$ is observed in proximity of the initial pile, in plot 16b, and it is related to the initiation collapse dynamics. After 1 km runout (horizontal projection), in plot 16e, the max speed is ten times smaller, $\sim 20\text{m/s}$. At about 2 km from the initiation, when entering the main ravines, speed

is $\sim 10m/s$, and becomes $\sim 5m/s$ or less in the distal part of the ravines. In detail, in plots 16f,g,h,i,j, the speed often shows bimodal profiles, not observed in the inclined plane case study. Moreover, in plots 16h,i,j, positive asymptotes are sometimes observed, meaning a slowly and steadily moving material even minutes after the collapse.

5.1.3 Average Froude Number, local measurements.

Figure 17 shows the Froude Number, $\|\bar{\mathbf{u}}\|/\sqrt{gh}$, at the 51 spatial locations of interest, according to MC.

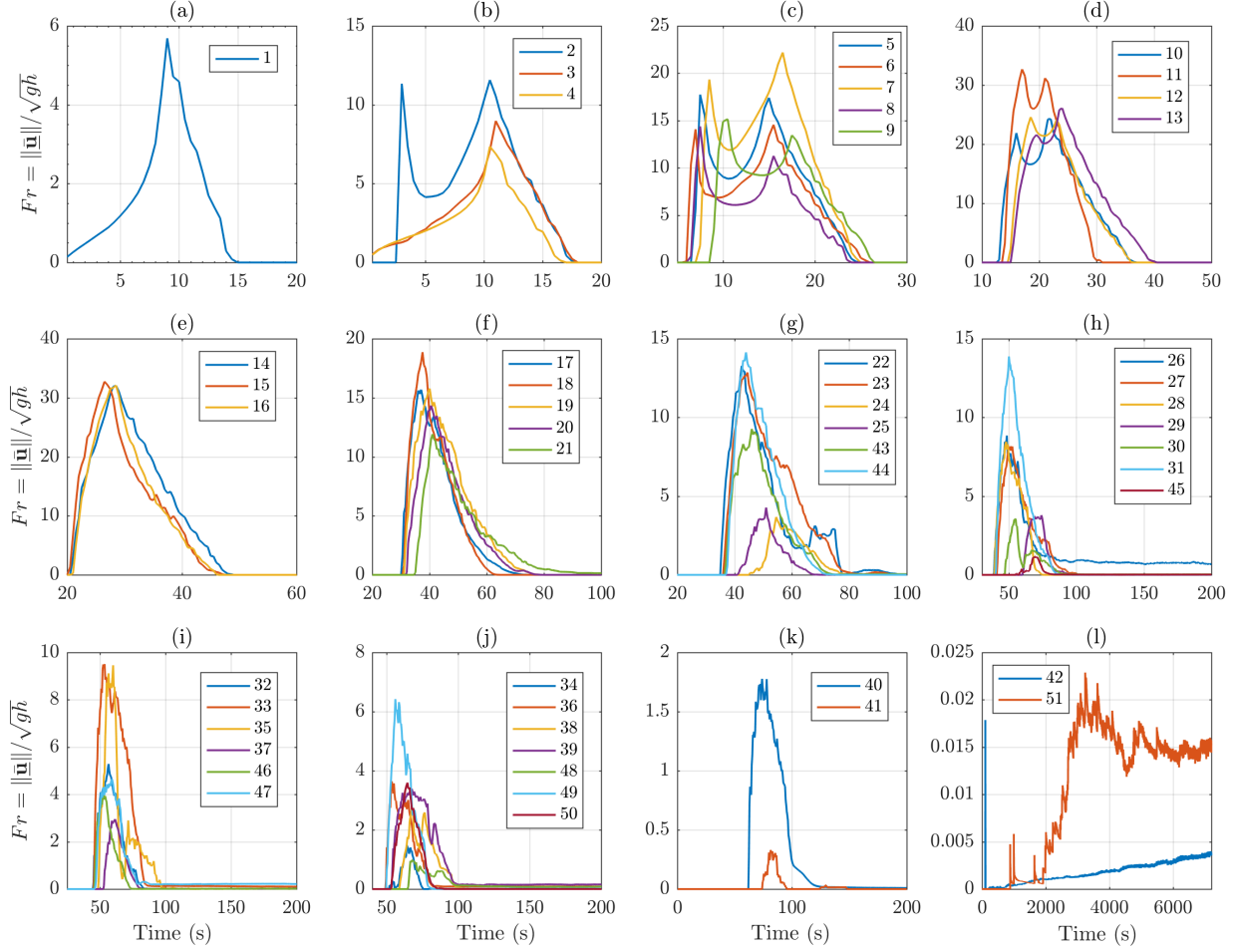


Figure 17: MC model, records of average Froude Number in 51 spatial locations of interest (Fig. 3).

Froude Number combines height and speed measurements, and plot profiles are similar to what observed in Figure 8. In particular, in plots 17b,c,d, strongly bimodal profile are observed due to the interplay between flow height and flow speed. In plots 17f,g,h,i,j, sharp changes are observed, and the plots are significantly rough when the speed is significantly small.

5.2 Observable outputs - six selected locations

The six selected locations are $[L_8, L_{10}, L_{17}, L_{39}, L_{43}, L_{46}]$, (see Fig. 3). First two points, L_8 and L_{10} are both significantly close to the initiation pile, the points L_{17} and L_{43} are placed where the slope is reducing and the ravine channels start, and L_{39} and L_{46} are placed in the channels, further down-slope. Moreover, L_8 , L_{43} , and L_{46} are placed at the western side of the inundated area, whereas L_{10} , L_{17} , and L_{39} are placed at the eastern side.

5.2.1 Flow Height, selected measurements

Figure 18 shows the flow height, $h(L, t)$, at the points $(L_i)_{i=8,10,17,39,43,46}$, for the three rheology models.

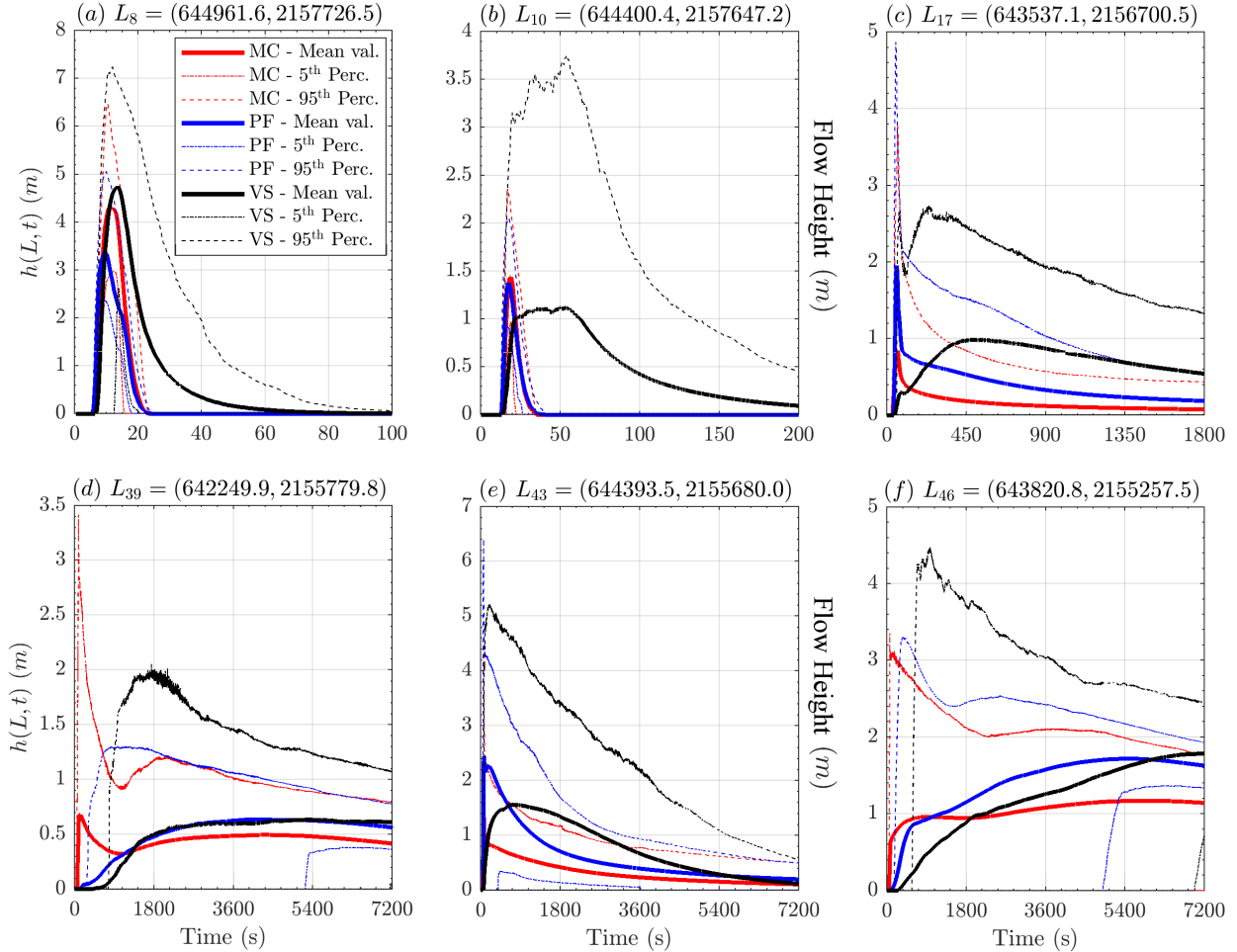


Figure 18: Records of flow height at six selected locations. Bold line is mean value, dashed/dotted lines are 5th and 95th percentile bounds. Different rheology models are displayed with different colors. Plots are at different scale, for simplifying lecture.

In plots 18a,b, we show the flow height in points L_8 and L_{10} , $\sim 200m$ and $\sim 500m$ from the initial pile, respectively. L_8 is on the east side, and L_{10} on the west side of the flow. Models MC and PF have similar profiles, lasting less $\sim 15s$ and bell-shaped. VS requires a significantly longer time to decrease, particularly in point L_{10} , where the average flow height is still positive after $\sim 200s$. Peak average values in L_8 are 3.4m for PF, 4.3m for MC, 4.7m for VS, with uncertainty of $\sim \pm 2m$, halved on the lower side for MC, and PF. In L_{10} , models MC and PF are almost indistinguishable, with peak height at 1.4m

and uncertainty $\pm 0.5m$. Model VS, in contrast, has a maximum height of $1.1m$ lasting for $50s$, and 95^{th} percentile reaching $3.7m$. In plots 18c,e, we show the flow height in points L_{17} and L_{43} , both at $\sim 2km$ from the initial pile, on the west and east side of the flow, respectively. All the three models show in both the points a fast spike in the first minute, followed by a slow decrease, still showing a positive average height after $30m$. Again, VS is significantly different from MC and PF, and has a secondary rise peaking at $\sim 450s$, which is not observed in the other models. This produces higher values for the most of the temporal duration, but converges to similar deposit thickness after more than 1 hour. Maximum values are $1m$ for MC, $2m$ for PF, and $1.5m$ for VS, in both locations. The 5^{th} percentile is zero for all the three models, meaning that the parameter range does not always allow the flow to reach those locations. The 95^{th} percentile is above $5m$ for the models, except in VS, point L_{17} . In plots 18d,f, we show the flow height in points L_{39} and L_{46} , both at more than $3km$ from the initial pile, on the west and east side of the flow, respectively. The three models all show an increasing profile, except for MC in point L_{39} which has an initial spike and a decrease before to rise again. A similar decreasing profile can be also observed in the 95^{th} percentiles of all the models. It is significant that the 5^{th} percentile of PF becomes positive after $\sim 5400s$, meaning that the flows almost surely have reached that location. Deposit thickness is $\sim 0.5m$ for all the models in point L_{39} , and $1.7m$ for VS, $1.6m$ for PF, $1.2m$ for MC, in L_{46} .

5.2.2 Flow Speed, selected measurements

Figure 19 shows the flow speed, $\|\mathbf{u}\|(L, t)$, at the points $(L_i)_{i=8,10,17,39,43,46}$, for the three rheology models. Like observed in Fig.18, pair of points L_8 and L_{10} , points L_{17} and L_{43} , and points L_{39} and L_{46} have significantly similar plot profiles. In plot 19a MC shows higher average speed, $\sim 80m/s$, than PF and VS, both $\sim 70m/s$. 95^{th} percentile values can reach $150m/s$ in MC, $140m/s$ in VS, $130m/s$ in PF. MC and PF are null after $20s$, while VS decreases slower, and becomes null at $\sim 60s$. In plot 19b, the average peak values are $\sim 40m/s$ in MC and PF, while only $20m/s$ in VS. All the three models show 95^{th} percentile values above $60m/s$. VS speed decreases remarkably slower than in the other models, requiring more than $120s$ to become null, while MC and PF speed remains positive for $\sim 25s$. In plot 19c, average speed is $\sim 20m/s$ in PF, $\sim 10m/s$ in MC, $\sim 2m/s$ in VS. 95^{th} percentile values can reach $\sim 55m/s$ in PF, $\sim 48m/s$ in MC, $\sim 24m/s$ in VS. The duration of positive velocity in VS can be long hundredths of seconds. A very similar situation is pictured in plot 19e. Instead in plot 19d, only MC shows a max speed above $3m/s$, the 95^{th} percentile values at $\sim 15m/s$. In the other models the average speed is always below $1m/s$ and the 95^{th} percentile values have an increasing profile followed by a slightly decreasing plateau, at $\sim 2m/s$ in VS, $\sim 1m/s$ in PF. VS can have a speed above $\sim 1m/s$ at $\sim 3600s$. In plot 19f, only MC shows an average speed above zero, while in the other models even the 95^{th} percentile values are always below $\sim 0.5m/s$, and start to be positive only at $\sim 200s$ in PF, and $\sim 600s$ in VS. MC can have speed at $\sim 1m/s$ for more than $\sim 500s$, but the plot is very noisy.

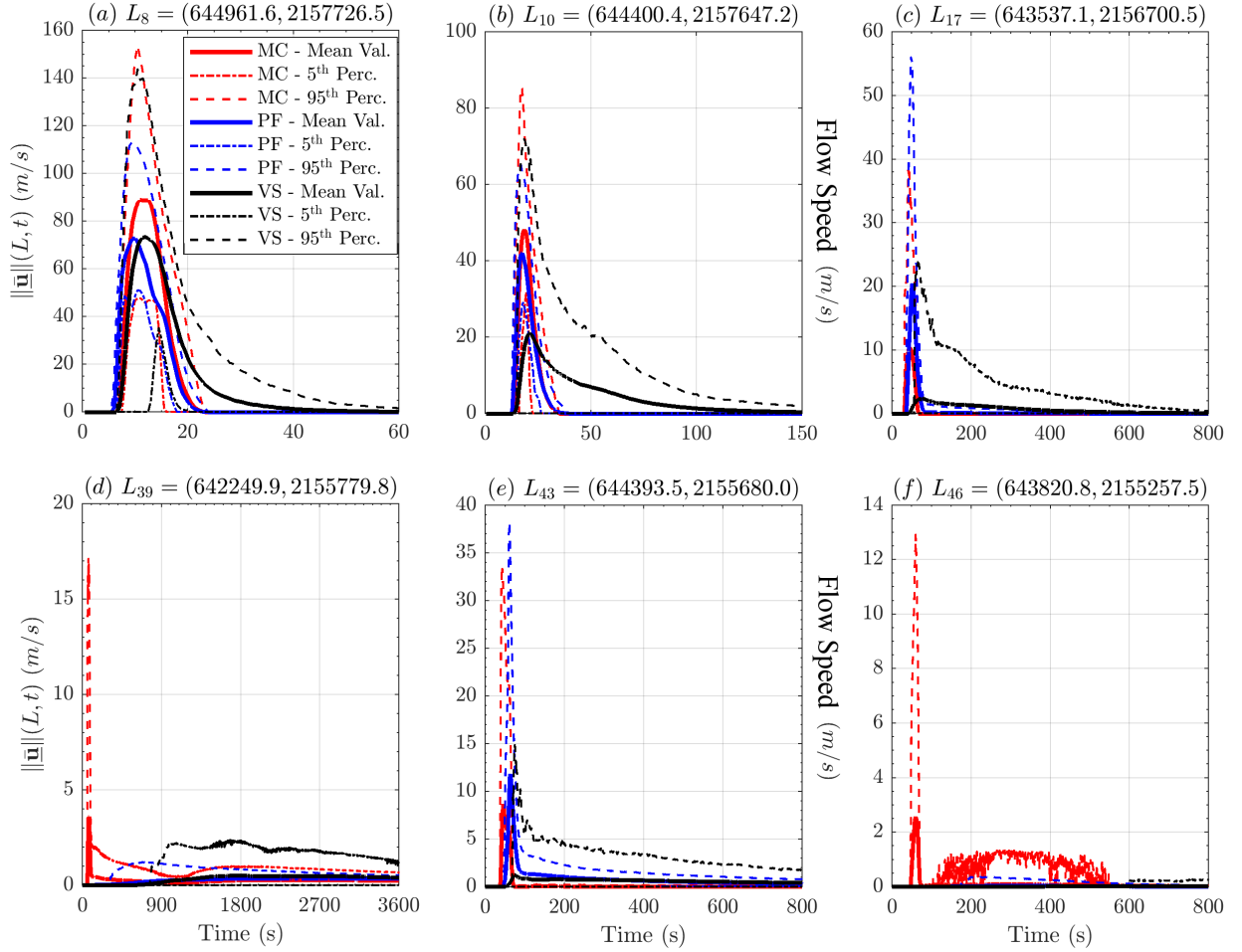


Figure 19: Records of flow speed at six selected locations. Bold line is mean value, dashed/dotted lines are 5th and 95th percentile bounds. Different rheology models are displayed with different colors. Plots are at different scale.

5.2.3 Froude Number, selected measurements

Figure 20 shows the Froude Number, $\|\bar{\mathbf{u}}\|/\sqrt{gh}$, at the points $(L_i)_{i=8,10,17,39,43,46}$, for the three rheology models.

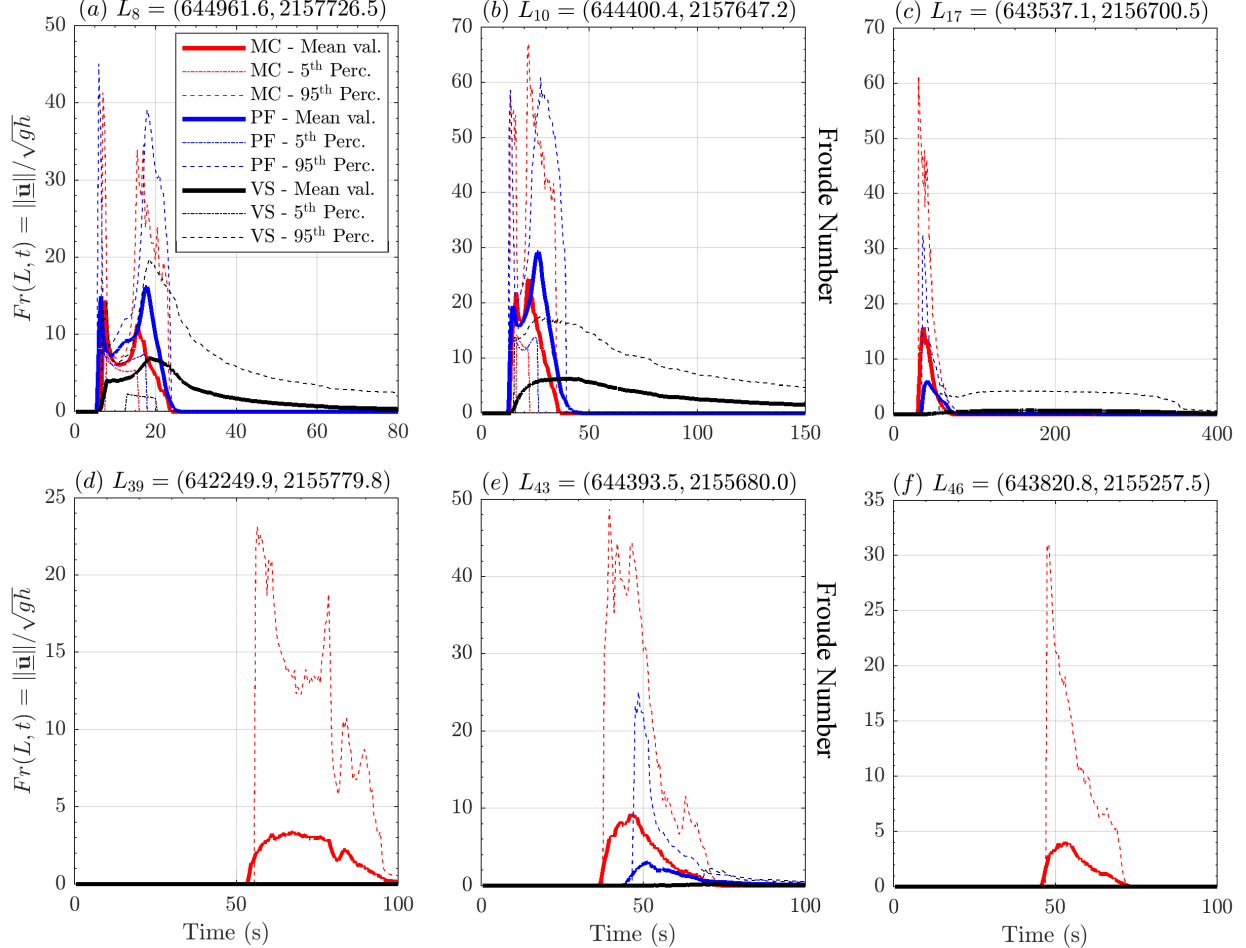


Figure 20: Records of Froude number at six selected locations. Records of points L_{39} , L_{43} , and L_{46} are displayed at two different scales, according to the initial dynamics, in plots (d-f), and the asymptotic dynamics, in plots (g-i). Bold line is mean value, dashed/dotted lines are 5th and 95th percentile bounds. Different rheology models are displayed with different colors.

Froude Number is proportional on the ratio between the flow speed and the square root of flow height, and hence the observed plots profiles are the combine effects of Fig. 18 and 19. Largest values are observed when the speed is significantly high compared to the flow height. Similarly to what observed in Fig. 8 and 17, in plots 20a,b bimodal profiles are displayed. The first peak when the flow arrives in the location, the second when it leaves the location. Due to the slower dynamics of VS, the bimodal profile is almost absent. In PF the peaks, at ~ 15 and ~ 30 , respectively, are slightly more prominent than in MC. In contrast, in plot 20c, MC displays an average Fr of ~ 15 significantly larger than in PF, ~ 5 , and VS is almost null. In plot 20e the profile is significantly similar, but with lower values. In plots 20d,f, only MC displays a significantly positive Fr, the average below 5, but the 95th percentile can reach above 20. Finally, in plots 20g,h,i, a zoom on the low Fr values in the distal locations is displayed on a long time window. Observations are sometimes noisy, and only 20g shows the 95th percentile above 1. The rest of the plots are significantly lower. In general, PF has a more decreasing and less noisy character than MC

and VS, while the latter is the most noisy and also has a weakly increasing profile.

5.2.4 Flow Acceleration, selected measurements

Figure 21 shows the flow speed, $\|\mathbf{a}\|(L, t)$, at the points $(L_i)_{i=8,10,17,39,43,46}$, for the three rheology models.

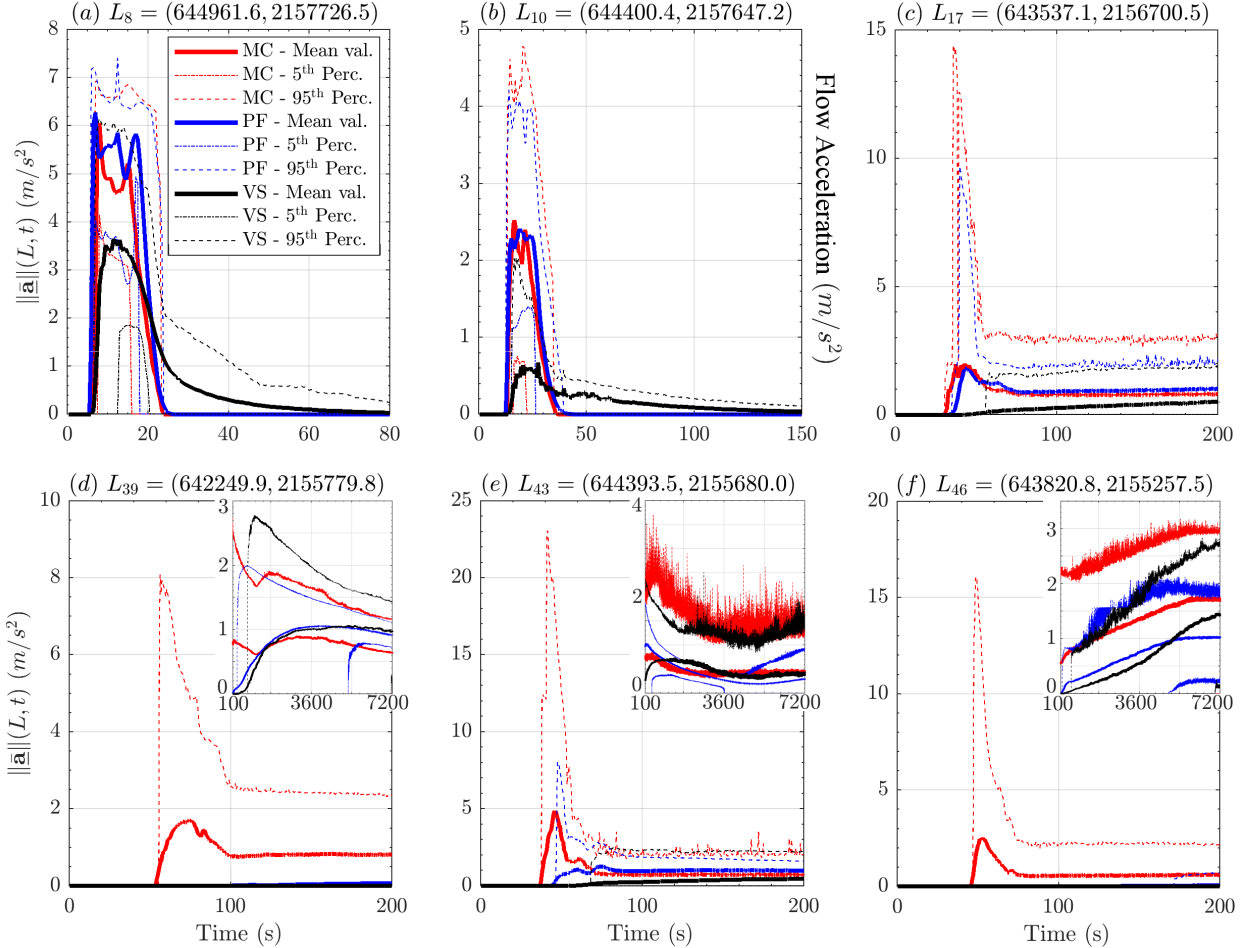


Figure 21: Records of flow acceleration magnitude (computed from LHS), in six selected locations. Records of points L_{39} , L_{43} , and L_{46} are displayed at two different scales, according to the initial dynamics, in plots (d-f), and the asymptotic dynamics, in plots (g-i). Bold line is mean value, dashed lines are 5th and 95th percentile bounds. Different rheology models are displayed with different colors.

In plot 21a,b, MC and PF display a higher maximum acceleration, both at $\sim 6m/s^2$ and $\sim 2.5m/s^2$ in the first and second plot respectively, than VS, $\sim 3.5m/s^2$ and $\sim 0.5m/s^2$, respectively. The latter has a slower decrease to zero, consistent with what observed on the speed and Froude. Uncertainty in VS is more significant in plot 21a, than in plot 21. It is the opposite in MC and PF. In plot 21c, in MC and PF there can a significant peak in acceleration, up to $\sim 15m/s^2$ and $\sim 10m/s^2$, in the 95th percentile values, respectively. The same peak is absent in the average plots, which are significantly flat in all the models, with values at $\sim 1m/s^2$ in MC and PF, and $\sim 0.5m/s^2$ in VS, at $\sim 200s$. Plot 21e is similar, but PF is significantly reduced and lack of the peak in the 95th percentile values. In plot 21d,f, only MC shows significant acceleration values. Like in Fig.20, plots 21g,h,i, are a zoom on the acceleration values in the distal locations, displayed on a long time window of 7200s. The last two plots are more noisy and

possess an increasing trend. All the three show, in all the models, values up to $\sim 1m/s^2$. In general, PF acceleration tends to be lower than in the other models.

5.2.5 Flow area and spatially averaged measurements

Figure 22 shows the spatial average of speed and Froude Number, for the three rheology models. Moreover, it shows the inundated area of flow, as a function of time.

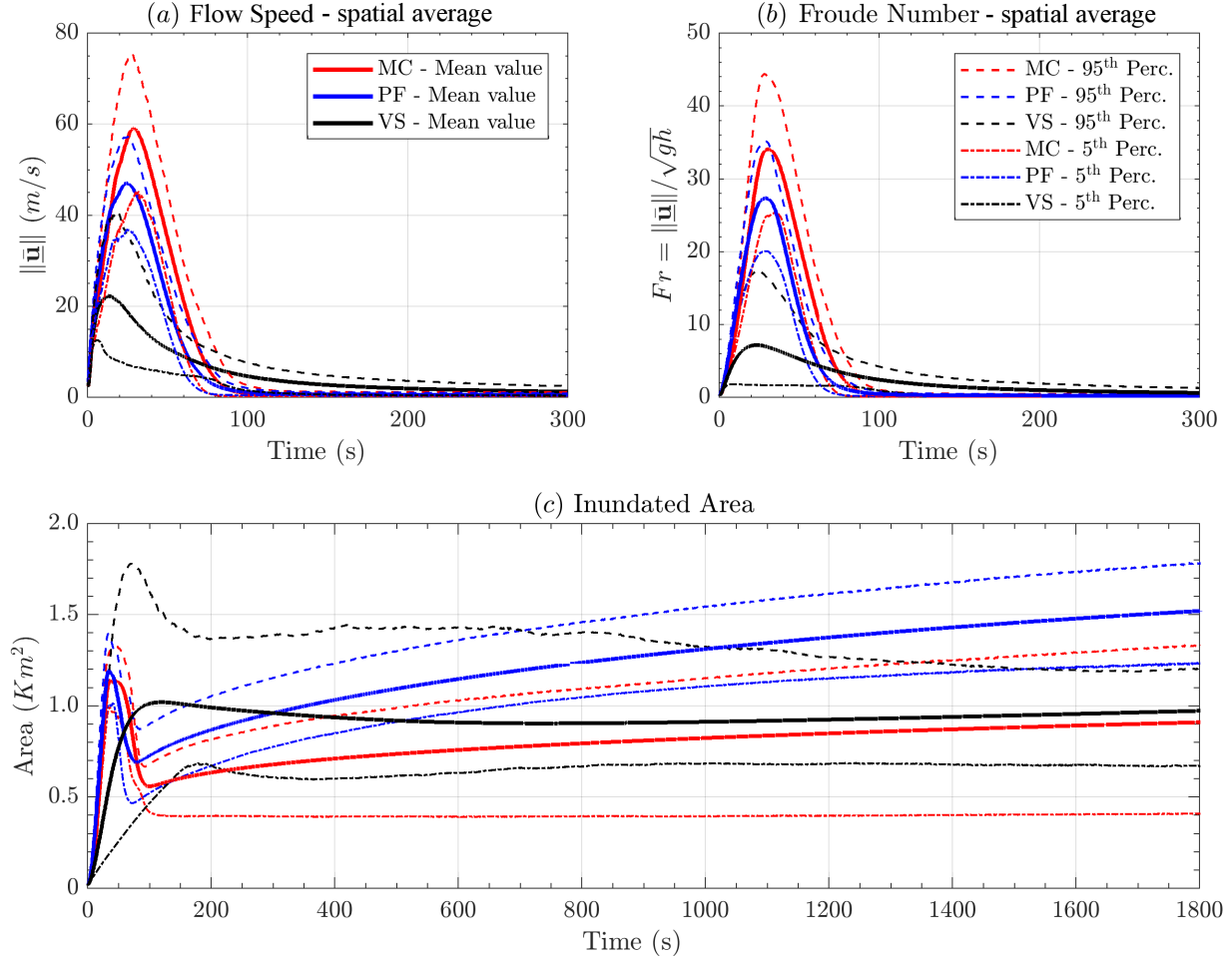


Figure 22: Comparison between spatial averages of (a) flow speed, and (b) Froude Number, in addition to the (c) inundated area, as a function of time.

Like in Fig.10, spatial averages and inundated area have smoother plots than local measurements, and most of the details observed in local measurements are not easy to discern. In plot 22a the speed shows a bell-shaped profile in all the models, but whereas the values were significantly similar in the inclined plane experiment, here the maximum speed is $\sim 60m/s$ in MC, $\sim 50m/s$ in PF, $\sim 20m/s$ in VS, on average. Uncertainty is $\pm 18m/s$ in MC, similar, but skewed on the larger values in VS, $\pm 10m/s$ in PF. In plot 22b, the Froude profile is very similar to the speed, but the difference between Vs and the other models is accentuated. Maximum values are ~ 50 in MC, ~ 38 in PF, ~ 5 in VS, whereas uncertainty is ± 10 in MC, ± 7 in PF, and skewed $[-5, +10]$ in VS. In plot 22c, inundated area has a first peak in MC and PF, both at $\sim 1.15km^2$, followed by a decrease to $0.55km^2$ and $0.7km^2$, respectively, and then a slower increase up to a flat plateau at $0.9km^2$ and $1.5km^2$, respectively. Uncertainty is $\sim \pm 0.2km^2$ in both MC and PF until $\sim 100s$, and then they increase at $\pm 0.3km^2$ and $[-0.5, +0.4]km^2$, respectively.

In MC the increase on uncertainty is particularly significant at ~ 100 s, while it is more gradual in PF. VS has a different profile. The initial peak is significant only in the 95th percentile values, and occurs significantly later, i.e. at ~ 100 s against ~ 50 s in MC and PF. It is of $\sim 1\text{km}^2$ on the average, but up to $\sim 1.8\text{km}^2$ in the 95th percentile. The decrease after the peak is very slow and the average inundated area is never below 0.85km^2 , and eventually reaches back to $\sim 1\text{km}^2$. Uncertainty is $[-0.3, +0.2]\text{km}^2$.

5.3 Statistical analysis of dynamic quantities

The current case study does not show a preferential direction, equivalent to the slope direction of the inclined plane. Hence, we will focus on the moduli, and powers, of the force terms detailed in Section 4.2. In particular, all the estimates assume the material density of the flow $\rho = 1800\text{kg/m}^3$. This a fixed scaling factor, and the plots aspect is not affected by its value.

5.3.1 Forces, spatial integral

Figure 23 shows the spatial sum of the force terms moduli, for the three rheology models.

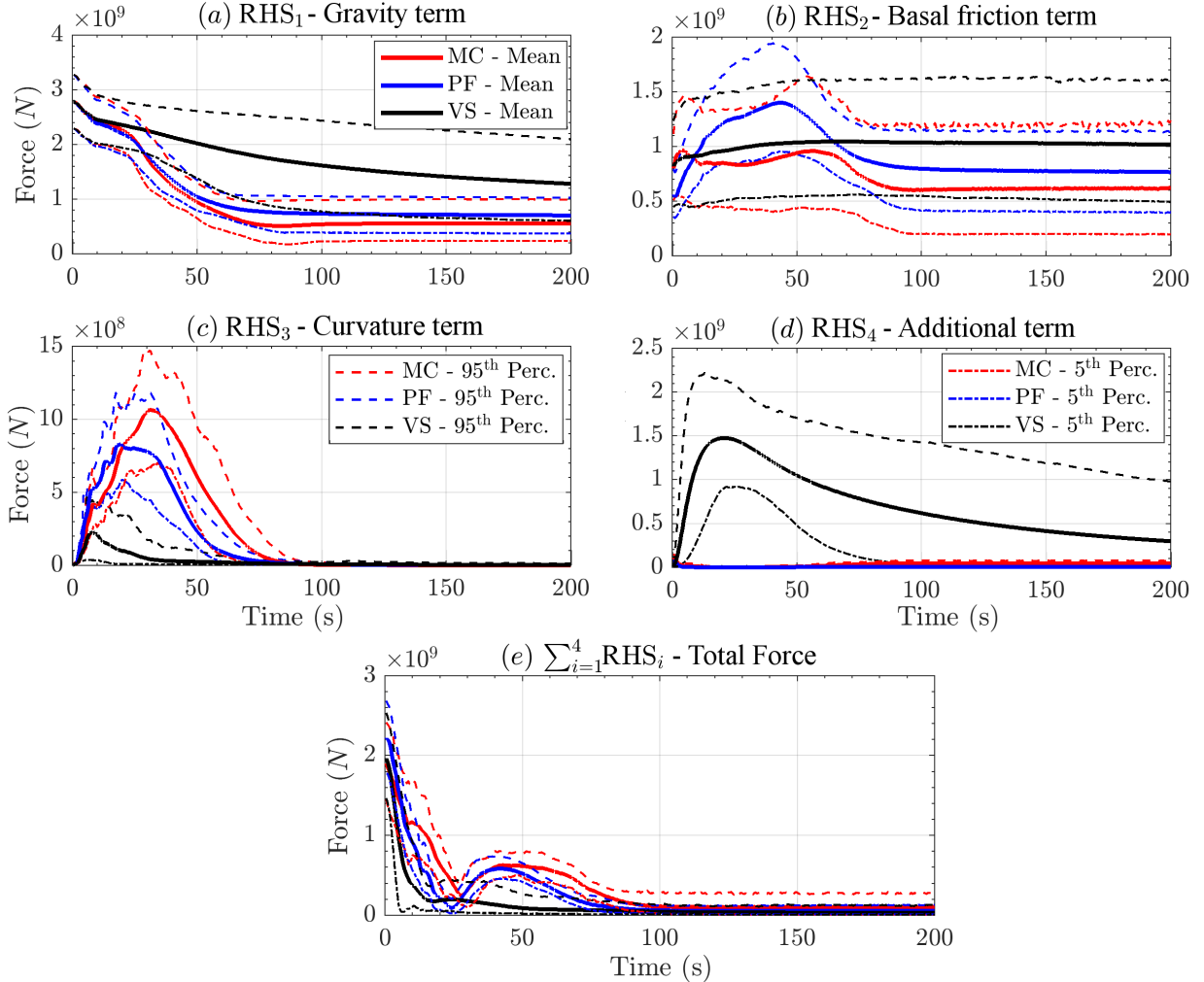


Figure 23: Spatial sum of the RHS force terms moduli. Bold line is mean value, dashed lines are 5th and 95th percentile bounds.

The figure can be compared with Fig. 11, which was related to forces in the slope direction in the inclined plane case study. In plot 23a \mathbf{RHS}_1 represents the effect of the gravity in all the models. It is decreasing in all the models, but more gradually in VS than in the others. Initial values are $2.8e9N$ in all the models, uncertainty $\pm 2.5e8N$. Force values are consistent with the material weight component along the mountain slope, and their decrease is related to the slope reduction. At $\sim 10s$ all the models show a slowing down of the decrease, which is permanent in VS, and lasting $10s$ in MC and PF. The latter models, reach a flat profile after $\sim 60s$, at $6e8N$ and $7e8N$, respectively, and uncertainty of $\pm 2e8N$ and $1.5e8N$. VS, which flattens more gradually, is $1.3e9N$ at $200s$, uncertainty $[-7e8, +8e8]N$. In plot 23b \mathbf{RHS}_2 represents the effect of the basal friction in all the models. In MC, shows a bimodal profile, with a peak at $5s$, and a second one at $60s$. Both of them at $9.5e8N$ on average, with uncertainty of $[-4e8, +5e8]N$ in the first peak, and $[-5e8, +7e8]N$ in the second. The minimum between the two peaks is at $8e8N$ and lasts from $10s$ to $30s$. After the second peak there is significant decrease, reaching $6e8N$ at $90s$, and becoming flat. Final uncertainty is $[-4e8, +6e8]N$. In PF, the plot starts from lower initial values than in the other models, but then has a unimodal peak of $1.4e9N$ at $40s$, on average. Uncertainty $\pm 5e8N$. After that, the plot decreases, reaching $7.5e8N$ at $90s$, and becoming flat. Final uncertainty is $\pm 3.5e8NN$, lower than in the other models. In VS, there is slow increase until the plot reaches $1.05e9N$ at $70s$. Then the average force is almost flat, at $1.0e9N$, with significant uncertainty of $[-5e8, +6e8]N$. In plot 23c \mathbf{RHS}_3 represents the effect of the curvature of terrain. The three models all show a bell-shaped profile, waning to zero at $90s$. However, MC has reaches $1.1e9N$ at $30s$, PF $8e8N$ at $20s$, VS $2.5e8N$ at $10s$. The rise has a similar profile, but a different duration. The decrease is more gradual in VS. Uncertainty at the peak value is $\pm 4.5e8N$ in MC, $[-2.5e8, +3.5e8]N$ in PF, $\pm 2e8N$ in VS. In plot 23d \mathbf{RHS}_4 has a different meaning in the three models. In MC it is the internal friction term, and it has a small peak in the first second, at $1e8N$. After that it flattens to negligible values, but shows again values at $5e7N$ after $60s$. In PF it is the a depth averaged correction in the hydrostatic pressure, and has a almost negligible effect only in the first second, at $5e7N$. In VS, instead, it is the velocity dependent term, and has a very relevant effect. The plot shows a bell-shaped profile, with a peak of $1.45e9N$ at $20s$. Uncertainty is $[-5.5e8, +6.6e8]N$, at the peak. After that, the force gradually decreases, and is $3e8N$ at $200s$, on average. Uncertainty $[-3e8, +7e8]N$. In plot 23d, the modulus of the total force $\sum_{i=1}^4 \mathbf{RHS}_i$ is shown, with the complex interplay between the terms. First a steep decrease due to the domination of the gravity upon the friction, then a bell-shaped increase when the friction stops the dynamics.

5.3.2 Powers, spatial integral

Figure 24 shows the spatial sum of the powers, for the three rheology models.

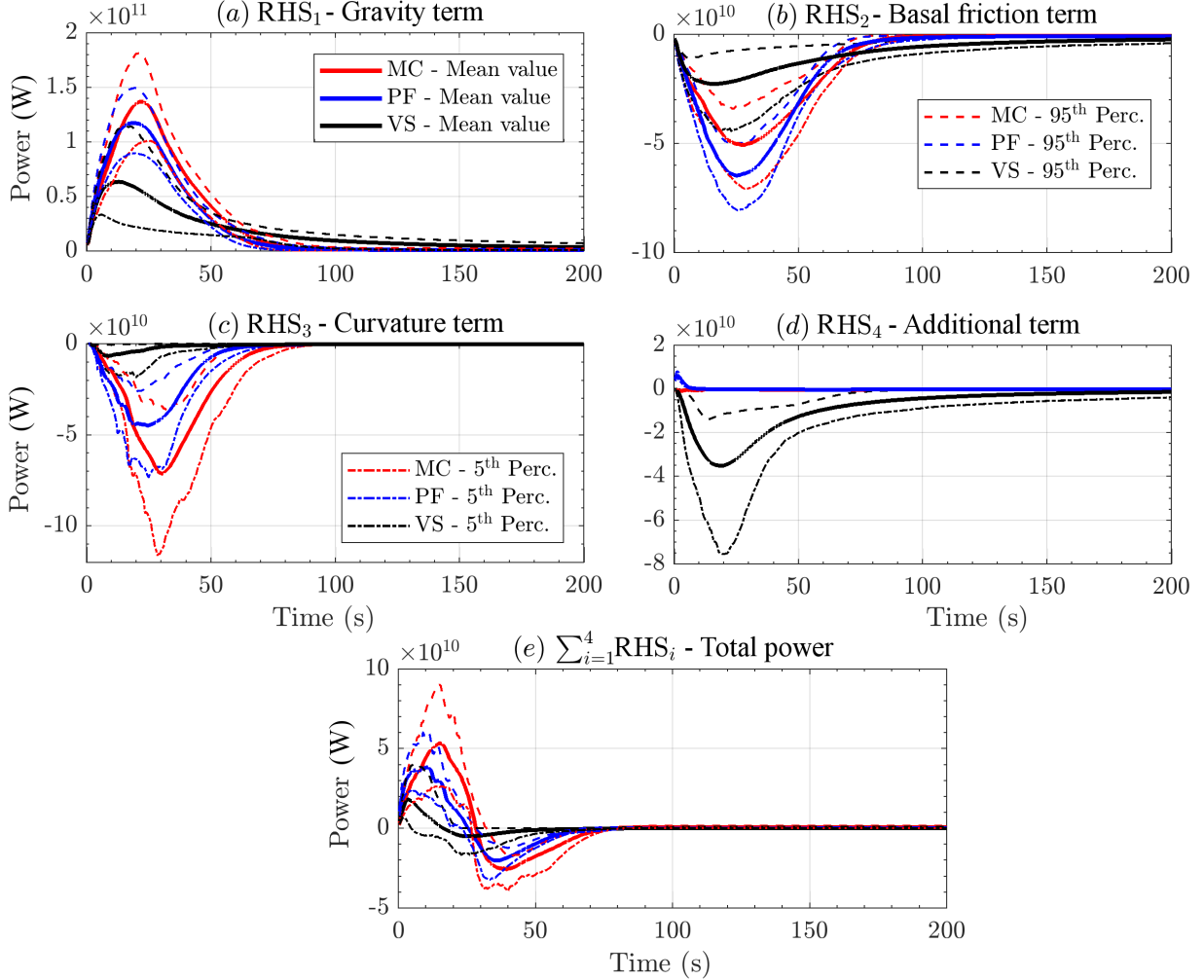


Figure 24: Spatial sum of the RHS powers. Bold line is mean value, dashed lines are 5th and 95th percentile bounds. Model comparison on the mean value is also displayed.

The plots follow the same order used in Fig. 23, but the scalar product with velocity imposes the bell-shaped profile already observed in Fig. 12a. In plot 24a the power of RHS_1 starts from zero and rises up to $\sim 1.4e11\text{W}$ in MC, $\sim 1.2e11\text{W}$ in PF, $\sim 6.5e10\text{W}$ in VS. Uncertainty is $\pm 4e10\text{W}$ in MC, $\pm 3e10\text{W}$ in PF, $[-4e10, +5e10]\text{W}$ in VS. In plot 24b the power of RHS_2 is negative and peaks to $\sim -6.5e10\text{W}$ in MC, $\sim -5e10\text{W}$ in PF, $\sim -2e10\text{W}$ in VS. Again VS power is significantly lower than in the other models. Uncertainty is $\pm 2e10\text{W}$ in MC, $\pm 1.5e10\text{W}$ in PF, $[-2e10, +1e10]\text{W}$ in VS. In plot 24c the power of RHS_3 has a similar profile to the force, peaking to $\sim -7e10\text{W}$ in MC, $\sim -4.5e10\text{W}$ in PF, $\sim 5e9\text{W}$ in VS. Uncertainty is $[-4.5e10, +3.5e10]\text{W}$ in MC, $[-2.5e10, +2e10]\text{W}$ in PF, $[-1e10, +5e9]\text{W}$ in VS. In plot 24d the power of RHS_4 is relevant only in VS, although also in PF has a very short lasting positive peak up to $5e9\text{W}$ before to become null at $\sim 10\text{s}$. Peak negative power in VS is $\sim -3.5e10\text{W}$, $[-2e10, +1e10]\text{W}$. In plot 24e the power of the total force $\sum_{i=1}^4 \text{RHS}_i$ summarizes the energy accumulation and dissipation, following, like in the inclined plane case study, a sinusoid profile. As observed in Fig. 11e, MC profile is delayed compared to the others, and is affected

by a larger uncertainty.

5.3.3 Force contribution coefficients, RHS terms

Figure 25 shows the Contributions Coefficients (C_i) $_{i=1,\dots,4}$, for the three rheology models and focusing on the RHS terms moduli. The different models are plotted separately: 25a,d,g assume MC; 25b,e,h assume PF; 25c,f,i assume VS.

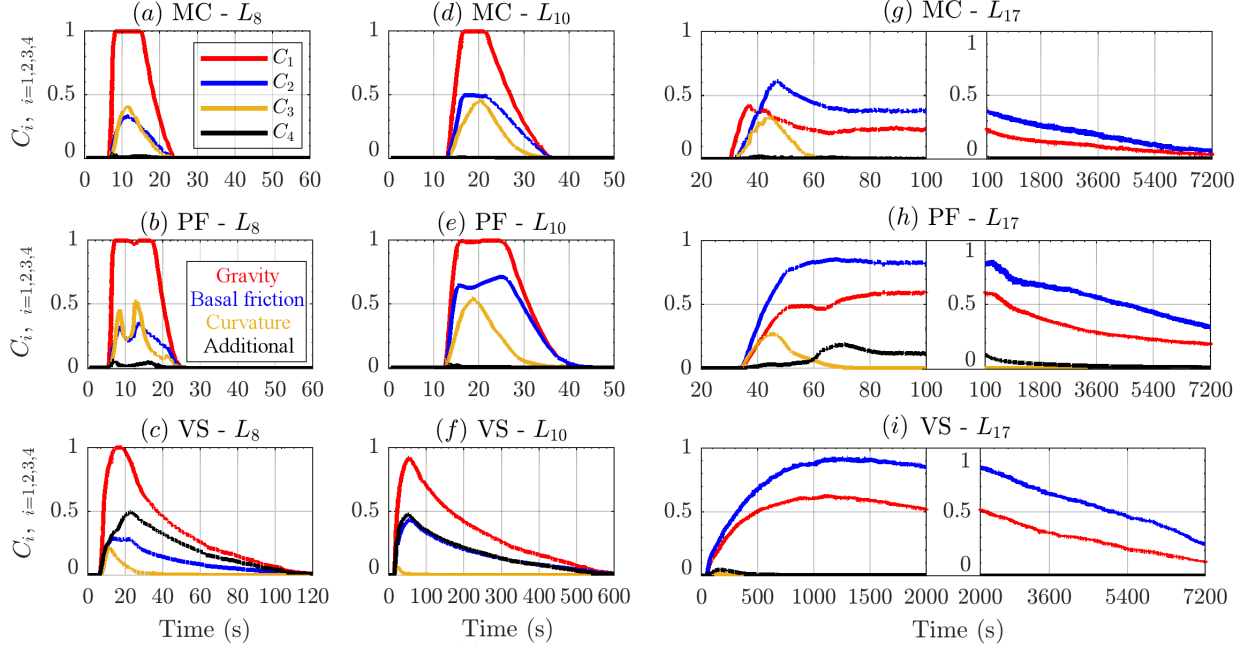


Figure 25: Records of contribution coefficients of **RHS** force moduli, at three spatial locations of interest, in the first km of runout. Different rheology models are displayed with different colors. Dominant factor is calculated based on the l^∞ norm (see Section 3.1)

The coefficients in the first two locations, points L_8 and L_{10} , are shown in 25a,b,c and 25d,e,f, respectively. Those points are close to the initial pile, in the western and eastern sectors of the inundated area. The pairs of plots related to the same model are similar. In all the models the greater contribution is given by C_1 , significantly larger than C_2 and C_3 , which have similar scales in MC and PF, while $C_2 > C_3$ in VS.. C_4 always gives a negligible contribution, except for in VS, where it is comparable with C_2 . In L_8 , following PF, C_3 is bimodal, whereas the plot is unimodal in MC and VS, or in L_{10} . In L_8 , C_3 is greater than in L_{10} , compared to the other forces. Like in the previous figures, VS shows a slower decrease of the plots, which is due to the rising probability of no-flow (see also next section). In plots 25g,h,i, are shown the coefficients in L_{17} , about 1 km from the initial pile (in horizontal projection). The plots are split in two sub-frames, following different temporal scales - the first 100s are on the left, and the rest of the temporal domain [100, 7200]s is on the right. Initial dynamics is dominated by C_2 , except for in MC, and only for a short time, [30, 35]s. In MC there is an initial peak of C_2 which is not observed in the other models. C_3 has a significant size, in MC and PF, and unimodal profile. In PF, after C_3 wanes, at about 60s, also C_4 , representing the effect of hydrostatic pressure correction, is not negligible, for ~ 40 s. The second part of the temporal domain, is characterized by a slow decrease of $C_2 > C_1$, due to the rise of the no-flow probability.

5.3.4 Force dominance factors, RHS terms

Figure 26 show the Dominance Factors (P_i) $_{i=1,\dots,4}$, for the three rheology models and focusing on the RHS terms moduli, at the three selected points L_8 , L_{10} , and L_{17} , closer than 1 km to the initial pile (in

horizontal projection).

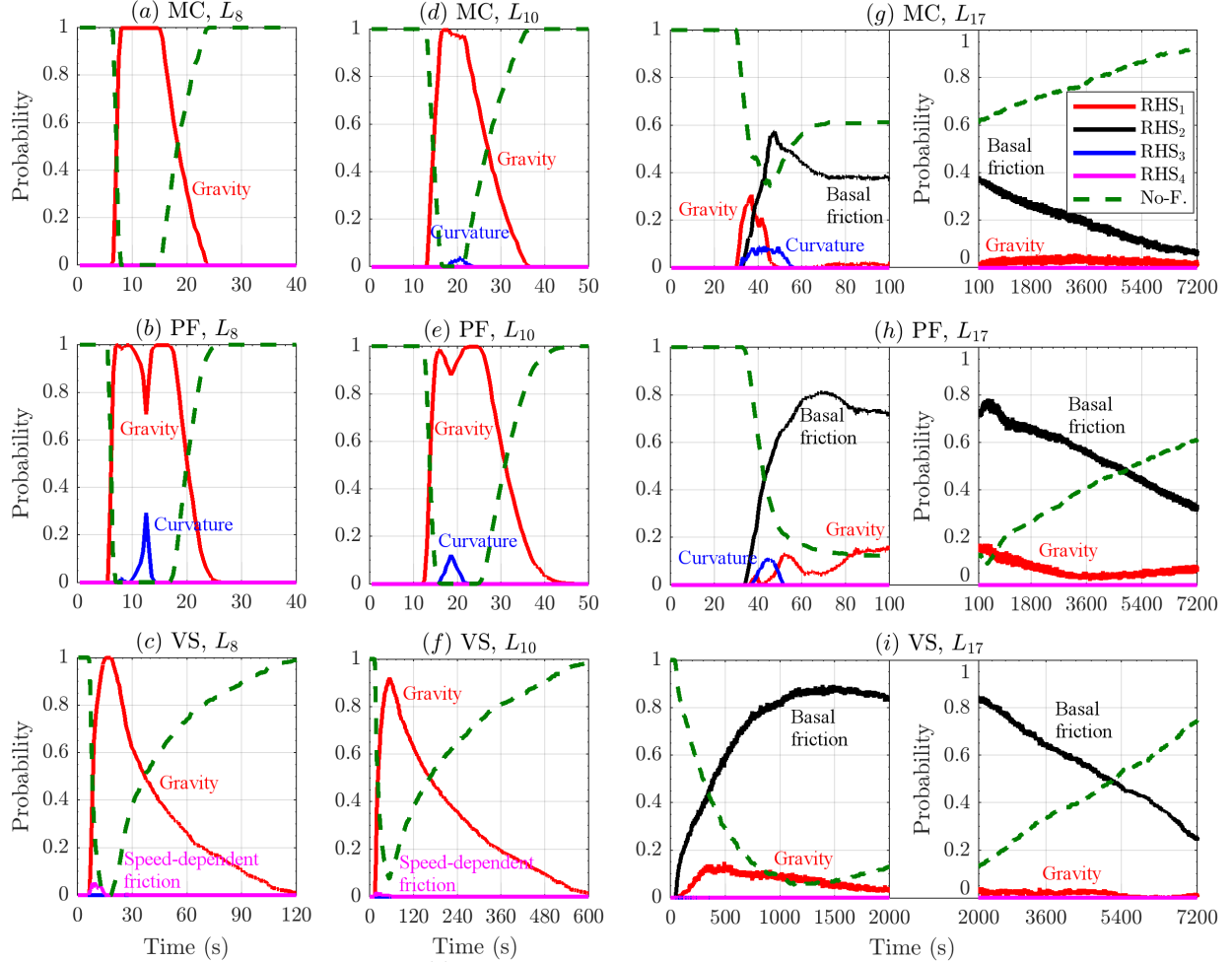


Figure 26: Records of dominance probabilities of **RHS** force moduli, at three spatial locations of interest, in the first km of runout. Bold line is mean value, dashed/dotted lines are 5th and 95th percentile bounds. Different rheology models are displayed with different colors. No-flow probability is also displayed.

The plots 26a,b,c and 26d,e,f are related to point L_8 and L_{10} , respectively. Like in the case of contribution coefficients, they are significantly similar. **RHS**₁ is the dominant force with a very high chance, $P_1 > 90\%$. In MC and PF it is observed a small chance, i.e. $P_3 = 5\% - 30\%$ at most, of **RHS**₃ being the dominant force for a short amount of time, i.e. $\sim 5s$. This occurs in the middle of the time interval in which the flow is almost surely inundating the points. In VS it is observed a $P_4 = 5\%$ chance of **RHS**₄ being dominant, for a few seconds, anticipating the minimum of no-flow probability. Plots 26g,h,i, are related to point L_{17} , and the plots are split in two sub-frames, following different temporal scales. In all the models, as observed in Fig.25, **RHS**₂ is the most probable dominant force, and its dominance factor has a bell-shaped profile, similar to the complementary of no-flow probability. In all the models, **RHS**₁ has a small chance of being the dominant force. In MC, this is more significant, at most $P_1 = 30\%$, for $\sim 20s$ after the flow arrival, and has again about $P_1 = 2\%$ chance to be dominant in $[100, 7200]s$. In PF, the chance is $P_1 = 15\%$ at most, and has two maxima, one short lasting at about $55s$, and the second in $[100, 500]s$. Also in VS, the chance is at most $P_1 = 15\%$, reached at $[300, 500]s$, but its profile is unimodal in time, and becomes lower than $P_1 = 2\%$ after $2000s$. In MC and PF, **RHS**₃ has a chance of $P_3 = 10\%$ of being the dominant force, for a short amount of time $[30, 50]s$ and $[40, 50]s$,

respectively.

Figure 27 show the Dominance Factors (P_i) $_{i=1,\dots,4}$, for the three rheology models, at the three selected points L_{39} , L_{43} , and L_{46} , over 2 km far away from the initial pile.

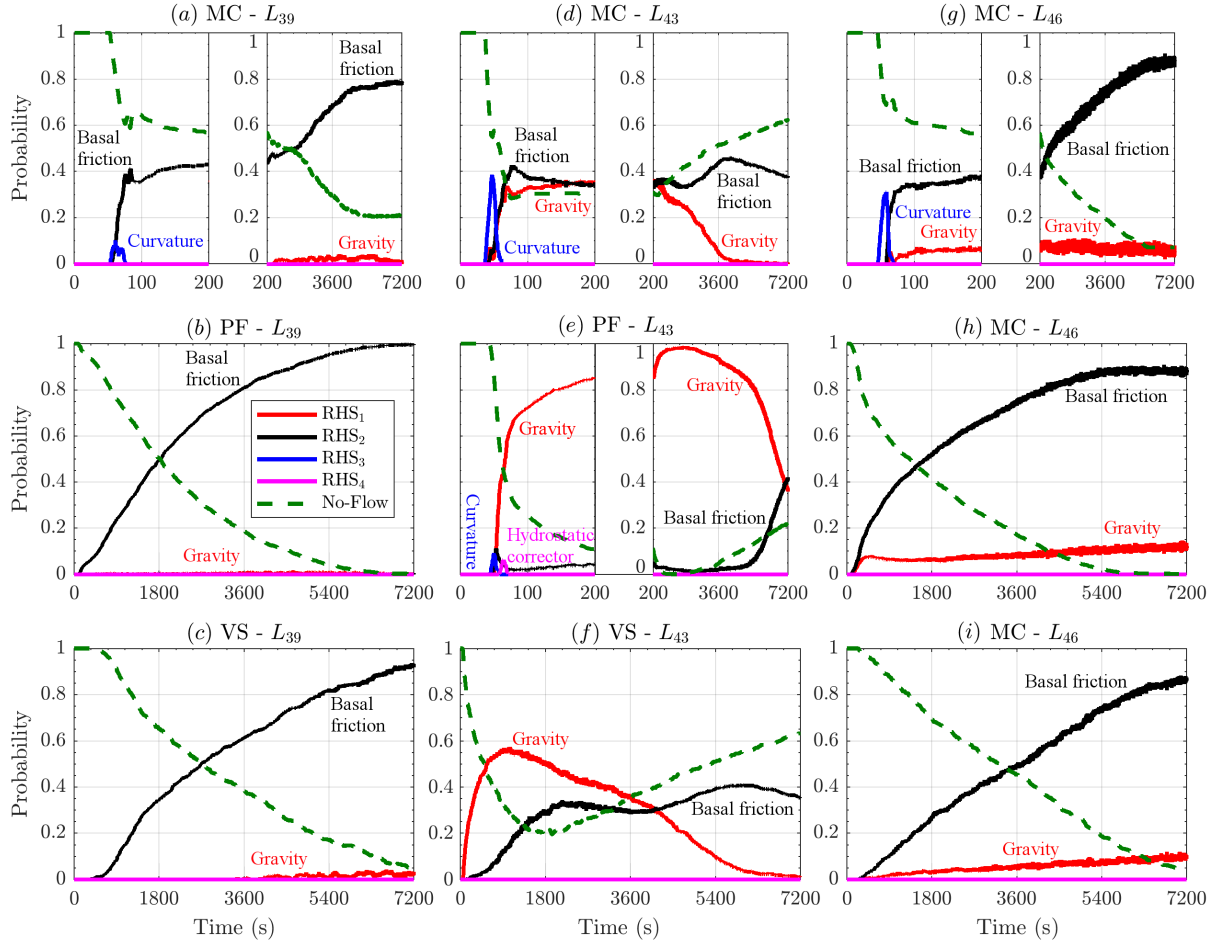


Figure 27: Records of dominance probabilities of **RHS** force moduli, at three spatial locations of interest, after 2 km of runout. Bold line is mean value, dashed/dotted lines are 5th and 95th percentile bounds. Different rheology models are displayed with different colors. No-flow probability is also displayed.

The plots 27a,b,c and 27g,h,i are related to point L_{39} and L_{46} , respectively, and they are significantly similar. Those points are both in the most distal part of the ravines, on the western and eastern side of the inundated area, respectively. They are also similar to the dominance factors at point L_{17} , shown in plots 26g,h,i, but the no-flow probability never wanes in this case, and the probability of **RHS₂** being the dominant force is $P_2 > 90\%$ till the end of the temporal window. Moreover, **RHS₁** does not show any initial peak in P_2 , and generally increases slowly, reaching at most $P_2 = 10\%$ chance of being the dominant force in L_{46} , after more than 3600s, in all the models. Plots 27d,e,f, are related to point L_{43} , are remarkably different. In MC, either **RHS₁** and **RHS₂** can be dominant forces, both with chances of $\sim 35\%$ in the first 200s. Then, **RHS₂** increases its chance, and becomes the only dominant force after 3600s. The no-flow probability is never below 30%. **RHS₃** has a chance P_3 up to 35% for a short amount of time, i.e. [40, 60]s. In PF, it is **RHS₁** to be the dominant force, with chance above $P_1 = 90\%$ until 3600s. **RHS₂** rises only in the very last amount of time, reaching $P_2 = 40\%$ at 7200s, at the same level of P_1 . The no-flow probability is very low for the most of the temporal window, rising at 20% only at 7200s. Both **RHS₃** and **RHS₄** have a short peak of dominance factor, at about 10% for a few seconds,

at [50, 60]s. Finally, in VS the no-flow probability is never below 20%, and the profile is similar to MC, although **RHS**₁ is more relevant, up to 4000s. The other force are almost never dominant.

6 Discussion

7 Conclusions

Appendix A: Latin Hypercubes and orthogonal arrays

The Latin Hypercube Sampling (LHS) is a well established procedure for defining pseudo-random designs of samples in \mathbb{R}^d , with good properties with respect to the uniform probability distribution on an hypercube $[0, 1]^d$ (McKay et al., 1979; Owen, 1992a; Stein, 1987; Ranjan and Spencer, 2014; Ai et al., 2016). In particular, compared to a random sampling, a LHS: (i) enhances the capability to fill the d-dimensional space with a finite number of points, (ii) in case $d > 1$, avoids the overlapping of point locations in the one dimensional projections, (iii) reduces the dependence of the number of points necessary on the dimensionality d .

Definition 5 (Latin hypercube sampling) Let $\Xi = \{\xi_i : i = 1, \dots, N\}$ be a set of points inside the d -dimensional hypercube $C = [0, 1]^d$. Let $[0, 1] = \bigcup_{j=1}^N I_j$, where $I_j = [\frac{(j-1)}{N}, \frac{j}{N}]$. Let $\xi_i = (\xi_i^1, \dots, \xi_i^d)$, and for each $k \in \{1, \dots, d\}$, let $\Xi^k = \{\xi_i^k : i = 1, \dots, N\}$. Let λ^d be the uniform probability measure supported inside C , called Lebesgue measure. Then Ξ is a latin hypercube w.r.t. $\lambda^d \iff \forall j \in \{1, \dots, N\}, \forall k \in \{1, \dots, d\}, |\mathcal{I}_j \cap \Xi^k| = 1$.

The procedure is simple: once the desired number of samples $N \in \mathbb{N}$ is selected, and $[0, 1]$ is divided in N equal bins, then each bin will contain one and only one projection of the samples over every coordinate. The LHS definition is trivially generalized over $C = \prod_i^d [a_i, b_i]$, i.e. the cartesian product of d arbitrary intervals. That will be applied in this study, defining LHS over the parameter domain of the flow models.

There are a large number of possible designs, corresponding the number of permutations of the bins in the d -projections, i.e. $d \cdot N!$. If the permutations are randomly sampled there is a high possibility that the design will have good properties. However, this is not assured, and clusters or regions of void space may be observed in C . For this reason, we base our design on the orthogonal arrays (OA) (Owen, 1992b; Tang, 1993).

Definition 6 (Orthogonal arrays) Let $S = \{1, \dots, s\}$, where $s \geq 2$. Let $Q \in S^{n \times m}$ be a matrix of such integer values. Then Q is called an OA(n, m, s, r) \iff each $n \times r$ submatrix of Q contains all possible $1 \times r$ row vectors with the same frequency $\lambda = n/s^r$, which is called the index of the array. In particular, r is called the strength, n the size, ($m \geq r$) the constraints, and s the levels of the array.

Orthogonal arrays are very useful for defining latin hypercubes which are also forced to fill the space (or its r -dimensional subspaces) in a more robust way, at the cost of potentially requiring a larger number of points than a traditional LHS.

Proposition 7 Let Q be an OA(n, m, s, r). Then let $U \in \mathbb{R}^{n \times m}$ be defined as follows:

$$\forall k \in \{1, \dots, s\}, \forall j \in \{1, \dots, m\}, \{Q[\cdot, j] : Q[i, j] = k\} = \Pi(\{(k-1)\lambda s^{r-1}, \dots, k\lambda s^{r-1}\}),$$

where Π is a random permutation of λs^{r-1} elements. Then $\Xi = \{\xi_i = U[i, \cdot] : i = 1, \dots, n\}$ is a LHS w.r.t to λ^m over $C = [0, 1]^m$. Moreover, let $[0, 1]^r = \bigcup_{(h_1, \dots, h_r)=1}^s I_{(h_i)}$, where $I_{(h_i)} = \prod_i^r [\frac{(h_i-1)}{s}, \frac{h_i}{s}]$. Then $\forall D = (d_1, \dots, d_r) \subseteq \{1, \dots, m\}$, let $\Xi^D = \{(\xi^{d_1}, \dots, \xi^{d_r}) : i = 1, \dots, n\}$. We have that

$$\forall k \in \{1, \dots, s\}, \forall (h_i : i = 1, \dots, r) \in \{1, \dots, d\}^r, |\mathcal{I}_{(h_i)} \cap \Xi^D| = \lambda.$$

For each column of Q we are replacing the λs^{r-1} elements with entry k by a random permutation of $((k-1)\lambda s^{r-1} + h)_{h \in 1, \dots, \lambda s^{r-1}}$. After the replacement procedure is done, the newly obtained matrix U is equivalent to a LHS which inherits from Q the property of fully covering s^r equal r -dimensional hypercubes in every r -dimensional projection. Each hypercube contains λ points. In other words, inside each r -dimensional projection, the design associated to U fills the space like a regular grid at the scale of

those s^r hypercubes, but it is still an LHS at a finer scale, i.e. the λs^{r-1} one dimensional bins. A complete proof can be found in Tang (1993) and it is a straightforward verification of the required properties.

However, even in an LHS based on an $OA(n, m, s, r)$, if $r < m$ what happens in the projections with dimension $r' > r$ is not controlled, and randomizing procedures are made more difficult by the additional structure imposed by the OA . Moreover, the total number of points necessary to achieve a full design increases with r , and hence is affected by dimensionality issues.

Dealing with relatively small d , i.e. $d \in \{3, 4\}$, we adopt a LHS U created by a $OA(s^d, d, s, d)$. The strength is equal to the dimension d , hence the design fills the entire space like a d dimensional grid, but it is a LHS as well. In this case there is one point in each hypercube, and $\lambda = 1$. We take $s = 8$ for the 3-dimensional designs over the parameter space of Mohr-Coulomb and Voellmy-Salm models, i.e. 512 points; we took $s = 6$ for the 4-dimensional designs over the more complex parameter space of the Pouliquen-Forterre model, i.e. 1296 points.

References

- Aghakhani, H., Dalbey, K., Salac, D., and Patra, A. K. (2016). Heuristic and Eulerian interface capturing approaches for shallow water type flow and application to granular flows. *Computer Methods in Applied Mechanics and Engineering*, 304:243–264.
- Ai, M., Kong, X., and Li, K. (2016). A general theory for orthogonal array based latin hypercube sampling. *Statistica Sinica*, (26):761–777.
- Balmforth, N. J. and Kerswell, R. R. (2005). Granular collapse in two dimensions. *Journal of Fluid Mechanics*, 538:399–428.
- Barker, T., Schaeffer, D. G., Bohorquez, P., and Gray, J. M. N. T. (2015). Well-posed and ill-posed behaviour of the $\mu(i)$ -rheology for granular flow. *Journal of Fluid Mechanics*, 779:794–818.
- Bartelt, P. and McArdell, B. (2009). Granulometric investigations of snow avalanches. *Journal of Glaciology*, 55(193):829–833(5).
- Bartelt, P., Salm, B., and Gruber, U. (1999). Calculating dense-snow avalanche runout using a voellmy-fluid model with active/passive longitudinal straining. *Journal of Glaciology*, 45(150):242–254.
- Batchelor, G. (2000). *An Introduction to Fluid Dynamics*. Cambridge Mathematical Libraries. Cambridge University Press.
- Bayarri, M. J., Berger, J. O., Calder, E. S., Dalbey, K., Lunagomez, S., Patra, A. K., Pitman, E. B., Spiller, E. T., and Wolpert, R. L. (2009). Using Statistical and Computer Models to Quantify Volcanic Hazards. *Technometrics*, 51(4):402–413.
- Bayarri, M. J., Berger, J. O., Calder, E. S., P. A. K. P. E. B., Spiller, E. T., and Wolpert, R. L. (2015). Probabilistic Quantification of Hazards: A Methodology Using Small Ensembles of Physics-Based Simulations and Statistical Surrogates. *International Journal for Uncertainty Quantification*, 5(4):297–325.
- Bursik, M., Patra, A., Pitman, E. B., Nichita, C., Macias, J. L., Saucedo, R., and Girina, O. (2005). Advances in studies of dense volcanic granular flows. *Reports on Progress in Physics*, 68(2):271.
- Capra, L., Gavilanes-Ruiz, J. C., Bonasia, R., Saucedo-Giron, R., and Sulpizio, R. (2015). Re-assessing volcanic hazard zonation of volcán de colima, méxico. *Natural Hazards*, 76(1):41–61.
- Capra, L., Macís, J., Cortés, A., Dávila, N., Saucedo, R., Osorio-Ocampo, S., Arce, J., Gavilanes-Ruiz, J., Corona-Chávez, P., García-Sánchez, L., Sosa-Ceballos, G., and Vázquez, R. (2016). Preliminary report on the july 10–11, 2015 eruption at volcán de colima: Pyroclastic density currents with exceptional runouts and volume. *Journal of Volcanology and Geothermal Research*, 310(Supplement C):39 – 49.
- Capra, L., Manea, V. C., Manea, M., and Norini, G. (2011). The importance of digital elevation model resolution on granular flow simulations: a test case for colima volcano using titan2d computational routine. *Natural Hazards*, 59(2):665–680.
- Charbonnier, S., Germa, A., Connor, C., Gertisser, R., Preece, K., Komorowski, J.-C., Lavigne, F., Dixon, T., and Connor, L. (2013). Evaluation of the impact of the 2010 pyroclastic density currents at merapi volcano from high-resolution satellite imagery, field investigations and numerical simulations. *Journal of Volcanology and Geothermal Research*, 261(Supplement C):295 – 315. Merapi eruption.
- Charbonnier, S. J. and Gertisser, R. (2009). Numerical simulations of block-and-ash flows using the titan2d flow model: examples from the 2006 eruption of merapi volcano, java, indonesia. *Bulletin of Volcanology*, 71(8):953–959.
- Christen, M., Kowalski, J., and Bartelt, P. (2010). RAMMS: Numerical simulation of dense snow avalanches in three-dimensional terrain. *Cold Regions Science and Technology*, 63:1–14.
- DaCruz, F., Emam, S., Prochnow, M., Roux, J.-N., and Chevoir, F. (2005). Rheophysics of dense granular materials: Discrete simulation of plane shear flows. *Physical Review E*, 72:021309.

- Dade, W. B. and Huppert, H. E. (1998). Long-runout rockfalls. *Geology*, 26(9):803–806.
- Dalbey, K., Patra, A. K., Pitman, E. B., Bursik, M. I., and Sheridan, M. F. (2008). Input uncertainty propagation methods and hazard mapping of geophysical mass flows. *Journal of Geophysical Research: Solid Earth*, 113:1–16.
- Dalbey, K. R. (2009). *Predictive Simulation and Model Based Hazard Maps*. PhD thesis, University at Buffalo.
- Davila, N., Capra, L., Gavilanes-Ruiz, J., Varley, N., Norini, G., and Vazquez, A. G. (2007). Recent lahars at volcán de colima (mexico): Drainage variation and spectral classification. *Journal of Volcanology and Geothermal Research*, 165(3):127 – 141.
- Denlinger, R. P. and Iverson, R. M. (2001). Flow of variably fluidized granular masses across three-dimensional terrain: 2. Numerical predictions and experimental tests. *Journal of Geophysical Research*, 106(B1):553–566.
- Denlinger, R. P. and Iverson, R. M. (2004). Granular avalanches across irregular three-dimensional terrain: 1. Theory and computation. *Journal of Geophysical Research (Earth Surface)*, 109(F1):F01014.
- Edwards, A. N. and Gray, J. M. N. T. (2015). Erosion-deposition waves in shallow granular free-surface flows. *Journal of Fluid Mechanics*, 762:35–67.
- Fischer, J., Kowalski, J., and Pudasaini, S. P. (2012). Topographic curvature effects in applied avalanche modeling. *Cold Regions Science and Technology*, 74–75:21–30.
- Forterre, Y. (2006). Kapiza waves as a test for three-dimensional granular flow rheology. 563(*Journal of Fluid Mechanics*):123–132.
- Forterre, Y. and Pouliquen, O. (2002). Stability analysis of rapid granular chute flows: formation of longitudinal vortices. *Journal of Fluid Mechanics*, 467:361–387.
- Forterre, Y. and Pouliquen, O. (2003). Long-surface-wave instability in dense granular flows. *Journal of Fluid Mechanics*, 486:21–50.
- Forterre, Y. and Pouliquen, O. (2008). Flows of dense granular media. *Annual Review of Fluid Mechanics*, 40(1):1–24.
- Fraccarollo, L. and Toro, E. F. (1995). Experimental and numerical assessment of the shallow water model for two dimensional dam-break type problems. *Journal of Hydraulic Research*, 33:843–864.
- Freundt, A. and Bursik, M. I. (1998). Pyroclastic flow transport mechanisms. In Freundt, A. and Rosi, M., editors, *From Magma to Tephra: Modelling Physical Processes of Explosive Volcanism*, volume 4 of *Advances in Volcanology*, pages 151–222. Elsevier Science, Amsterdam.
- González, M. B., Ramírez, J. J., and Navarro, C. (2002). Summary of the historical eruptive activity of volcán de colima, mexico 1519–2000. *Journal of Volcanology and Geothermal Research*, 117(1):21 – 46.
- Gray, J. M. N. T. and Edwards, A. N. (2014). A depth-averaged $\mu(I)$ -rheology for shallow granular free-surface flows. *Journal of Fluid Mechanics*, 755:503–534.
- Gray, J. M. N. T., Tai, Y. C., and Noelle, S. (2003). Shock waves, dead zones and particle-free regions in rapid granular free-surface flows. *Journal of Fluid Mechanics*, 491:161–181.
- Gray, J. M. N. T., Wieland, M., and Hutter, K. (1999). Gravity-driven free surface flow of granular avalanches over complex basal topography. *Proceedings of the Royal Society A: Mathematical, Physical and Engineering Sciences*, 455(1985):1841–1874.
- Greve, R., Koch, T., and Hutter, K. (1994). Unconfined flow of granular avalanches along a partly curved surface: experiments and theoretical predictions. *Proc. R. Soc. London Ser. A*, 342:573–600.

- Gruber, U. and Bartelt, P. (2007). Snow avalanche hazard modelling of large areas using shallow water numerical models and GIS. *Environmrntal Modelling & Software*, 22:1472–1481.
- Hokanardottir, K. M. and Hogg, A. J. (2005). Oblique shocks in rapid granular flows. *Phys. Fluids*, 17:077101.
- Hutter, K., Siegel, M., Savage, S. B., and Nohguchi, Y. (1993). Two-dimensional spreading of a granular avalanche down an inclined plane part I. Theory. *Acta Mechanica*, 100:37–68.
- Iordanoff, I. P. and Khonsari, M. M. (2004). Granular Lubrication: Toward an Understanding of the Transition Between Kinetic and Quasi-Fluid Regime. *Journal of Tribology*, 126(1):137–145.
- Iverson, R. M. (1997). The physics of debris flows. *Reviews of Geophysics*, 35:245–296.
- Iverson, R. M. and Denlinger, R. P. (2001). Flow of variably fluidized granular masses across three-dimensional terrain: 1. Coulomb mixture theory. *Journal of Geophysical Research*, 106(B1):537.
- Iverson, R. M. and George, D. L. (2014). A depth-averaged debris-flow model that includes the effects of evolving dilatancy. i. physical basis. *Proceedings of the Royal Society of London A: Mathematical, Physical and Engineering Sciences*, 470(2170).
- Iverson, R. M., Logan, M., and Denlinger, R. P. (2004). Granular avalanches across irregular three-dimensional terrain: 2. experimental tests. *Journal of Geophysical Research: Earth Surface*, 109(F1):n/a–n/a. F01015.
- Jaeger, H. M., Liu, C., and Nagel, S. R. (1989). Relaxation at the Angle of Repose. *Physical Review Letters*, 62(1):40–43.
- Jop, P., Forterre, Y., and Pouliquen, O. (2006). A constitutive law for dense granular flows. *Nature*, 441:727–730.
- Kelfoun, K. (2011). Suitability of simple rheological laws for the numerical simulation of dense pyroclastic flows and long-runout volcanic avalanches. *Journal of Geophysical Research*, 116:B08209.
- Kelfoun, K. and Druitt, T. H. (2005). Numerical modeling of the emplacement of socompa rock avalanche, chile. *Journal of Geophysical Research: Solid Earth*, 110(B12).
- Kelfoun, K., Samaniego, P., Palacios, P., and Barba, D. (2009). Testing the suitability of frictional behaviour for pyroclastic flow simulation by comparison with a well-constrained eruption at Tungurahua volcano (Ecuador). *Bulletin of Volcanology*, 71:1057–1075.
- Kern, M., Bartelt, P., Sovilla, B., and Buser, O. (2009). Measured shear rates in large dry and wet snow avalanches. *Journal of Glaciology*, 55(190):327–338.
- la Cruz-Reyna, S. D. (1993). Random patterns of occurrence of explosive eruptions at colima volcano, mexico. *Journal of Volcanology and Geothermal Research*, 55(1):51 – 68.
- Lajeunesse, E., Monnier, J. B., and Homsy, G. M. (2005). Granular slumping on a horizontal surface. *Phys. Fluids*, 17:103302.
- Luca, I., Tai, Y., and Kuo, C. (2016). *Shallow Geophysical Mass Flows down Arbitrary Topography: Model Equations in Topography-fitted Coordinates, Numerical Simulation and Back-calculations of Disastrous Events*. Advances in Geophysical and Environmental Mechanics and Mathematics. Springer International Publishing.
- Mangeney-Castelnau, A., Bouchut, F., Thomas, N., Vilotte, J. P., and Bristeau, M.-O. (2007). Numerical modeling of self-channeling granular flows and of their levee/channel deposits. *J. Geophys. Res.*, 112:F02017.
- Mangeney-Castelnau, A., Bouchut, F., Vilotte, J. P., Lajeunesse, E., Aubertin, A., and Pirulli, M. (2005). On the use of Saint-Venant equations to simulate the spreading of a granular mass. *J. Geophys. Res.*, 110:B09103.

- Martin Del Pozzo, A. M., Sheridan, M. F., Barrera, M., Hubp, J. L., and Selem, L. V. (1995). Potential hazards from Colima Volcano, Mexico. *Geofisica Internacional*, 34:363–376.
- McKay, M. D., Beckman, R. J., and Conover, W. J. (1979). A comparison of three methods for selecting values of input variables in the analysis of output from a computer code. *Technometrics*, 21(2):239–245.
- Norini, G., De Beni, E., Andronico, D., Polacci, M., Burton, M., and Zucca, F. (2009). The 16 november 2006 flank collapse of the south-east crater at mount etna, italy: Study of the deposit and hazard assessment. *Journal of Geophysical Research: Solid Earth*, 114(B2):n/a–n/a. B02204.
- Ogburn, S. E., Berger, J., Calder, E. S., Lopes, D., Patra, A., Pitman, E. B., Rutarindwa, R., Spiller, E., , and Wolpert, R. L.
- Owen, A. B. (1992a). A Central Limit Theorem for Latin Hypercube Sampling. *Journal of the Royal Statistical Society.,* 54(2):541–551.
- Owen, A. B. (1992b). Orthogonal arrays for computer experiments, integration and visualization. *Statistica Sinica*, 2(2):439–452.
- Patra, A., Nichita, C., Bauer, A., Pitman, E., Bursik, M., and Sheridan, M. (2006). Parallel adaptive discontinuous galerkin approximation for thin layer avalanche modeling. *Computers & Geosciences*, 32(7):912 – 926. Computer Simulation of natural phenomena for Hazard Assessment.
- Patra, A. K., Bauer, A. C., Nichita, C. C., Pitman, E. B., Sheridan, M. F., Bursik, M., Rupp, B., Webber, A., Stinton, A. J., Namikawa, L. M., and Renschler, C. S. (2005). Parallel adaptive numerical simulation of dry avalanches over natural terrain. *Journal of Volcanology and Geothermal Research*, 139(1-2):1–21.
- Pirulli, M., Bristeau, M. O., Mangeney, A., and Scavia, C. (2007). The effect of the earth pressure coefficients on the runout of granular material. *Environmental Modelling & Software*, 22(10):1437–1454.
- Pirulli, M. and Mangeney, A. (2008). Results of Back–Analysis of the Propagation of Rock Avalanches as a Function of the Assumed Rheology. *Rock Mechanics and Rock Engineering*, 41(1):59–84.
- Pitman, E., Nichita, C., Patra, A., Bauer, A., Bursik, M., and Webb, A. (2003a). A model of granular flows over an erodible surface. *Discrete and Continuous Dynamical Systems - Series B*, 3(4):589–599.
- Pitman, E. B. and Le, L. (2005). A two-fluid model for avalanche and debris flows. *Philosophical transactions. Series A, Mathematical, physical, and engineering sciences*, 363(1832):1573–601.
- Pitman, E. B., Nichita, C. C., Patra, A., Bauer, A., Sheridan, M., and Bursik, M. (2003b). Computing granular avalanches and landslides. *Physics of Fluids*, 15(12):3638.
- Pouliquen, O. (1999). Scaling laws in granular flows down rough inclined planes. *Physics of Fluids*, 11(3):542–548.
- Pouliquen, O. and Forterre, Y. (2002). Friction law for dense granular flows: application to the motion of a mass down a rough inclined plane. *Journal of Fluid Mechanics*, 453:133–151.
- Procter, J. N., Cronin, S. J., Platz, T., Patra, A., Dalbey, K., Sheridan, M., and Neall, V. (2010). Mapping block-and-ash flow hazards based on titan 2d simulations: a case study from mt. taranaki, nz. *Natural Hazards*, 53(3):483–501.
- Pudasaini, S. and Hutter, K. (2007). *Avalanche Dynamics: Dynamics of Rapid Flows of Dense Granular Avalanches*. Springer.
- Pudasaini, S. P. and Hutter, K. (2003). Rapid shear flows of dry granular masses down curved and twisted channels. *Journal of Fluid Mechanics*, 495:193–208.
- Ranjan, P. and Spencer, N. (2014). Space-filling latin hypercube designs based on randomization restrictions in factorial experiments. *Statistics and Probability Letters*, 94(Supplement C):239 – 247.

- Rankine, W. J. M. (1857). On the Stability of Loose Earth. *Phil. Trans. R. Soc. Lond.*, 147(2):9–27.
- Reyes-Dvila, G. A., Armbula-Mendoza, R., Espinasa-Perea, R., Pankhurst, M. J., Navarro-Ochoa, C., Savov, I., Vargas-Bracamontes, D. M., Corts-Corts, A., Gutierrez-Martinez, C., Valds-Gonzalez, C., Dominguez-Reyes, T., Gonzalez-Amezcua, M., Martinez-Fierros, A., Ramirez-Vazquez, C. A., Credens-Gonzalez, L., Castaeda-Bastida, E., de los Monteros, D. M. V. E., Nieto-Torres, A., Campion, R., Courtois, L., and Lee, P. D. (2016). Volcan de colima dome collapse of july, 2015 and associated pyroclastic density currents. *Journal of Volcanology and Geothermal Research*, 320(Supplement C):100 – 106.
- Rupp, B. (2004). An analysis of granular flows over natural terrain. Master's thesis, University at Buffalo.
- Rupp, B., Bursik, M., Namikawa, L., Webb, A., Patra, A. K., Saucedo, R., Macías, J. L., and Renschler, C. (2006). Computational modeling of the 1991 block and ash flows at Colima Volcano, México. *Geological Society of America Special Papers*, 402(11):223–237.
- Ruyer-Quil, C. and Manneville, P. (2000). Improved modeling of flows down inclined planes. *Eur. Phys. J. B*, 15:357–369.
- Salm, B. (1993). Flow, flow transition and runout distances of flowing avalanches. *Annals of Glaciology*, 18:221–226.
- Salm, B., Burkard, A., and Gubler, H. (1990). Berechnung von Fliesslawinen: eine Anleitung für Praktiker mit Beispielen. *Mitteilungen des Eidgenössische Institutes für Schnee- und Lawinenforschung*, 47.
- Sarocchi, D., Sulpizio, R., Macías, J., and Saucedo, R. (2011). The 17 july 1999 block-and-ash flow (baf) at colima volcano: New insights on volcanic granular flows from textural analysis. *Journal of Volcanology and Geothermal Research*, 204(1):40 – 56.
- Saucedo, R., Macías, J., Bursik, M., Mora, J., Gavilanes, J., and Cortes, A. (2002). Emplacement of pyroclastic flows during the 1998–1999 eruption of volcán de colima, méxico. *Journal of Volcanology and Geothermal Research*, 117(1):129 – 153.
- Saucedo, R., Macías, J., Gavilanes, J., Arce, J., Komorowski, J., Gardner, J., and Valdez-Moreno, G. (2010). Eyewitness, stratigraphy, chemistry, and eruptive dynamics of the 1913 plinian eruption of volcán de colima, méxico. *Journal of Volcanology and Geothermal Research*, 191(3–4):149 – 166.
- Saucedo, R., Macías, J., Sheridan, M., Bursik, M., and Komorowski, J. (2005). Modeling of pyroclastic flows of colima volcano, mexico: implications for hazard assessment. *Journal of Volcanology and Geothermal Research*, 139(1):103 – 115. Modeling and Simulation of Geophysical Mass Flows.
- Saucedo, R., Macías, J. L., and Bursik, M. (2004). Pyroclastic flow deposits of the 1991 eruption of Volcán de Colima, Mexico. *Bulletin of Volcanology*, 66(4):291–306.
- Savage, S. B. and Hutter, K. (1989). The motion of a finite mass of granular material down a rough incline. *Journal of Fluid Mechanics*, 199:177.
- Savage, S. B. and Iverson, R. M. (2003). Surge dynamics coupled to pore-pressure evolution in debris flows. *Debris-Flow Hazards Mitigation: Mechanics, Prediction and Assessment*, edited by: Rickenmann, D. and Chen, C. L., Millpress, 1:503–514.
- Sheridan, M., Stinton, A., Patra, A., Pitman, E., Bauer, A., and Nichita, C. (2005). Evaluating titan2d mass-flow model using the 1963 little tahoma peak avalanches, mount rainier, washington. *Journal of Volcanology and Geothermal Research*, 139(1):89 – 102. Modeling and Simulation of Geophysical Mass Flows.
- Sheridan, M. F. and Macas, J. (1995). Estimation of risk probability for gravity-driven pyroclastic flows at volcan colima, mexico. *Journal of Volcanology and Geothermal Research*, 66(1):251 – 256. Models of Magnetic Processes and Volcanic Eruptions.
- Sheridan, M. F., Patra, A. K., Dalbey, K., and Hubbard, B.

- Silbert, L. E., Ertas, D., Grest, G. S., Halsey, T. C., Levine, D., and Plimpton, S. J. (2001). Granular flow down an inclined plane: Bagnold scaling and rheology. *Physical Review E*, 64(5):051302.
- Spiller, E. T., Bayarri, M. J., Berger, J. O., Calder, E. S., Patra, A. K., Pitman, E. B., and Wolpert, R. L. (2014). Automating emulator construction for geophysical hazard maps. *SIAM/ASA Journal on Uncertainty Quantification*, 2(1):126–152.
- Stefanescu, E. R., Bursik, M., Cordoba, G., Dalbey, K., Jones, M. D., Patra, A. K., Pieri, D. C., Pitman, E. B., and Sheridan, M. F. (2012a). Digital elevation model uncertainty and hazard analysis using a geophysical flow model. *Proceedings of the Royal Society of London A: Mathematical, Physical and Engineering Sciences*, 468(2142):1543–1563.
- Stefanescu, E. R., Bursik, M., and Patra, A. K. (2012b). Effect of digital elevation model on mohr-coulomb geophysical flow model output. *Natural Hazards*, 62(2):635–656.
- Stein, M. (1987). Large sample properties of simulations using latin hypercube sampling. *Technometrics*, 29(2):143–151.
- Sulpizio, R., Capra, L., Sarocchi, D., Saucedo, R., Gavilanes-Ruiz, J., and Varley, N. (2010). Predicting the block-and-ash flow inundation areas at volcán de colima (colima, mexico) based on the present day (february 2010) status. *Journal of Volcanology and Geothermal Research*, 193(1):49 – 66.
- Tang, B. (1993). Orthogonal array-based latin hypercubes. *Journal of the American Statistical Association*, 88(424):1392–1397.
- Toro, E. (2013). *Riemann Solvers and Numerical Methods for Fluid Dynamics: A Practical Introduction*. Springer Berlin Heidelberg.
- Voellmy, A. (1955). Über die Zerstörungskraft von Lawinen. *Schweiz Bauzeitung*, 73:159–165, 212–217, 246–249, 280–285.
- Webb, A. (2004). Granular flow experiments to validate numerical flow model, TITAN2D. Master's thesis, University at Buffalo.
- Webb, A. and Bursik, M. (2016). Granular flow experiments for validation of numerical flow models. Technical report, University at Buffalo.
- Wieland, J. M., Gray, J. M. N. T., and Hutter, K. (1999). Channelized free-surface flow of cohesionless granular avalanches in a chute with shallow lateral curvature. *Journal of Fluid Mechanics*, 392:73–100.
- Yu, B., Dalbey, K., Webb, A., Bursik, M., Patra, A. K., Pitman, E. B., and Nichita, C. (2009). Numerical issues in computing inundation areas over natural terrains using Savage-Hutter theory. *Natural Hazards*, 50(2):249–267.
- Zobin, V., Luhr, J., Taran, Y., Bretón, M., Cortés, A., Cruz-Reyna, S. D. L., Domínguez, T., Galindo, I., Gavilanes, J., Muniz, J., Navarro, C., Ramírez, J., Reyes, G., Ursúa, M., Velasco, J., Alatorre, E., and Santiago, H. (2002). Overview of the 1997–2000 activity of volcán de colima, méxico. *Journal of Volcanology and Geothermal Research*, 117(1):1 – 19.
- Zobin, V. M., Arámbula, R., Bretón, M., Reyes, G., Plascencia, I., Navarro, C., Téllez, A., Campos, A., González, M., León, Z., Martínez, A., and Ramírez, C. (2015). Dynamics of the january 2013–june 2014 explosive-effusive episode in the eruption of volcán de colima, méxico: insights from seismic and video monitoring. *Bulletin of Volcanology*, 77(4):31.